NTNU – Trondheim
Norwegian University of
Science and Technology

Development and testing of a Linnik Interference Microscope for Sub-surface Inspection of Silicon during moving Indentation

Lars Oskar Osnes Kittang

Master of Science in Physics and Mathematics
Submission date: July 2012
Supervisor: Morten Kildemo, IFY
Co-supervisor: Lars Johnsen, SINTEF

Norwegian University of Science and Technology
Department of Physics

Development and testing of a Linnik Interference Microscope for Sub-surface Inspection of Silicon during moving Indentation

Lars Oskar Osnes Kittang

July 23, 2012

Samandrag

"Fixed-abrasive diamond wire sawing" er ein lovande teknikk for redusering av kostnader i forbindelse med saging av silisium-wafere for solceller. Dei mikroskopiske mekanismane for fjerning av materiale i denne prosessen er ikkje fullstendig forstått, og trengs undersøkast for å kunne redusere kostnader ytterlegare.

Eit interferensmikroskop for inspeksjon av interne refleksjonar i monokrystallinsk silisium har blitt bygd basert på Linnik-konfigurasjonen, med spesifikt bruksområde for sanntids-overvåking av bevegelege fordjupningar. Nødvendig teori for å forklare instrumentets funksjonalitet er beskrive ut frå eit litteratursøk, og kombinerer fenomener som optisk interferens, koherens og avbildingsteori. Det optiske systemet har blitt eksperimentelt testa med fokus på konvensjonell avbildingsevne og interferometri. Testar angåande avbildingsevne viser stor forstørring, ei lateral oppløysingsgrense på 0.9μm og tilstrekkeleg god djupneskarpleik. Dette gir forbetra forhold for avbilding av interne refleksjonar samanlikna med ein tidlegare brukt prototype.

Systemets evne til å måle djupne-profilar av silisiumoverflater har blitt testa med bruk av ei lyskjelde med lav tidskoherens. Den brukte teknikken reknar ut djupner frå interferogram som er innhenta ved skanning av eit optisk referanse-felt. Foreløpige resultat med ei flat test-overflate viser at djupner ikkje kan bestemmast nøyaktig nok for å kunne anse dei målte profilane som pålitelege rekonstruksjonar. Det er i denne rapporten diskutert at den dårlege nøyaktigheita er grunna eksperimentelle feil, inkludert ei ikkje-uniform belysning, uønskte refleksjonar og ikkje-uniforme målingsintervall ved skanning.

To eksperiment med bevegelege fordjupningar på silisiumoverflater har blitt utført. Desse er henholdsvis overvåka av konvensjonell avbilding og beregningar av interferometriske fasekart. Resultatene er sett i kontekst med den teoretiske forståinga av mekanismane for fjerning av materiale i "fixed-abrasive diamond wire sawing". Utviklinga av overflateskade er observert som samankobling av avskallingar, i begge eksperimenta. I tillegg er laterale sprekker under overflata identifisert frå dei interferometriske fasekarta. Fasekart av overflateskade kan likevel kun i begrensa grad tolkast som topografiske konturlinjer av overflata si djupne. Ei djupare forståing av mekanismane for fjerning av materiale krev kvantitative målingar av djupne. Dette kan i større grad oppnåast ved å rekne ut nøyaktige overflateprofilar frå interferogram. Framtidige forbetringar av systemet er avhengig av ei revurdering av det optiske designet samt betre kontroll over målingsintervalla ved skanning.

Abstract

Fixed-abrasive diamond wire sawing is a promising technique for reduction of costs related to sawing of silicon wafers for solar cells. The microscopic mechanisms of material removal in the process are however not fully understood, and must be surveyed in order for costs to be further reduced.

An interference microscope for sub-surface inspection of mono-crystalline silicon has been built based on the Linnik configuration, with specific application to in-situ monitoring of moving indentations. The working principles of the instrument are explained from a literature study on relevant theory, combining concepts of optical interference and coherence with imaging theory. The optical system has been experimentally tested in terms of its performance in conventional imaging as well as its interferometric capabilities. Tests on the imaging performance show that a large magnification is accompanied by a lateral resolution with a lower limit of 0.9μm and an adequately long depth of field. This provides improved conditions for imaging of internal reflections in silicon, compared to a previously used prototype.

Using a light source of low temporal coherence, the capability of the system to measure depth profiles of silicon surfaces has been tested. The technique calculates depths from interferograms recorded by scanning of a reference field. Preliminary results from a flat test surface show that depths are not determined accurately enough for calculated profiles to be considered as reliable reconstructions. It is discussed that the inaccuracy is caused by a number of experimental factors including non-uniform illumination, undesired reflections and non-uniform sampling intervals in scanning.

Two experiments with moving indentations on silicon surfaces have been performed, monitored by conventional imaging and calculation of interferometric phase maps, respectively. Results are seen in context with the theoretical understanding of material removal mechanisms in fixed-abrasive diamond wire sawing. The evolution of surface damage is observed as interconnection of chippings in both experiments. In addition, sub-surface lateral cracks are identified from interferometric phase maps. The phase maps of surface damage can, however, only to a limited extent be interpreted as topographic contour lines of surface depth. A deeper knowledge of removal mechanisms requires quantitative measurements of depths. This can be better achieved by calculating accurate depth profiles from interferograms. Future enhancement of the system is dependent on a reevaluation of the optical design as well as better control of sampling intervals in scanning.

Preface

This thesis is a report of the work performed for the Master thesis in the final semester of the Master's program in Applied Physics at NTNU. The work presented is a continuation of the work started in my project work of Fall 2011, and is part of a research project run by Lars Johnsen at SINTEF ICT in consultation with REC Wafer Norway AS and the Research Council of Norway [1]. Work on the project was started by Lars Johnsen and Kay Gastinger[1] in 2009. Contributions have since been given by Astrid Aksnes[2], Ove Simonsen [2] and myself. This report presents and discusses obtained results, and also describes relevant theory and the experimental apparatus and procedure.

The main supervisor of my work has been Morten Kildemo[3], who has guided me in the theoretical aspects of the work. I am grateful for his contributions and the time he has spent in theoretical discussions. Lars Johnsen has been my professional supervisor at SINTEF, guiding me along the path of the experimental work. I would like to thank him for providing me the opportunity of doing this thesis, and also for the good cooperation he has contributed. Gratitude is also given to Lars Martin Aas[3] for his programming assistance and the Precision Mechanical workshop at NTNU for their services in modifying parts for the apparatus.

The experimental work has been embossed by delays due to technical problems and the delivery time of necessary parts. A significant amount of time has been spent troubleshooting the former.

"Through the darkness of future past,
the magician longs to see" *David Lynch*

[1]SINTEF ICT
[2]Department of Electronics and Telecommunications, NTNU
[3]Department of Physics, NTNU

Contents

Chapter 1

Introduction

1.1 Industrial motivation

Solar power is a highly sustainable and environmental-friendly source of electrical energy. The working principles of converting sunlight into electricity with solar cells has been known for decades. Still, only a small amount of today's consumed electricity is produced from solar cells made by the photo-voltaic (PV) industry. This is in large part due to high costs in the fabrication of cells. In competing with other energy sources, the main challenge for the PV industry lies in the reduction of fabrication costs [3, 4].

1.1.1 Silicon solar cells

Solar cells are made from semiconductor materials that convert light into electricity by the photoelectric effect[1] [7]. By far, the most used semiconductor material in solar cells is silicon. About 83% of todays solar cells are manufactured from crystalline silicon (c-Si). The dominance of silicon as the primary raw material of the PV industry is partly due to its abundance. In the form of silica[2], SiO_2, it is the second most abundant element in the earth's crust [8].

Silicon does not achieve the highest of conversion efficiencies[3] of solar cells; the record has been set at 43.5% based on gallium arsenide material (GaAs). The theoretical efficiency limit of c-Si cells has almost been reached, with a record set at 25.0% by Green at UNSW [9]. Still, c-Si remains the primary material of choice for commercial cells due to manufacturing and material costs.

[1] First explained by Albert Einstein in 1905 [5]. He received the Nobel Prize in Physics in 1921 "for his services to theoretical physics, and especially for his discovery of the law of the photoelectric effect" [6]

[2] Also known as quartz.

[3] In converting solar power to electrical power

1.1.2 Wafering

Commercial c-Si solar cells are based on *wafers*, thin slices of c-Si on which the final cell is built. At present time, wafers of thickness 180-220μm are produced [10]. The making of thin wafers from large blocks of silicon, known as ingots, is an early but important stage in the production line of solar cells. The diagrams of Figure 1.1 illustrate how costs are spread over different stages in the production line. As much as 65% of the total manufacturing cost is due to production of wafers [10].

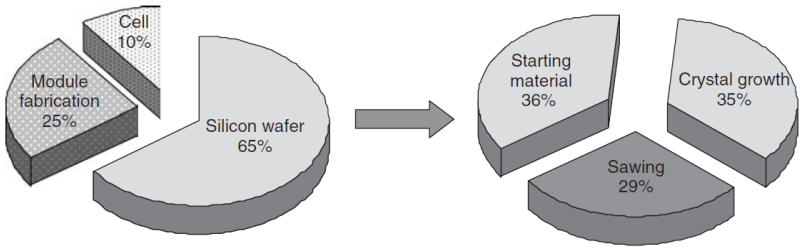

Figure 1.1: **Left:** The total cost of c-Si solar cell production divided between different stages of the process. **Right:** Costs related to the production of wafers. [Reprinted from Luque et al. [10].]

The aim of the *wafering* process is to produce thin wafers of high quality at low costs. Costs are largely related to the throughput at which wafers are produced, but also the amount of raw material needed per wafer. A large amount of material is wasted in the wafering process by *kerf losses*. In order to keep material costs at a minimum, it is desired to produce thin wafers with small kerf losses. In addition, wafering causes surface damage on the wafers. This damage is reduced by etching at a later stage in the process, thus further increasing costs [11, 12].

Multi-wire sawing

For commercial cells, the dominant wafering technique is multi-wire sawing. An illustration of the technique is shown in Figure 1.2. A silicon ingot is pushed against a parallel web of traveling wires that slices the silicon into thin wafers. This allows a high throughput of hundreds of wafers per sawing operation. The pitch of the wires largely determine the final thickness of the wafers. A long wire is used to set up the web, and is pulled from a reservoir spool to an intake spool. Hence the wires travel parallel to the silicon surface with large velocity.

Abrasive particles in the region between wire and silicon are responsible for the material removal necessary for sawing. To date, the dominant sawing technique uses silicon carbide (SiC) as loose abrasive particles in a lubricating slurry that is fed to the wire. Such systems are known as loose-abrasive. The SiC particles are not fixed to the wire, but as the wire is pulled they are dragged with it in a rolling motion. When the ingot is pushed

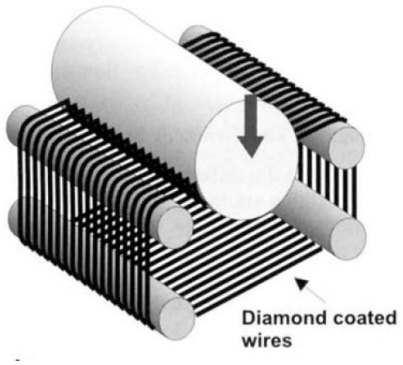

Figure 1.2: The multi-wire sawing technique. A silicon ingot is pushed against a web of traveling wires, slicing it into hundreds of wafers simultaneously. [Reprinted from Lee [13].]

through the web, the abrasives apply pressure on the silicon surface. This interaction causes continuous removal of silicon, eventually sawing through the entire ingot [10, 11]. A microscopic mechanics model of this material removal has been given by Möller [14]. The abrasive particles are believed to perform rolling indentations on the silicon surface, which eventually chip away pieces of material.

Fixed-abrasive diamond wire sawing

A novel alternative to the loose-abrasive wafering technique is fixed-abrasive diamond wire sawing (FADWS). The machinery of this technique is similar to that used in loose-abrasive sawing, except that the abrasives particles are diamonds fixed to the wire. The slurry is replaced by a water-soluble coolant liquid that is more environmentally friendly[15]. Diamond grits are attached to an iron-based wire either by electroplating or a by a resin bond as shown in Figure 1.3 [16]. As the wire is pulled, the abrasives follow its movement and effectively grind the silicon.

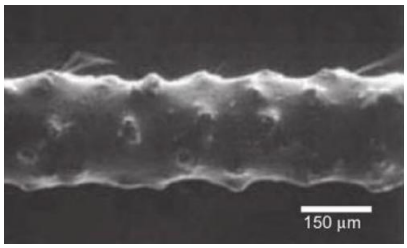

Figure 1.3: Small diamond grits attached to an iron wire by a resin bond. [Reprinted from Watanabe et al. [16].]

Studies on the slicing of wafers with fixed-abrasive diamonds show an improved throughput of a factor of 2.5 compared to slicing with loose abrasives. In addition, the thickness of

surface damage is reduced by a factor of two [16]. It is therefore a promising technique for wafering. However, there is a lack of knowledge on the mechanisms of material removal associated with the process. Deeper knowledge about these mechanisms is needed in order to survey the effect of process parameters, and hence optimize the technique for reduced costs. A theoretical model presented by Gao et al. [17] considers the diamond grits as performing *moving* indentations on the silicon surface, imposing both normal and tangential forces.

The work presented in this report is motivated by the possibility of studying material removal mechanisms of the FADWS process experimentally, under controlled circumstances. It is aimed at developing an experimental apparatus for in-situ inspection of a silicon surface's response to a moving indentation. Physically, moving indentations are performed by first burying an indenter to a desired depth on a clean silicon surface. This is followed by translation of the indenter parallel to the silicon surface, in a scratching fashion. The experimental apparatus is the prototype of an instrument to be used for characterization of removal mechanisms.

1.2 Previous prototype

Gastinger and Johnsen developed the idea and proof of principle of an interference microscope for sub-surface inspection of c-Si based on the Michelson interferometer[4] in 2010 [18]. It was later built and used to inspect a c-Si surface during indentation, with contributions from Simonsen and Aksnes [2, 19]. The indentation was intended to represent the material removal process of the loose-abrasive sawing technique. Simonsen obtained interferometric phase maps of an indented surface, revealing chippings and sub-surface cracks. It was however not succeeded to relate phase maps to the depth profiles of chippings.

A different method of measuring surface depths was later analyzed by the author of this text in a project assignment [20]. The prototype used by Simonsen was slightly modified, and it was aimed at determining depths from interferograms, exploiting the low coherence of the light source. It was attempted to determine the accuracy at which depths could be measured, but the study was complicated by a lack of repeatability in experiments. Results did however show promising prospects for further work.

1.3 Development and testing of new prototype

Johnsen has designed a new prototype of an interference microscope for sub-surface inspection of c-Si. The apparatus is based on the Linnik interference microscope, enabling enhanced optical resolution and increased flexibility in alignment of light. The industrial

[4]Presented in Section 2.2.2.

motivation has for the work presented in this report been shifted towards a study of the FADWS process, and equipment has been built in order to perform moving indentations. Still, the work picks up where the project assignment was ended. It is primarily aimed at testing the prototype's capability of measuring three-dimensional depth profiles from interferograms.

It is stressed that this text does not seek to understand the FADWS process. Focus is aimed at the development and testing of the new prototype, with emphasis on its performance. Still, experiments with moving indentations have been performed, with results attempted seen in context with the theoretical model of removal mechanisms.

The experimental work presented in this report is summarized as follows:

- Building an interference microscope for sub-surface inspection of c-Si
- Testing the imaging performance of the system
- Testing interference fringes' response to a tilted object surface
- Writing computational code for recording and analyzing interferograms
- Measuring the depth profile of a flat test surface
- Performing moving indentations, monitored by both conventional imaging and interferometric phase maps

The report starts off with a description of the theoretical concepts relevant to the working principle of the interference microscope, followed by a brief description of the theoretical model of material removal mechanisms. The experimental apparatus and procedures are then clarified. Chapters 4 and 5 presents and discusses results related to system performance and moving indentations, respectively. A conclusion on the current state of the prototype is reached in Chapter 6.

Chapter 2

Theory

A thorough literature study has been performed in order to describe the theoretical foundation for the operation of the Linnik interference micrsocope. A complete description requires combining concepts from geometrical imaging, wave-description of imaging, and interference and coherence phenomena. This chapter is an attempt to present a compilation of the necessary theoretical background with the necessary references, in order to properly analyze the system. Although the current report is an experimental layout, this chapter is presented as a thorough literature study, and thus as a starting point for future theoretical work relating to improved modeling of the full system. A brief description of the mechanisms of material removal in fixed-abrasive sawing is also given in this chapter.

2.1 Propagation of light

The propagation of light is a phenomenon that can be described by wave theory. It follows from Maxwell's equations that electric and magnetic fields can propagate in free space as solutions to the wave equations

$$\nabla^2\mathbf{E} - \frac{\epsilon_0\mu_0}{c^2}\ddot{\mathbf{E}} = 0 \tag{2.1a}$$

$$\nabla^2\mathbf{B} - \frac{\epsilon_0\mu_0}{c^2}\ddot{\mathbf{B}} = 0 \tag{2.1b}$$

where $\mathbf{E}$ and $\mathbf{B}$ are the electric and magnetic field vectors and the dots denote two derivations with respect to time. c is the speed of light, ϵ_0 the electric permittivity and μ_0 the magnetic permeability, all in vacuum. The wave equation (2.1) suggest that solutions exist as wave functions where both fields propagate as mutually coupled waves with phase speed $c = \sqrt{\epsilon_0\mu_0}$ [21, 22]. In this text it will be sufficient to treat fields as scalars. Moreover,

both fields can be represented by a single scalar field, $U^{(r)}$, which will be referred to as the optical field.

2.1.1 Complex field representation

The real-valued wavefunction $U^{(r)}(\mathbf{r},t)$ is a solution to the wave equations (2.1) and therefore describes a propagating wavefront. The complex generalization of this function is the complex wavefunction $U(\mathbf{r},t)$ implicitly given by

$$U^{(r)}(\mathbf{r},t) = \Re\{U(\mathbf{r},t)\} = \frac{1}{2}[U(\mathbf{r},t) + U^*(\mathbf{r},t)], \tag{2.2}$$

$U(\mathbf{r},t)$ is an analytic signal which also solves the wave equation. It therefore describes the wavefront completely [21]. The physical field $U^{(r)}$ is obtainable at any time by taking its real part. A monochromatic wave is described by the complex wavefunction

$$U(\mathbf{r},t) = U(\mathbf{r}) \exp(-i2\pi\nu t), \tag{2.3}$$

where ν is the frequency, related to the vacuum wavelength λ_0 through

$$\nu = \frac{c}{\lambda_0}, \tag{2.4}$$

and c is the speed of light in free space. The time-independent function $U(\mathbf{r})$ is the complex amplitude of the wave [22]. For a plane wave propagating along an axis of coordinate z, the complex amplitude is

$$U(z) = e^{ikz}, \tag{2.5}$$

where $k = \frac{2\pi}{\lambda}$ is the wave number in free space. The complete wave function is then written

$$U(z,t) = e^{i(kz - 2\pi\nu t)}. \tag{2.6}$$

2.1.2 Optical properties of c-Si

The electric and magnetic fields of a wave propagating in a material interacts with particles, thereby disturbing the propagation of the wave. This interaction is the origin of the phenomenons of reflection, refraction and absorption. Important optical properties can be summarized in the complex refractive index

$$\tilde{n} = n + i\kappa \tag{2.7}$$

where n is the refractive index and κ is the extinction coefficient. In a material, the wave number is generally a complex number $\tilde{k}$ related to $\tilde{n}$ through [23]

$$\tilde{k} = \tilde{n}k. \tag{2.8}$$

Absorption

Replacing k with $\tilde{k}$ in eq. (2.6) yields the expression

$$U(z,t) = U_0 e^{i(nkz - 2\pi\nu t)} e^{-\kappa kz}, \tag{2.9}$$

for a plane wave propagating in a material. The last factor on the right hand side attenuates for increasing values of z [24]. κ is therefore a measure of the material's ability to absorb an optical field. In c-Si, κ is largely dependent on the wavelength, i.e. $\kappa = \kappa(\lambda)$. This is due to the band gap of the material. Photons excite carriers only when their energy is sufficiently large to overcome the band gap, i.e. for short enough wavelengths [25]. The wavelength dependence $\kappa(\lambda)$ is shown for c-Si in Figure 2.1b.

Refractive index

The refractive index n is expressed as

$$n = \sqrt{\frac{\epsilon\mu}{\epsilon_0\mu_0}}, \tag{2.10}$$

where ϵ and μ are the electric permittivity and magnetic permeability of the material. It alters the phase speed v of the light, which can be expressed as

$$v = \frac{c}{n}, \tag{2.11}$$

where c is the speed of light in vacuum [26]. $n = 1$ is the refractive index of free space, which is the value typically used also for air. Larger n's slow down the speed of light. Because frequency is the conserved quantity of the optical field, it follows from (2.11) that the wavelength is a function of the refractive index:

$$\lambda = \frac{\lambda_0}{n(\lambda_0)}. \tag{2.12}$$

λ_0 is here the wavelength in free space. $n = n(\lambda_0)$ denotes the refractive index' dependence on wavelength. This is known as dispersion and is closely related to the absorption of the material. The dispersion in c-Si therefore related to its band gap. Figure 2.1a shows the dispersion curve of c-Si at 300K.

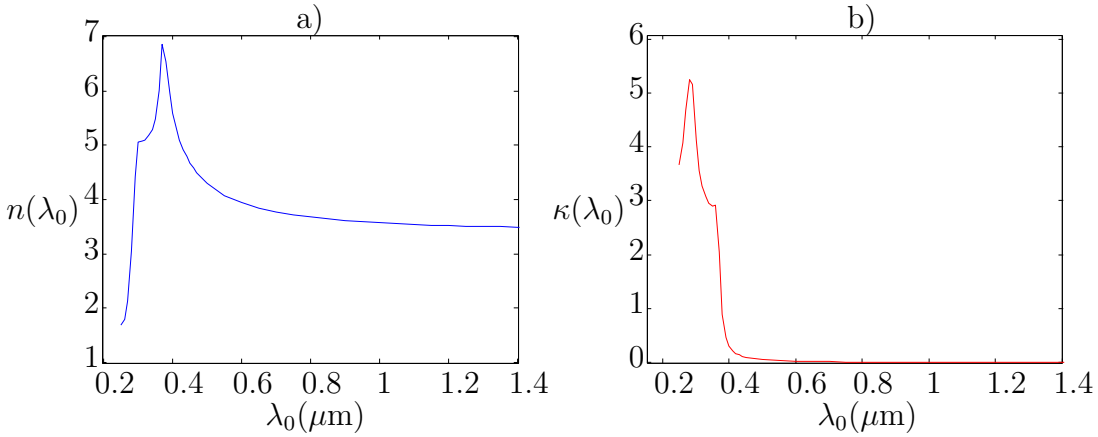

Figure 2.1: Complex refractive index of c-Si as a function of wavelengths in the region 0.25-1.4μm at 300K. **a)** The dispersion $n(\lambda_0)$ of c-Si. At $\lambda_0 = 1.29\mu$m the refractive index is $n = 3.506$. **b)** The extinction coefficient $\kappa(\lambda_0)$ as a function of wavelength. κ is nearly zero for wavelengths longer than $\lambda_0 = 1\mu$m, hence there is very little absorption in this region. Data are retrieved from experimental results by Green and Keevers [27].

2.1.3 Reflection and refraction

Figure 2.2 shows plane waves, represented by rays, incident on an abrupt interface between materials. At the interface there is a sudden change in refractive index that causes the incident wave to be partly reflected and partly transmitted into the other material by *refraction*. All three rays are contained within the *plane of incidence*, and according to the law of reflection the incidence angle equals the reflection angle, $\theta_r = \theta_i$. The angle of refraction θ_t is governed by Snell's law: [23]

$$n_i \sin\theta_i = n_t \sin\theta_t \tag{2.13}$$

The amplitudes of the reflected and transmitted fields, U_r and U_t, are related to the incident field U_i through the relations $U_r = rU_i$ and $U_t = tU_i$, where r is the amplitude reflection coefficient and t is the amplitude transmission coefficient. An important aspect in this process is the polarization[1] of the field. s- and p-polarized waves[2] generally experience different reflection and transmission coefficients. The boundary conditions set by Maxwell's equations lead to a set of equations determining these coefficients for linear materials: [23]

[1]The spatial orientation of the optical fields relative to the interface.

[2]s-wave: **E** parallel to the plane interface. p-wave: **B** parallel to the plane interface.

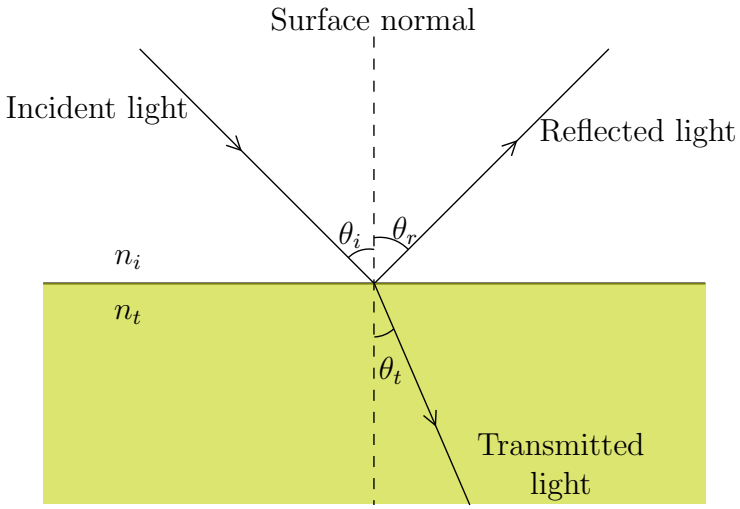

Figure 2.2: Reflection and refraction at the interface between two media of refractive indices n_i and n_t.

$$r_s = \frac{n_i \cos\theta_i - n_t \cos\theta_t}{n_i \cos\theta_i + n_t \cos\theta_t} \tag{2.14a}$$

$$r_p = \frac{-n_t \cos\theta_i + n_i \cos\theta_t}{n_t \cos\theta_i + n_i \cos\theta_t} \tag{2.14b}$$

$$t_s = \frac{2n_i \cos\theta_i}{n_i \cos\theta_i + n_t \cos\theta_t} \tag{2.14c}$$

$$t_p = \frac{2n_i \cos\theta_i}{n_t \cos\theta_i + n_i \cos\theta_t} \tag{2.14d}$$

Equations (2.14) are called the Fresnel equations. The cosine of the transmitted angle is simply given from Snell's law (2.13) as $\cos\theta_t = \sqrt{1 - \frac{n_i}{n_t}\sin^2\theta_i}$. The reflection coefficients are in general complex numbers $r = |r|e^{i\Phi}$. The magnitude $|r|$ determines the amplitude of the reflected wave while the phase Φ introduces an eventual phase change on reflection.

Figure 2.3 shows $|r|$ and Φ for internal reflection of both polarizations at an interface from c-Si to air, calculated for $n_i = 3.506$, $n_t = 1$ and $\lambda_0 = 1.29\mu$m. At angle of incidence equal to *Brewster's angle* $\theta_{p'} = \tan^{-1}(n_t/n_i) = 15.92°$, a phase change of π occurs for the p-polarized reflection. For incidence angles larger than $\theta_c = \sin^{-1}(n_t/n_i) = 16.57°$, the reflection is total for both polarizations, and phase changes occur . θ_c is known as the *critical angle* for total internal reflection [23].

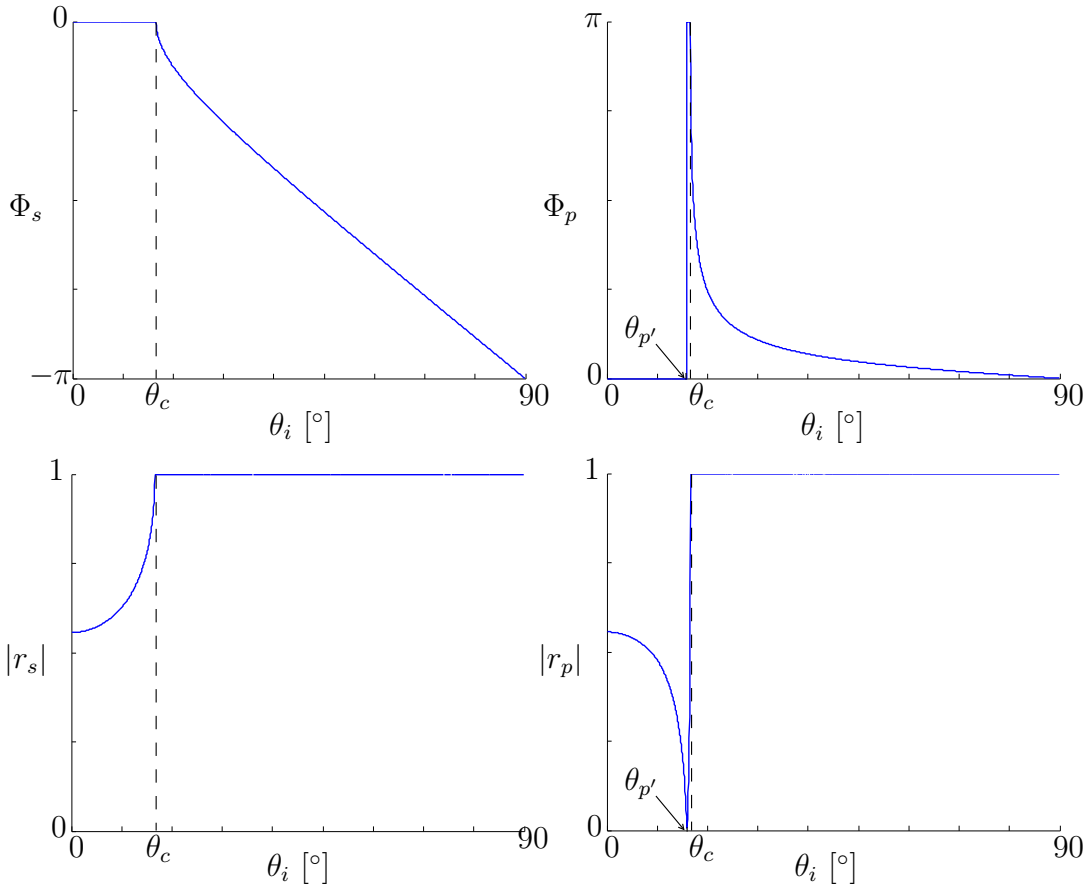

Figure 2.3: Internal reflection in c-Si for $\lambda_0 = 3.506$. The phase Φ (top) and magnitude $|r|$ (bottom) of the reflection coefficient are shown for s-waves (left) and p-waves (right) as functions of incidence angle θ_i. Reflections are calculated for the wavelength $\lambda = 1.29\mu$m at which $n_i = 3.506$. Brewster's angle $\theta_{p'} = 15.92°$ and the critical angle $\theta_c = 16.57°$ are indicated on the horizontal axes.

2.2 Optical Interferometry

Interference of optical fields is a phenomenon resulting from the wave nature of light. The phenomenon is observed as intensity variations, but is a consequence of the principle of superposition when adding fields. When two fields are present at the same time and place their amplitudes are superposed. Intensity variations known as interference patterns are a result of this superposition.

Intensity

The instantaneous intensity of an optical field is a measure of the flow of energy, and is proportional to the square of the field strength,

$$I_{inst}(t) \propto |U(t)|^2 = U^*(t)U(t). \tag{2.15}$$

The proportionality factor of (2.15) is omitted in this text.

The intensity in (2.15) is not an observable quantity. No detecting device is capable of recording the fast fluctuations of an optical field because a finite integration time $2T$ is always needed. The detected intensity is therefore a time-averaged quantity,

$$\overline{I} = \frac{1}{2T} \int_{-T}^{T} U^*(t)U(t)\mathrm{d}t, \tag{2.16}$$

that depends on integration time. For a *stationary* field, the statistical nature of the wavefunction is independent of time. Changing the time origin of eq. (2.16) does therefore not alter the measurement [26]. If in addition the field is ergodic[3], the integration time can approach infinity without affecting the measurement. The intensity is then assured to reach the definite limit [21]

$$I = \lim_{T\to\infty} \frac{1}{2T} \int_{-T}^{T} U^*(t)U(t)\mathrm{d}t, \tag{2.17}$$

or simply

$$I = \langle U^*(t)U(t)\rangle, \tag{2.18}$$

where the brackets denote time-averaging [28].

2.2.1 Coherent Interference

The phenomenon of interference is most easily described by considering monochromatic waves. With this restriction, any spectral distribution is eliminated since only one frequency is present.

[3] "Ergodicity implies that each ensemble average is equal to the corresponding time average involving a typical member of the ensemble." [21]

Interference equation

Due to the linearity of the wave equation, wavefronts are linear in amplitude and not intensity. Hence, when two waves are present at the same time and place, the total amplitude is a superposition of the individual amplitudes [22],

$$U_{tot}(\mathbf{r},t) = U_1(\mathbf{r},t) + U_2(\mathbf{r},t). \tag{2.19}$$

Interference is easily illustrated when the two waves differ only by a time delay, i.e. when

$$U_2(\mathbf{r},t) = U_1(\mathbf{r},t+\tau). \tag{2.20}$$

U_2 is then merely a copy of U_1 at a time τ later. The subscripts are therefore dropped, and (2.19) becomes

$$U_{tot}(\mathbf{r},t) = U(\mathbf{r},t) + U(\mathbf{r},t+\tau). \tag{2.21}$$

The observed intensity is then found from (2.18),

$$I_{tot} = \langle (U(\mathbf{r},t) + U(\mathbf{r},t+\tau))(U(\mathbf{r},t) + U(\mathbf{r},t+\tau))^* \rangle, \tag{2.22}$$

which, using (2.15), reduces to

$$I_{tot} = 2I_1 + 2\Re\{\langle U^*(\mathbf{r},t)U(\mathbf{r},t+\tau)\rangle\}. \tag{2.23}$$

I_1 is the intensity of the respective fields individually. With the monochromatic wave of eq. (2.3), the interference equation is obtained:

$$I_{tot}(\tau) = 2I_1(1 + \cos 2\pi\nu\tau). \tag{2.24}$$

Eq. (2.24) is only dependent on the time delay τ. As τ is increased, the measured intensity varies sinusoidally, with an offset intensity $I_0 = 2I_1$. Peaks and drops appear with period $\frac{2\pi}{\nu}$ and are referred to as constructive and destructive interference, respectively. This intensity signal resulting from this time delay, referred to as an interferogram, is shown in Figure 2.4.

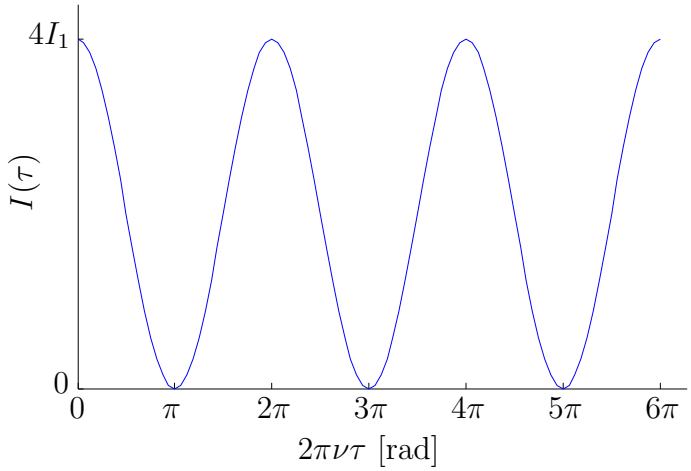

Figure 2.4: The sinusoidal variation in intensity $I(\tau)$ for interference between two coherent waves separated by a time-delay τ.

Visibility

In order for the interferogram to be visible the contrast of the signal must be sufficient. A pattern is hard to measure if peaks and drops are separated by a small difference in intensity compared to the offset intensity. The visibility V of the signal is a measure of its contrast and is defined as [23]

$$V = \frac{I_{max} - I_{min}}{I_{max} + I_{min}}, \tag{2.25}$$

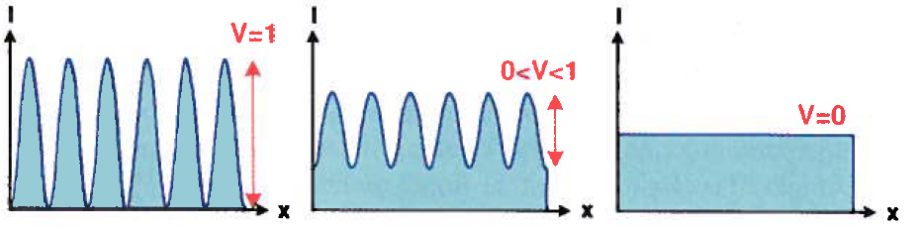

Figure 2.5: Three interferograms of different visibility V. The interference signal is here a spatial intensity variation represented by x. [Reprinted from Singer et. al. [29]]

where I_{max} and I_{min} are the intensities of the maxima (peaks) and minima (drops), respectively. In eq. (2.24), the visibility is maximal ($V = 1$), but for interference between waves of unequal amplitude V is smaller. Interferograms of visibilities $V = 1$, $0 < V < 1$, and $V = 0$ are shown in Figure 2.5.

2.2.2 The Michelson Interferometer

The interferogram in Figure 2.4 can be demonstrated by passing light through an interferometer. This is an optical instrument where light is divided into copies of itself before it is superimposed to interfere. The most basic configuration is the Michelson two-beam interferometer shown in Figure 2.6. This is an example of interferometry by *amplitude-division* [23].

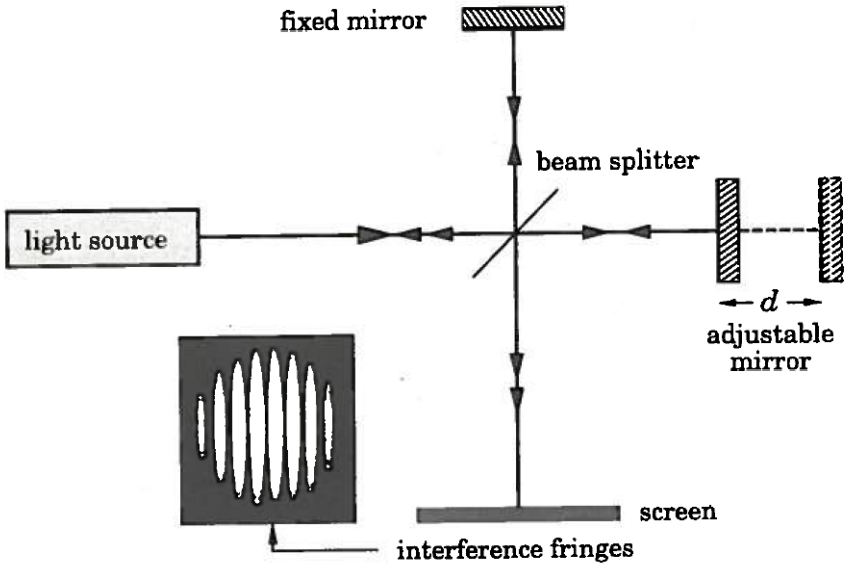

Figure 2.6: The Michelson interferometer. The axial shift d of the reference mirror introduces a time delay τ between the interfering waves. [Reprinted from Lauterborn et al. [28]]

Planes waves emitted from a light source is amplitude-divided into two waves by a *beam splitter*. The two waves then propagate in two different *arms*, where one is reflected by a fixed *object mirror* while the other is reflected by an adjustable *reference mirror* that can be shifted along the direction of propagation. The reflected waves are again divided into two by the beam splitter. Two waves, one from each of the mirrors, are then propagated to a detecting screen where they are superimposed to interfere [28]. The waves are copies of each other, with wavefunctions differing only by the optical path difference $OPD = 2d$ introduced by the shift of the reference mirror. According to (2.5), this causes a phase shift Φ for the reference wave, given by a multiplicative term

$$\exp i\Phi = \exp ik2d. \tag{2.26}$$

Using eq. (2.3), the OPD can be interpreted as a time delay

$$\tau = \frac{2d}{c}. \tag{2.27}$$

Thus, at the detecting screen, the reference wave is delayed by a time τ relative to the object wave [28]. An interferogram is therefore apparent as the shift d of the reference mirror is adjusted. From eq. (2.26), the period of this interferogram is $\lambda_0/2$.

2.2.3 Fizeau fringes

Interference can be observed when light is incident on two adjacent and partly reflecting plane surfaces separated by a gap. Figure 2.7 illustrates how fringes of equal thickness, known as Fizeau fringes, are formed when the bottom surface is tilted relative to the upper surface. Hecht [26] shows that constructive interference occurs given the condition

$$(m + 1/2)\lambda_0 = 2n\alpha x_m, \tag{2.28}$$

if the angles of incidence θ and tilt α are small. m is here a positive integer defining the fringe order. Eq. (2.28) assumes a phase shift of π on reflection at the bottom surface. Fringes of order m are subject to reflection at a gap of constant depth

$$d_m = \frac{\lambda_0}{2n}(m + 1/2), \tag{2.29}$$

hence they relate to equal thicknesses. With an extended source, these fringes are localized in the gap and are imaged by an imaging system [30].

2.3 Optical Coherence

Interference can only be observed when the interfering waves are sufficiently correlated. For instance, wavefronts originating from different sources do not interfere because they appear completely random to one another. If however the waves share some correlation,they can interfere with one another. This mutual correlation of optical fields is related to the theory of optical *coherence*. Coherence deals with the statistical averages of waves that becomes important in the time-averaging of intensity. Therefore, it is easily manifested in the ability of light to produce visible interference fringes [22]. If no correlation exists, the visibility of the interference signal's will average to zero. Optical coherence is of great relevance for the work in this text, especially for measurements of surface depths.

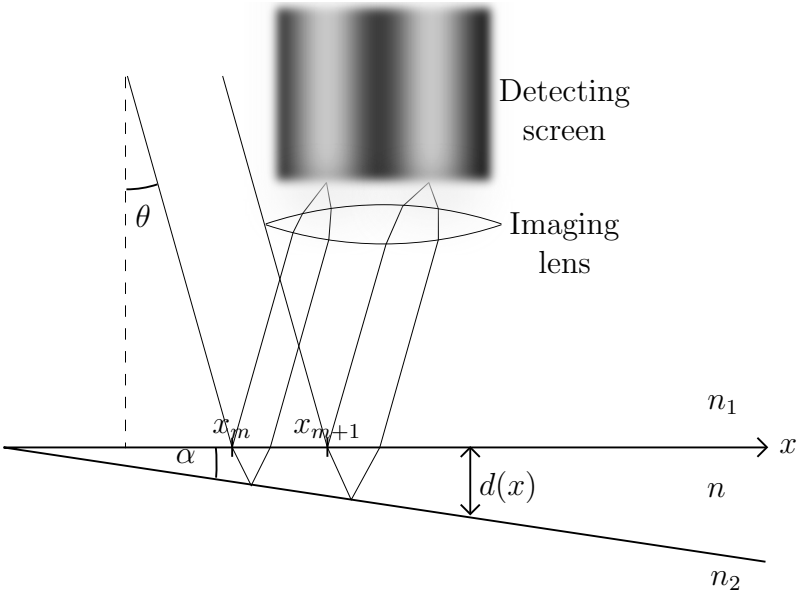

Figure 2.7: Interference fringes resulting from waves reflected from two adjacent plane surfaces separated by a gap. Fringes of the same order correspond to an equal thickness $d(x)$ of the gap, and can be imaged by an imaging system (represented by the imaging lens) to a detecting screen. It is stressed that this is a very simplified illustration.

There are two limiting cases of this theory: *temporal* and *spatial* coherence. The former examines the dependence of correlation on time delays, while the latter regards separations in space. Both are however descendant from the more general concept of coherence functions [28].

2.3.1 Coherence Function

The basic concept in the theory of coherence is the *mutual coherence*. It is represented by the *mutual coherence function*,

$$\Gamma(\mathbf{r_1}, \mathbf{r_2}; \tau) = \Gamma_{12}(\tau) = \langle U(\mathbf{r_1}, t+\tau) U^*(\mathbf{r_2}, t) \rangle, \tag{2.30}$$

where $\mathbf{r_1}$ and $\mathbf{r_2}$ are points in space. The brackets denote the time-averaging operation of eqs. (2.17)-(2.18), hence (2.30) is explicitly expressed as

$$\Gamma_{12}(\tau) = \lim_{T\to\infty} \frac{1}{2T} \int_{-T}^{T} U(\mathbf{r_1}, t+\tau) U^*(\mathbf{r_2}, t) \mathrm{d}t. \tag{2.31}$$

Eq. (2.30) is a convolution that measures the correlation between the wavefunctions of two

optical fields separated in both space and time. For $\mathbf{r_1} = \mathbf{r_2}$ and $\tau = 0$, this is simply the intensity of the field:

$$\Gamma_{11}(0) = I_1. \tag{2.32}$$

Normalizing the mutual coherence gives the *degree of coherence*

$$\gamma_{12}(\tau) = \frac{\Gamma_{12}(\tau)}{\sqrt{I_1 I_2}}, \tag{2.33}$$

which is limited to the region

$$0 \leq |\gamma_{12}(\tau)| \leq 1. \tag{2.34}$$

2.3.2 Temporal Coherence

If $\mathbf{r_1} = \mathbf{r_2}$ but $\tau \neq 0$, the right-hand side of (2.30) becomes an auto-correlation,

$$\Gamma(\tau) = \langle U(t+\tau)U^*(t)\rangle. \tag{2.35}$$

Eq. (2.35) is a measure of a wavefunction's correlation with a time-delayed copy of itself, also called its *temporal coherence function* [21]. Its normalization is the degree of temporal coherence:

$$\gamma(\tau) = \frac{\Gamma(\tau)}{\Gamma(0)} \tag{2.36}$$

For a monochromatic wave, the wavefunction is perfectly periodic and therefore completely resembles itself at any time τ later. Monochromatic waves are therefore temporally *coherent*. This is however not the case for a polychromatic wave, in which the optical field is composed of multiple spectral components. Due to varying periodicities of the spectral components, the wavefunction only partially resembles itself when a time delay is introduced. Polychromatic waves are therefore only partially coherent.

Coherence length

$|\gamma(\tau)|$ is typically a monotonously decreasing function of τ, with a maximum at $\tau = 0$. The *coherence time* τ_c defines the width of this function, which can be given by its FWHM[4]

[4]Full Width at Half Maximum.

[28]. Two waves are considered coherent for $\tau < \tau_c$ and incoherent for $\tau > \tau_c$. The distance propagated during τ_c,

$$l_c = c\tau_c, \tag{2.37}$$

is called the *coherence length* and limits the path length differences that can be introduced between waves while maintaining a sufficient degree of coherence.

Spectral representation

The derivations in this section follows Born and Wolf [21]. Temporal coherence is uniquely a property of the spectral distribution of optical fields. The real-valued amplitude $U^{(r)}(t)$ may be expressed by its spectral components $v(\nu)$ in a Fourier integral

$$U^{(r)}(t) = \int_{-\infty}^{\infty} v(\nu) e^{-i2\pi\nu t} \mathrm{d}\nu. \tag{2.38}$$

However, since $U^{(r)}(t)$ necessarily is defined in a finite time interval only, and hence is not Fourier transformable, a truncated version defined by

$$U_T^{(r)}(t) = \left\{ \begin{array}{ll} U^{(r)}(t), & |t| \leq T \\ 0, & |t| > T \end{array} \right\}, \tag{2.39}$$

must be used in order to utilize Fourier analysis. T is half the length of the truncation interval. The Fourier integral representation of $U_T^{(r)}(t)$ is

$$U_T^{(r)}(t) = \int_{-\infty}^{\infty} v_T(\nu) e^{-i2\pi\nu t} \mathrm{d}\nu, \tag{2.40}$$

where $v_T(\nu)$ are the associated spectral components defined by

$$v_T(t) = \int_{-\infty}^{\infty} U_T^{(r)}(\nu) e^{i2\pi\nu t} \mathrm{d}\nu. \tag{2.41}$$

The time-convolution of $U_T^{(r)}(t)$ now reads

$$\begin{aligned}\int_{-\infty}^{\infty} U_T^{(r)}(t+\tau)U_T^{(r)}(t)\mathrm{d}t &= \int_{-\infty}^{\infty} U_T^{(r)}(t)\int_{-\infty}^{\infty} v_T(\nu)e^{-i2\pi\nu(t+\tau)}\mathrm{d}\nu\mathrm{d}t \\ &= \int_{-\infty}^{\infty}\int_{-\infty}^{\infty} U_T^{(r)}(t)e^{-i2\pi\nu t}\mathrm{d}t v_T(\nu)e^{-i2\pi\nu\tau}\mathrm{d}\nu \\ &= \int_{-\infty}^{\infty} v_T^*(\nu)v_T(\nu)e^{-i2\pi\nu\tau}\mathrm{d}\nu\end{aligned} \tag{2.42}$$

Dividing (2.42) by $2T$ and taking the limit $T \to \infty$ yields the real-valued coherence function

$$\Gamma^{(r)}(\tau) = \langle U_T^{(r)}(t+\tau)U_T^{(r)}(t)\rangle = \int_{-\infty}^{\infty} S(\nu)e^{-i2\pi\nu\tau}\mathrm{d}\nu. \tag{2.43}$$

The stationarity of the signal ensures that a definite limit is reached. $S(\nu)$ is the *power spectral density* given by

$$S(\nu) = \lim_{T\to\infty}\frac{v_T(\nu)v_T^*}{2T}, \tag{2.44}$$

with units of power per frequency, which completely describes the spectral distribution of the field. Eq. (2.43) states that $\Gamma^{(r)}(\tau)$ is the Fourier transform of $S(\nu)$. Together they constitute a Fourier transform pair.

Since the complex amplitude $U(t)$ is an analytic signal[5], its truncated spectral representation reads

$$U_T(t) = 2\int_0^{\infty} v_T(\nu)e^{-i2\pi\nu t}. \tag{2.45}$$

Following the same arguments as above, it can be shown that the complex temporal coherence function in $\Gamma(\tau)$ has the spectral representation

$$\Gamma(\tau) = 4\int_0^{\infty} S(\nu)e^{-i2\pi\nu\tau}\mathrm{d}\nu = 4\Gamma^{(r)}(\tau). \tag{2.46}$$

$\Gamma(\tau)$ is therefore also uniquely determined by the spectral distribution of the field. It follows from the scaling property of the Fourier transform that a broad spectral distribution corresponds to a narrow coherence function and vice versa. This is expressed mathematically as:

[5]With negative spectral components given by $v(-\nu) = v^*(\nu)$.

$$\mathfrak{F}\{S(\nu/a)\} = |a|\Gamma^{(r)}(a\tau) \tag{2.47}$$

When $S(\nu)$ is stretched by a factor a, $\Gamma^{(r)}(\tau)$ is compressed by the same factor a. Hence is the coherence time inversely related to the width $\Delta\nu$ of $S(\nu)$, $\tau_c \propto \frac{1}{\Delta\nu}$ [22]. This is illustrated in terms of the magnitude of the degree of coherence $|\gamma(\tau)|$ in Figure (2.8).

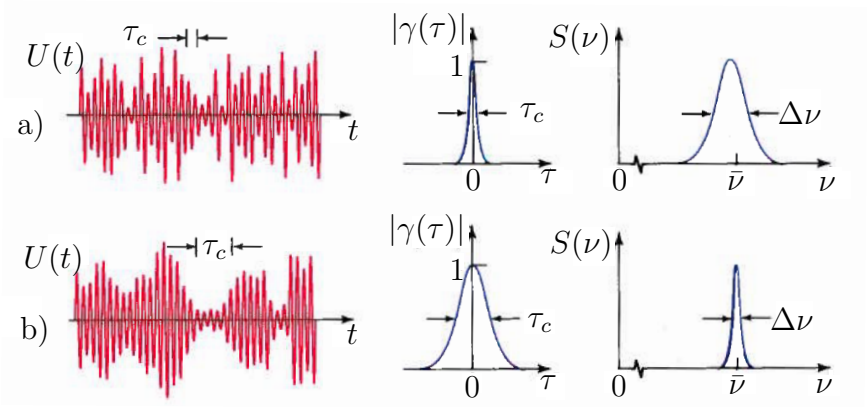

Figure 2.8: The time variation of amplitude (left), degree of temporal coherence (middle) and power spectral density (right) for waves of broad spectral distribution (a) and narrow spectral distribution (b). The inverse relation between widths of the coherence function and spectral distribution is noted. [Reprinted from Saleh and Teich [22]]

2.3.3 Spatial Coherence

Analog to the temporal separation discussed in Section 2.3.2, waves may also exhibit correlation when separated in space. Setting $\tau = 0$ in (2.30) yields the *mutual intensity*

$$\Gamma(\mathbf{r_1}, \mathbf{r_2}) = \langle U^*(\mathbf{r_1}, t)U(\mathbf{r_2}, t)\rangle, \tag{2.48}$$

which is a measure of *spatial coherence* [22].Typically, the spatial coherence decays with the spatial separation of optical fields. Spatial coherence is an important topic for the wave-optics description of imaging. The formalism of imaging is different, dependent on whether the optical fields at object points are spatially coherent, partially coherent or incoherent [31]. Spatial coherence is however not presented in further detail in this text.

2.3.4 Low Coherence Interferometry

Temporal coherence effects alter the formalism of interference, and also has a dramatic effect on the shape of interferograms. Interference using low coherent light is termed Low coherence Interferometry (LCI), and is of great importance to the depth profiling attempted in this report. LCI regards interference with polychromatic waves.

Quasi-monochromaticity

For a polychromatic light source, the spectral distribution consists of a range of frequencies, in contrast to the single frequency of monochromatic waves. The wavefunction (2.3) can therefore no longer be used to describe the optical field. However, any modest deviations from monochromaticity can be modeled as a *quasi-monochromaticity* with a mean frequency $\bar{\nu}$ and bandwidth $\Delta\nu$. In the quasi-monochromatic approximation, the wavefunction reads [32]

$$U(\mathbf{r},t) = A(\mathbf{r},t)e^{-i2\pi\nu t}, \tag{2.49}$$

where $A(\mathbf{r},t)$ is a time-varying complex amplitude. As a function of time, $A(\mathbf{r},t)$ is a slowly varying envelope compared to the rapid fluctuations of the term $e^{-i2\pi\nu t}$. Therefore, the envelope varies very little within one temporal period. Quasi-monochromaticity is assured under the condition [21]

$$\frac{\Delta\nu}{\bar{\nu}} = \frac{\Delta\lambda}{\bar{\lambda}} \ll 1. \tag{2.50}$$

The coherence function of a quasi-monochromatic wave is investigated by multiplying the spectral representation (2.46) with $e^{i2\pi\bar{\nu}\tau}$, yielding

$$\Gamma(\tau)e^{i2\pi\nu\tau} = 4\int_0^\infty S(\nu)e^{i2\pi(\bar{\nu}-\nu)\tau}\mathrm{d}\nu. \tag{2.51}$$

Due to the small bandwidth $\Delta\nu$, the right hand side of (2.51) varies slowly as a function of τ and hence does also the expression on the left hand side. $\Gamma(\tau)$ can therefore be written as the product

$$\Gamma(\tau) = (\Gamma(\tau)e^{i2\pi\bar{\nu}\tau}) \cdot e^{-i2\pi\bar{\nu}\tau}, \tag{2.52}$$

of a slowly varying function with the rapidly varying function $e^{i2\pi\bar{\nu}\tau}$ [21]. Representing the slowly varying function sin polar form, this can be rewritten

$$\Gamma(\tau) = |\Gamma(\tau)|e^{i\alpha(\tau)} \cdot e^{-i2\pi\bar{\nu}\tau}, \tag{2.53}$$

Interference equation for quasi-monochromatic waves

Returning to eq. (2.23) and using eq. (2.35), the interference equation can be rewritten

$$I(\tau) = 2\left[I_1 + \Re\left\{\Gamma(\tau)\right\}\right], \tag{2.54}$$

in terms of the coherence function. Using the coherence function (2.53) gives the expression [21]

$$\begin{aligned} I(\tau) &= 2\left[I_1 + |\Gamma(\tau)|\cos\left(2\pi\bar{\nu}\tau - \alpha(\tau)\right)\right] \\ &= 2I_1\left[1 + |\gamma(\tau)|\cos\left(2\pi\bar{\nu}\tau - \alpha(\tau)\right)\right], \end{aligned} \tag{2.55}$$

for the interference between quasi-monochromatic waves. Since it was established that $\alpha(\tau)$ represented the complex argument of a slowly varying function, it varies very little in comparison with $2\pi\bar{\nu}\tau$. For $\tau = 0$ the waves are completely coherent, hence the coherent interference equation (2.23) should be reproduced for this special case. It is therefore determined that $\alpha(0) = 0$. From these two arguments, $\alpha(\tau)$ can to an approximation be set to zero, yielding the interference equation

$$I(\tau) = 2[I_1 + \gamma(\tau)\cos\left(2\pi\bar{\nu}\tau\right)]. \tag{2.56}$$

(2.56) is similar to the monochromatic interference equation (2.24), but with an interference term modulated by an envelope which is the magnitude of the degree of coherence $|\gamma(\tau)|$. Figure 2.9 shows the interferogram from a Michelson interferometer with a light source of Gaussian spectral distribution. At $d = 0$, the degree of coherence is maximal, which is identified as the peak of the envelope for which constructive interference occurs.

2.4 Imaging Optics

Imaging is the process of reproducing the detail in an object to an image. In optics this is done by a transfer of optical fields. A perfect image is formed when all light originating from an object point is brought to converge at a common image point [33]. The aim of optical imaging is to obtain a 1-to-1 relationship between object and image points. This process requires an adequate optical imaging system.

In this text, the formation of images is described by two different theories. Geometrical optics offers a simple formalism of imaging from geometric rules of refraction. The

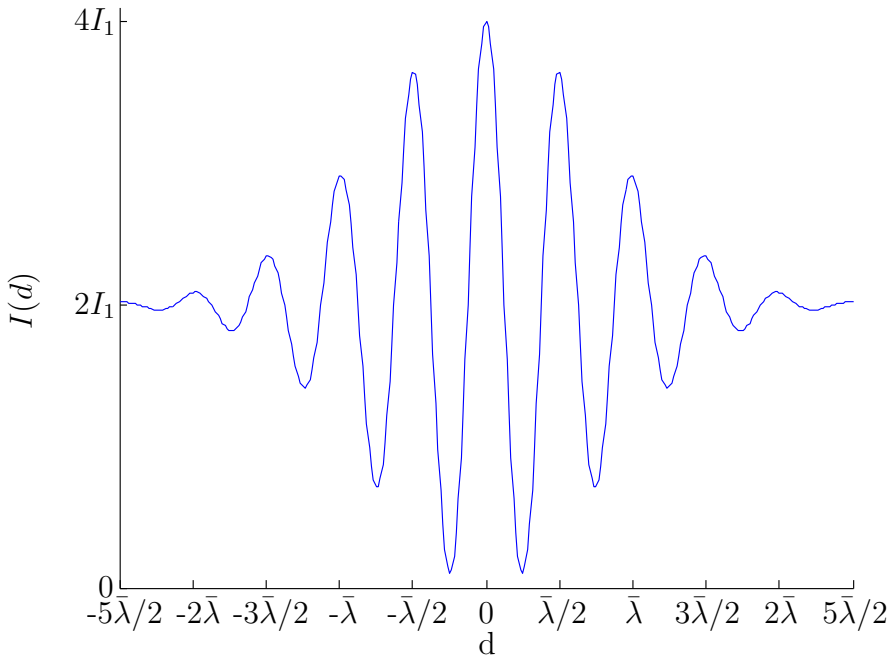

Figure 2.9: The interferogram recorded from a Michelson interferometer with a light source of Gaussian spectral distribution. The interference signal is modulated by an envelope which is the temporal coherence function.

wave-optics description is more cumbersome, but essential to explain concepts like optical resolution and interference microscopy.

2.4.1 Geometrical optics

In geometrical optics, optical fields are not treated as waves but as rays of light that propagate along straight lines. The direction of rays are only altered through reflection or refraction at the boundary of two media of different refractive index n, according to Snell's law [22]. Rays diverging from an object point may undergo several reflections and/or refractions before converging to an image point.

The components of an imaging system are usually symmetric about a straight line known as the optical axis. In paraxial optics, rays always travel sufficiently close to and make small angles with this axis [33]. This is known as the paraxial approximation[6]

$$\sin\theta \approx \theta, \tag{2.57}$$

where θ (in radiands) is either a ray's angle with the optical axis or the angle of incidence on refracting/reflecting surfaces. In paraxial optics, Snell's law (2.13) takes the form

[6]It is discussed in Section 2.4.2 that deviations from this approximation causes aberrations

$$n_1\theta_i = n_2\theta_t. \tag{2.58}$$

Image formation

It is shown by Pedrotti et al. [23] that refraction through a spherical surface separating two media of refractive indices n_1 and n_2 satisfies imaging by the relation

$$\frac{n_1}{z_o} + \frac{n_2}{z_i} = \frac{n_2 - n_1}{R}. \tag{2.59}$$

z_o and z_i are the axial distances from the object and image plane to the axial intersect of the spherical surface, respectively. R is the radius of the spherical surface. The sign convention is that z_o and z_i are positive for *real* objects and images, and negative for *virtual* objects and images. The lateral magnification of an image formed by a spherical surface is given by

$$M = -\frac{n_1 z_i}{n_2 z_o}, \tag{2.60}$$

where a negative sign denotes that the image is an inverted version of the object.

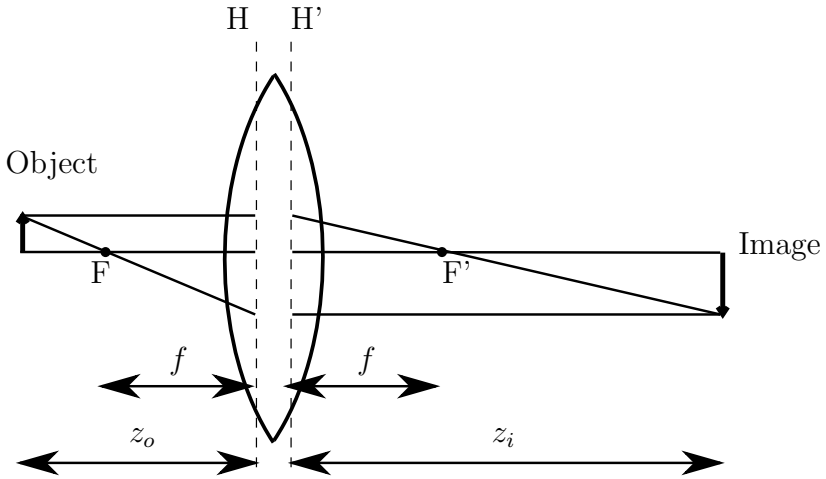

Figure 2.10: The imaging properties of a converging (biconvex) lens. Refraction is described by the lens formula (2.61) between H and H'. Rays parallel to the optical axis on one side pass through the focal point on the other side. The lateral magnification of the image is determined by the distances z_o and z_i.

An imaging system is typically formed by a system of lenses, made from materials of high refractive index and spherical surfaces. Figure 2.10 shows how an image is formed by a single converging lens, surrounded by air on both sides. Refraction of rays are modeled as

occurring between the first and second principal planes, H and H', of the lens. The amount of refraction is governed by the focal length f of the lens, which is the axial distance from H and H' to their associated focal points F and F' [26]. The location of object and image planes are governed by the lens formula [33]

$$\frac{1}{z_o} + \frac{1}{z_i} = \frac{1}{f}, \tag{2.61}$$

where the object and image distances z_o and z_i are indicated in the figure. The lateral magnification of this imaging process is

$$M = -\frac{z_i}{z_o}. \tag{2.62}$$

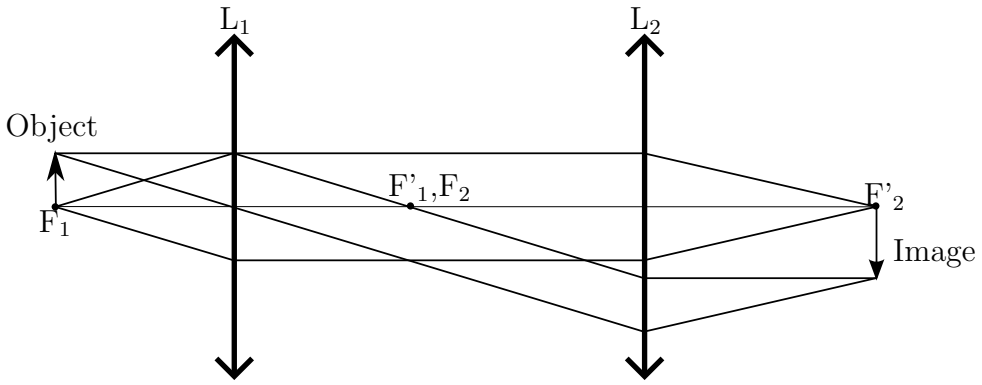

Figure 2.11: Imaging by a two-lens system. Lenses are denoted by two-sided arrows. The object is located in the front focal plane of L_1, making rays originating from the same object point parallel in the space between L_1 and L_2. An image is formed at the back focal plane of L_2.

Sophisticated imaging systems such as microscopes utilize a series of lenses for imaging. Such systems can be analyzed by successive application of eq. (2.61), where the image formed by one lens constitutes the object for the next lens. Figure 2.11 shows how an image is formed by a specific two-lens system. The object is placed in the front focal plane of L_1, i.e. at an object distance $z_{o1} = f_1$. According to (2.61), the image formed by this lens is located at infinity, $z_{i1} = \infty$. The object for L_2 is thus also located at infinity, $z_{o2} = \infty$. L_2 then forms a final image in its back focal plane, hence the final image distance is $z_{i2} = f_2$. Hecht [26] shows that the lateral magnification of such a system is

$$M = -\frac{z_{i2}}{z_{o1}} = \frac{f_2}{f_1}. \tag{2.63}$$

Pupils and stops

The angular limitation of rays throughput by an imaging system is set by apertures within the system. Apertures are either formed by the lateral dimension of lenses, or they are diaphragms specifically introduced to control light. A discussion on apertures and their effects on imaging has been given by Born and Wolf [21], and is briefly presented here.

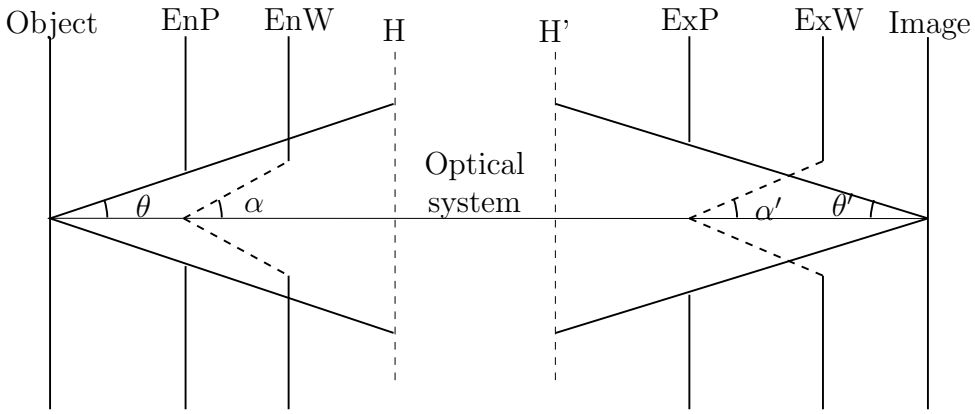

Figure 2.12: Entrance and exit pupils (EnP, ExP) and windows (EnW, ExW) for a general imaging system represented by its principal planes. θ is the half-angle of the cone of rays accepted by the system, and α determine the field of view.

The physical aperture that limits the cone of rays throughput from an axial object point is the *aperture stop* of the system. Its images in object and image space are the *entrance pupil* and *exit pupil* of the system, respectively. The pupils of a general imaging system is shown in Figure 2.12. The pupils control the irradiance of the image. Furthermore, the half-angle θ extended by the entrance pupil defines the object-side numerical aperture of the system

$$NA = n \sin \theta, \tag{2.64}$$

which ultimately controls the diffraction-limited resolution.

The physical aperture which limits the cone of rays from the axial intersection of the entrance pupil is the *field stop*. In analogy with the pupils, the field stop also has images in object and image space. These are the *entrance window* and *exit window*, respectively, and are also shown in Figure 2.12. The half-angle α determines the object side angular field of view, which is the lateral extent of the object that is seen in the image.

2.4.2 Aberrations

The theory presented in the above section assumes an ideal imaging system. However, any *aberrations* within the system will cause image errors. There are two main types of aberrations. *Chromatic aberrations* occur due to dispersion, and are therefore only important for imaging with very broadband light. System components are often designed for a specific wavelength region in order to minimize such aberrations. *Monochromatic aberration* is however a subject for all light. There are several types of such aberrations, however only spherical aberration is presented in this text [23, 26].

Spherical aberration

The paraxial approximation (2.57) is valid only for small angles θ. For increasing angles, the higher order terms of the Taylor series expansion

$$\sin\theta = \theta - \frac{\theta^3}{3!} + \frac{\theta^5}{5!} - \frac{\theta^7}{7!} + \cdots \tag{2.65}$$

become increasingly important. Spherical aberrations are mainly due to the third order term in (2.65), when the paraxial approximation is no longer adequate for a correct description of refraction.[7] Followingly, rays of light originating from the same object point but striking a refracting surface at different distances from the optical axis will be brought to intersect again at different points in the axial direction. Hence spherical aberration invokes differing focal lengths for non-paraxial rays. Converging surfaces generally focus non-paraxial rays in front of the paraxial focus, known as positive spherical aberration. The opposite is the case for diverging surfaces, known as negative spherical aberration. As an effect of this aberration, point sources are no longer imaged as Airy patterns. Instead, light is distributed in the lateral surroundings, thereby degrading lateral resolution. Spherical aberrations can be reduced by lowering NA so that only paraxial rays are captured by the system. However, this also degrades resolution. Another approach is to combine converging and diverging surfaces in order to cancel out the effect [23, 26].

2.4.3 Wave Theory

Geometrical optics offers a good description of the ideal imaging process. The limitations of the mapping from object to image is however better highlighted through the diffraction effects described by wave theory. In wave theory, image formation is a mapping of light distribution from the object to image plane.

[7] The same is also the case with reflection.

The derivations in this section follows Goodman [31] and are given for monochromatic waves only. They are however also valid under the quasi-monochromatic approximation. It is stressed that the formalism of imaging is largely dependent on the spatial coherence of the object. Imaging is in the following explained assuming a spatially coherent object, with the corresponding result for an incoherent object stated at the end. The more general formalism of partial coherence is outside the scope of this text.

Any time-invariant optical system employing spatially coherent light is linear in complex amplitude. The amplitudes at input and output of a general system can therefore be related by the superposition integral [31]

$$U(x,y) = \iint_{-\infty}^{\infty} U(\xi,\eta)h(x,y;\xi,\eta)\mathrm{d}\xi\mathrm{d}\eta, \tag{2.66}$$

where (x,y) and (ξ,η) are coordinates in output and input planes, respectively. $h(x,y;\xi,\eta)$ is called the *point spread function* of the system, and is an impulse response that completely characterizes the system. $h(x,y;\xi,\eta)$ defines the amplitude mapped to (x,y) by a point source at (ξ,η). The complex amplitude from such a point source is expressed as

$$U(\mathbf{r}) = \frac{e^{ikr}}{r}, \tag{2.67}$$

with $\mathbf{r}$ representing the point of evaluation. $\mathbf{r} = 0$ denotes the spatial position of the point source.

Diffraction

Diffraction has been defined as any deviation from the rectilinear behavior of light rays that is not caused by reflection or refraction. It is a phenomenon caused by the lateral confinement of waves, usually in the form of apertures. The phenomenon is a result of the Huygens-Fresnel principle, stating that every point on a wavefront can be considered a point source of a secondary wavefront. At any point beyond, the wavefront is a superposition of all these secondary wavefronts [23]. The principle is expressed by the Rayleigh-Sommerfeld diffraction formula:

$$U(P_0) = \frac{1}{i\lambda}\iint_{\Sigma} U(P_1)\frac{\exp(ikr_{01})}{r_{01}}\cos\theta\mathrm{d}s \tag{2.68}$$

$U(P_1)$ and $U(P_0)$ are complex amplitudes at a point on the first wavefront and the point of evaluation, respectively. r_{01} is the distance separating the points, θ is the angle between

the vector $\mathbf{r}_{01}$ and the optical axis, and ds is an infinitesimal area on the wavefront denoted by Σ. The geometry is explained in Figure 2.13.

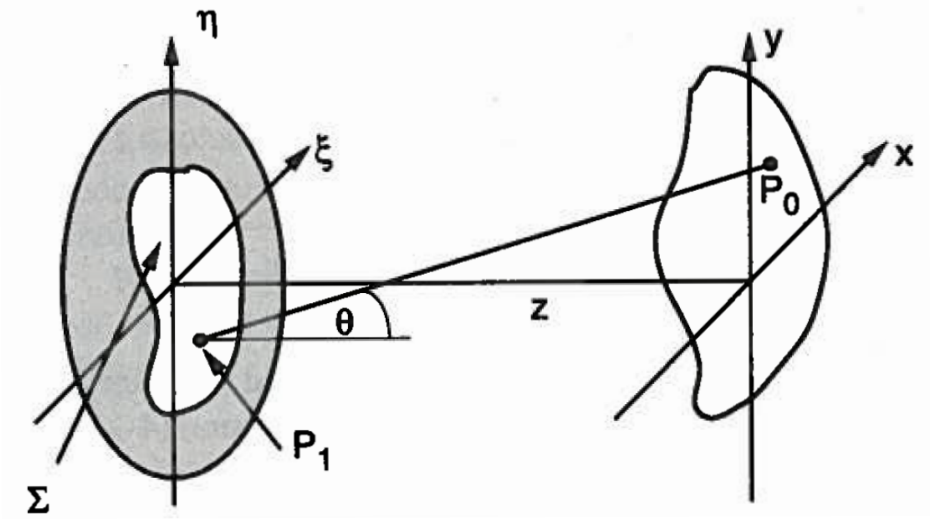

Figure 2.13: The geometry of the Huygens-Fresnel principle. Each point P_1 on a wavefront constricted to an aperture Σ in the plane (ξ, η) is a point source for a secondary wavefront. Diffraction effects are observed when this wavefront is propagated to points P_0 in the plane (x, y). [Reprinted from Goodman [31]]

Diffraction will occur when a wavefront is confined by an aperture. The limitation of the aperture can be incorporated in the expression of $U(P_1)$ as

$$U(P_1) = U(\xi, \eta) = t_l(\xi, \eta) U'(\xi, \eta), \tag{2.69}$$

where $U'(\xi, \eta)$ represents the wavefront incident on the aperture and $t_l(\xi, \eta)$ is a multiplicative factor representing the structure of the aperture. For a simple circular aperture, $t_l(\xi, \eta)$ is represented by the pupil function

$$P(\xi, \eta) = \left\{ \begin{array}{ll} 1 & \sqrt{\xi^2 + \eta^2} \leq a \\ 0 & \sqrt{\xi^2 + \eta^2} > a \end{array} \right\}, \tag{2.70}$$

where a is the radius of the aperture. (2.68) and (2.69) then describe propagation of light through an aperture.

Eq. (2.68) can be simplified by the Fresnel approximation when evaluating at a point in the *near field* of the diffracting aperture. Binomial expansion simplifies the expression of the distance r_{01}, yielding the Fresnel diffraction integral

$$U(x,y) = \frac{e^{ikz}}{i\lambda z} \iint_{-\infty}^{\infty} U(\xi,\eta) \exp\left\{ i\frac{k}{2z}\left[(x-\xi)^2 + (y-\eta)^2\right]\right\} \mathrm{d}\xi\mathrm{d}\eta, \tag{2.71}$$

where z is the optical axis coordinate measured from the aperture. The point-spread function of Fresnel diffraction is

$$h(x,y;\xi,\eta) = h(x-\xi, y-\eta) = \frac{e^{ikz}}{i\lambda z} \exp\left\{ \frac{ik}{2z}\left[(x-\xi)^2 + (y-\eta)^2\right]\right\}. \tag{2.72}$$

Fresnel diffraction can be further simplified if evaluating in the *far field*. By applying the Fraunhofer approximation

$$z \gg \frac{k(\xi^2+\eta^2)_{max}}{2} \tag{2.73}$$

to eq. (2.71), the quadratic terms of the aperture coordinates (ξ,η) can be dropped, yielding the amplitude [31]

$$U(x,y) = \frac{e^{ikz} e^{i\frac{k}{2z}(x^2+y^2)}}{i\lambda z} \iint_{-\infty}^{\infty} U(\xi,\eta) \exp\left[-i\frac{k}{z}(x\xi + y\eta)\right] \mathrm{d}\xi\mathrm{d}\eta. \tag{2.74}$$

Fraunhofer diffraction is thus a special case of of the more general Fresnel diffraction.

Image formation

An image is formed if at a plane at the output of the system there appears a distribution of field amplitude $U_i(u,v)$ that resembles the distribution $U_o(\xi,\eta)$ in the object plane. These are related by a superposition integral as in (2.66). In this context, the point-spread function is an indicator of how much the light from an object point is distributed among the neighboring points of the corresponding image point. The quality of the image is then indicated by the semblance of the point-spread function with the two-dimensional Dirac delta function:

$$h(u,v;\xi,\eta) \approx K\delta(u + M\xi, v + M\eta), \tag{2.75}$$

where M is the lateral magnification and K is a constant. The limiting case where (2.75) is an exact equation gives the perfect geometrical image, $U_g(u,v)$.

An imaging system that is limited by diffraction can be modeled as described in Section 2.4.1 by determining its terminal properties. These are the entrance and exit pupils, the principal planes and the focal length. Either of the two pupils completely characterize the diffraction, since they are images of each other. The image can therefore be described according to geometrical optics, with diffraction effects resulting from the exit pupil. The geometry of this model is illustrated in Figure 2.14.

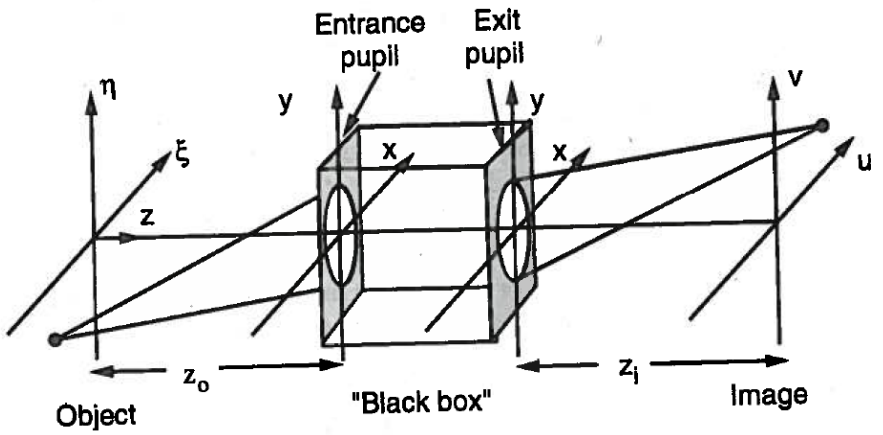

Figure 2.14: Geometry of the wave theory model of imaging. The imaging system is represented by a "black box" where geometrical optics apply. Diffraction effects arise from propagation through the exit pupil of the system. [Reprinted from Goodman [31]].

The image distribution is then the superposition integral of $U_g(u,v)$ and the point-spread function of the system. The object amplitude $U(\xi,\eta)$ is first propagated by Fresnel diffraction (2.71) a distance z_o to the entrance pupil, yielding the amplitude $U'(x,y)$ at the entrance pupil of the imaging system. The imaging system is incorporated in the amplitude at the exit pupil by a multiplicative term consisting of a quadratic phase-shift $\exp\left[-\frac{ik}{2f}(x^2+y^2)\right]$ and an exit pupil function $P(x,y)$. f is the focal length of the compound system. Hence the amplitude at the exit pupil is

$$\begin{aligned} U(x,y) &= P(x,y)\exp\left[-\tfrac{ik}{2f}(x^2+y^2)\right]U'(x,y) \\ &= \tfrac{e^{ikz_o}}{i\lambda z_o}P(x,y)\exp\left[-\tfrac{ik}{2f}(x^2+y^2)\right] \\ &\quad \times \int_{-\infty}^{\infty}\!\!\int U_o(\xi,\eta)\exp\left\{i\tfrac{k}{2z_o}\left[(x-\xi)^2+(y-\eta)^2\right]\right\}\mathrm{d}\xi\mathrm{d}\eta. \end{aligned} \tag{2.76}$$

The amplitude in (2.76) is then Fresnel diffracted (2.71) a distance z_i to the image plane, yielding an expression for the image amplitude distribution [34]

$$\begin{aligned} U_i(u,v) &= \frac{e^{ikz_i}}{i\lambda z_i}\iint_{-\infty}^{\infty} U(x,y)\exp\left\{i\tfrac{k}{2z_i}\left[(u-x)^2+(v-y)^2\right]\right\}\mathrm{d}x\mathrm{d}y \\ &= \frac{e^{ik(z_o+z_i)}}{\lambda^2 z_o z_i}\iiiint_{-\infty}^{\infty} U_o(\xi,\eta)P(x,y)\exp\left[-\tfrac{ik}{2f}(x^2+y^2)\right]\exp\left\{i\tfrac{k}{2z_o}\left[(x-\xi)^2+(y-\eta)^2\right]\right\} \\ &\quad\times\exp\left\{i\tfrac{k}{2z_i}\left[(u-x)^2+(v-y)^2\right]\right\}\mathrm{d}\xi\mathrm{d}\eta\mathrm{d}x\mathrm{d}y, \end{aligned} \tag{2.77}$$

where a negative sign has been omitted. Eq. (2.77) can be expanded to yield

$$\begin{aligned} U_i(u,v) &= \frac{e^{ik(z_o+z_i)}}{\lambda^2 z_o z_i}\exp\left[\tfrac{ik}{2z_i}(u^2+v^2)\right]\iiiint_{-\infty}^{\infty} U_o(\xi,\eta)P(x,y)\exp\left\{\tfrac{ik}{2z_o}(\xi^2+\eta^2)\right\}\exp\left\{\tfrac{ik}{2}\epsilon(x^2+y^2)\right\} \\ &\quad\times\exp\left\{-\tfrac{ik}{z_i}\left[x(u-M\xi)+y(v-M\eta)\right]\right\}\mathrm{d}\xi\mathrm{d}\eta\mathrm{d}x\mathrm{d}y. \end{aligned} \tag{2.78}$$

where $\epsilon = \frac{1}{z_o}+\frac{1}{z_i}-\frac{1}{f}$ is any deviation from the lens formula (2.61) of geometrical optics. Assuming that $u = M\xi$ and $v = M\eta$ in the first exponential of the integral in (2.78), it can be rewritten as

$$\begin{aligned} U_i(u,v) &= \frac{e^{ikz_o(1-M)}}{\lambda^2 M z_o^2}\exp\left\{-\tfrac{ik}{2Mz_o}(u^2+v^2)\left(1-\tfrac{1}{M}\right)\right\} \\ &\quad\times\iint_{-\infty}^{\infty} U_o(\xi,\eta)h(u-M\xi,v-M\eta)\mathrm{d}\xi\mathrm{d}\eta, \end{aligned} \tag{2.79}$$

where $h(u+M\xi, v+M\eta)$ is a point spread function given by

$$h(u,v) = \iint_{-\infty}^{\infty} P(x,y)\exp\left\{\frac{ik}{2}\epsilon(x^2+y^2)\right\}\exp\left\{-\frac{ik}{z_i}(xu+yv)\right\}\mathrm{d}x\mathrm{d}y. \tag{2.80}$$

Ignoring the terms preceding the integral in (2.79), the image distribution is seen to be a convolution

$$U_i(u,v) = h(u,v) * U_g(u,v), \tag{2.81}$$

of the point spread function and the image predicted by geometrical optics $U_g(u,v) = U_o\left(\frac{u}{M},\frac{u}{M}\right)$. The object resemblance is best when imaging in-focus, i.e. for $\epsilon = 0$. Setting this value in eq. (2.80), it is seen that the image (2.79) is, up to a constant factor, just the Fraunhofer diffraction pattern (2.74) centered on the image coordinates [31].

For a spatially *incoherent* object, the mapping from object to image is linear in intensity rather than amplitude. The intensity in the image is then given by the convolution

$$I_i(u,v) = K \iint_{-\infty}^{\infty} |h(u - M\xi, v - M\eta)|^2 I_g(M\xi, M\eta) \mathrm{d}\xi \mathrm{d}\eta, \tag{2.82}$$

where $I_g(M\xi, M\eta)$ is the intensity predicted by geometrical optics and K is a constant. $|h(u - M\xi, v - M\eta)|^2$ is the intensity impulse response.

2.4.4 Optical resolution

The ability of an imaging system to transfer detail from object to image can be analyzed by considering its optical resolution. Lateral resolution defines the minimal distance between points in the object plane that can be distinguished in the image. It is stressed that the concept of lateral resolution is meaningful only for incoherent objects. For coherent objects, the transfer of detail is better described by the frequency response of the system. Axial resolution describes how well detail is transferred when perfect focus is not met.

Diffraction limit of lateral resolution

The limit of *lateral resolution* is the distance between points in the object plane that are considered just resolved in the image. In the absence of aberrations, lateral resolution is limited by diffraction-effects within the system. Hence the resolving properties are uniquely determined by the impulse response of the system [35].

The following is a derivation of the diffraction-limited resolution for *incoherent* imaging. Diffraction causes the image of a point source to be a distribution of amplitude around the ideal image point. This distribution is the intensity impulse response, but shares the same functional dependence as the point-spread function. Transforming (2.80) to polar coordinates and setting $\epsilon = 0$ yields [26]

$$h(w,\psi) = \int_0^a \int_0^{2\pi} e^{-i(k\rho w/z_i)\cos(\theta - \psi)} \rho \mathrm{d}\rho \mathrm{d}\theta, \tag{2.83}$$

where (ρ, θ) and (w, ψ) are polar coordinates of the image plane and exit pupil plane, respectively. Eq. (2.83) can be expressed in terms of the zero order Bessel function of the first kind, $J_0(x)$, as

$$h(w,\psi) = 2\pi \int_0^a J_0(k\rho w/z_i) \rho \mathrm{d}\rho. \tag{2.84}$$

By the recurrence relation of the Bessel functions,

$$\frac{\mathrm{d}}{\mathrm{d}x}[x^m J_m(x)] = x^m J_{m-1}(x), \tag{2.85}$$

eq. (2.84) can be rewritten as

$$h(r) = 2\pi \frac{2J_1(kaw/z_i)}{kaw/z_i}, \tag{2.86}$$

where $J_1(x)$ is the first order Bessel function of the first kind. Eq. (2.86) describes a radially symmetric pattern known as the *Airy pattern*. The point source is imaged as a circular pattern of bright and dark annuluses surrounding a bright central spot called the *Airy disk* [26].

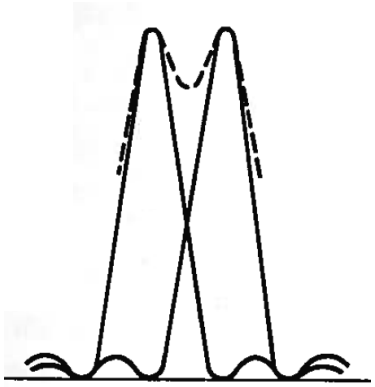

Figure 2.15: Rayleigh's criterion for the diffraction-limit of lateral resolution in incoherent imaging. The Airy patterns of two object points are shown in one dimension. The points are considered just resolved when the maximum of one Airy pattern coincides with the first minimum of the other. [Reprinted from Hecht [26]]

Determining the limit of resolution is a somewhat arbitrary task. However, Lord Rayleigh provides an often used criterion for the resolution limit [36]. It states that two object points are just resolved in the image when the center of one Airy disk is located at the first minimum of the other point's Airy pattern [26]. Figure 2.15 illustrates Rayleigh's criterion. The lateral resolution therefore equals the radius of the Airy disk. $J_1(x)$ has its first minimum for $x = 1.22\pi$ [21], hence the limit of resolution is given in image space as

$$\delta w = \frac{0.61\lambda z_i}{a}. \tag{2.87}$$

Applying the paraxial approximation gives $a/z_i = sin\theta_i$ where θ_i is the half-angle extended by the image-side numerical aperture. It is here assumed that the image point is laterally

close to the optical axis. Invoking the sine condition, $n_i \delta w \sin\theta_i = n \delta x \sin\theta$, eq. (2.87) gives a final expression for the diffraction-limited resolution

$$\delta x = \frac{0.61\lambda}{n \sin\theta} = \frac{0.61\lambda}{NA}. \tag{2.88}$$

$\sin\theta$ is the half-angle extended by the object side NA, n and $n_i = 1$ are the object and image-side refractive indices, respectively. δx is the diffraction-limited distance in the object. It is seen from (2.88) that the limit of resolution only depends on the object-side numerical aperture and the wavelength of the light. A good lateral resolution is achievable from a high-quality system with large NA. However, the presence of λ in the formula restricts the resolution to around the value of the wavelength used.

Frequency response

The frequency response of an imaging system, coherent or incoherent, can be analyzed by a Fourier transform of eqs. (2.81) and (2.82), respectively. By the convolution theorem of Fourier analysis[8], the spectrum of spatial frequencies in the image is given by the product of the corresponding spectrum in the object and a transfer function. The latter is, with coherent imaging, the Fourier transform of the point spread function,

$$H(f_X, f_Y) = \iint_{-\infty}^{\infty} h(u,v) e^{-i2\pi(f_X u + f_Y v)} \mathrm{d}u\mathrm{d}v, \tag{2.89}$$

which is known as the amplitude transfer function. f_X and f_Y are spatial frequencies. Under diffraction limited conditions and a circular aperture stop, $H(f_X, f_Y)$ is the transfer function of a sharp low-pass filter with cut-off at the spatial frequency [31]

$$f_0 = \frac{\mathrm{NA}}{\lambda}. \tag{2.90}$$

In incoherent imaging, the transfer function is the Fourier transform of $|h(u,v)|^2$, and is known as the *optical transfer function* It constitutes a less sharp filter of about the same cut-off frequency. In any case, the frequency response in imaging is an analog low-pass filtering of spatial frequencies.

[8] Presented in Appendix A.

Axial resolution

Axial resolution refers to how details in the object appear in the image when perfect focus is not obeyed. On the object side, this affects how well three-dimensional objects are imaged. The axial range in object space over which appreciable sharpness is met in the image is known as the *depth of field*. Pluta [37] shows that the diffraction limit of the depth of field can be given by

$$2\delta z = \frac{n\lambda}{\mathrm{NA}^2}, \tag{2.91}$$

where n and NA are the refractive index and numerical aperture in object space. The factor 2 shows that this is the two-sided depth.

2.4.5 Sub-surface imaging

Imaging of features internal in a medium is termed sub-surface microscopy. Object space is thus located in a material, which introduces some challenges that are not subject for in-air object-spaces. When imaging reflections within the material, the extinction coefficient $\kappa(\lambda_0)$ sets requirements to the wavelengths that can be propagated through the medium without absorbing the light. In addition, the refractive index n of the medium limits the cone of rays that can be transmitted in and out of the material through . Above the critical angle $\theta_c = \sin^{-1}(n_{air}/n)$ of total internal reflection, no transmission occur at all. Below this limit light is refracted according to Snell's law. The left part of Figure 2.16 shows how reflected light is refracted when using a slab with a planar medium-air interface as the object space. An imaging system accepts a cone of rays given by the half-angle θ. In this case, the amount of light accepted is reduced due to refraction at the interface, causing a reduction of brightness in the image. Snell's law however states that NA is equal on both sides of the interface, hence the diffraction-limit of lateral resolution is not affected by refraction compared to an in-air object space.

Solid immersion

Sub-surface imaging can be greatly improved by applying immersion techniques. To the right of Figure 2.16, the object medium is shaped as a *solid immersion lens* (SIL). This is a technique first used by Mansfield and Kino [38]. The medium is formed as a plano-convex lens, where the spherical center is situated in the center of the planar surface. Wavefronts converging towards or diverging from the spherical center are not refracted at the spherical interface because they strike at normal incidence. Waves reflected from within an appreciably small area surrounding the focal point are only slightly refracted at the interface. Spherical aberrations are therefore kept at a minimum. Moreover, the

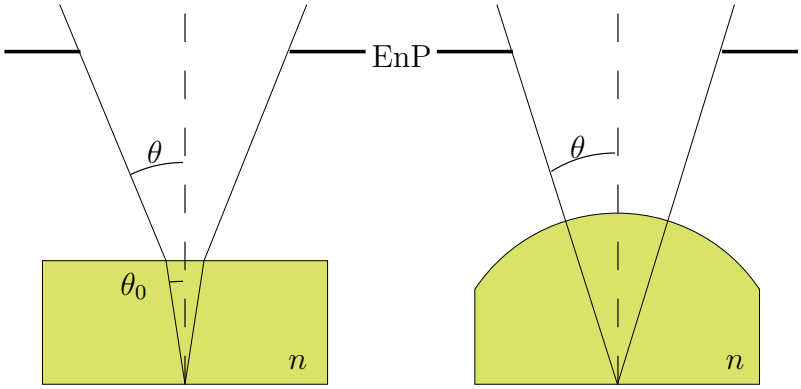

Figure 2.16: The cone of rays accepted by the entrance pupil of an imaging system for sub-surface imaging through a slab (left) and a SIL lens (right). No refraction occurs on transmission through the spherical surface of the SIL lens, hence the object space NA is increased by the refractive index n.

half-angle depicting the cone of rays accepted by the imaging system is the same as for an object space in air. The NA is therefore a factor n larger than that of an equivalent in-air object space:

$$\mathrm{NA} = n \sin\theta = n\mathrm{NA}_{air} \tag{2.92}$$

It follows from eq. (2.88) that the diffraction-limit of lateral resolution,

$$\delta x = \frac{0.61\lambda}{n\mathrm{NA}_{air}} \tag{2.93}$$

is also improved by a factor n.

When imaging reflections from the plane surface, this constitutes the object that is imaged. The spherical surface forms a virtual image of the object in the exact same object plane. This is seen by setting $z_o = R$ and $n_2 = 1$ in eq. (2.59). Hence, according to eq. (2.60), the solid immersion technique scales the magnification of an imaging system by a factor equal to the refractive index.

2.5 Interference microscopy

The application of optical interference in conventional microscopy is known as interference microscopy. It offers a non-contact technique for determining both lateral and axial structures of an object sample. The technique combines theory related to optical interference, coherence and imaging. A sample is imaged by ordinary microscopy, revealing lateral

structures of the object in focus. The addition of a reference field introduces interference fringes in the image that are related to the sample height $h(x, y)$ relative to the reference [39]. In this section, the Linnik interference microscope is first presented, followed by a description of its application in obtaining interferometric phase maps and depth profiles of the sample surface.

2.5.1 The Linnik Interference Microscope

The Linnik configuration shown in Figure 2.17 is a two-beam interference microscope based on the Michelson interferometer presented in Section 2.2. Microscope objectives in both arms of the interferometer image reflections of the sample and reference surfaces to a common image plane, with the aid of a tube lens in the detector arm. The individual image amplitudes are hence superimposed in the image. Interference fringes are present in the image provided that optical path differences are within the coherence length of the light source. The configuration can be used in imaging mode only by blocking the path of light in the reference arm.

Fringe spacing

The intensity distribution at image coordinates (u, v),

$$I(u, v, \Phi) = I_r(u, v) + I_o(u, v) + 2I_r(u, v)I_o(u, v)\Re\left[\gamma_{ro}(\Phi(u, v))\right], \tag{2.94}$$

is given by the superposition of the two image amplitudes. The spatial variation of the phase difference $\Phi(u, v)$ is the origin of the fringe pattern in the image. These are fringes of equal thickness. The fringe spacing is related to the sample height relative to the reference surface by the formula [41]

$$h(x, y) = f\frac{\bar{\lambda}(n)}{2}\frac{\Phi(u, v)}{2\pi}, \tag{2.95}$$

where (x, y) is the corresponding object coordinates and n is the refractive index of object space. f is here a scaling constant known as the NA-factor. It arises due to the large cone of rays accepted by the microscope objectives. With a large NA, the imaging system accepts rays with large incidence angles on the reflecting surfaces, thereby increasing the fringe spacing in the image. In effect, the NA-factor is always larger than unity. The limit $f = 1$ reproduces the result for a Michelson interferometer where only plane wavefronts are accepted (NA = 0). When relating fringe spacing to sample heights, the NA-factor must be calibrated beforehand [42]. A number of theories have been developed in order to explain the NA-factor. The most accurate with experimental results is given by Ingelstam and Johansson [43].

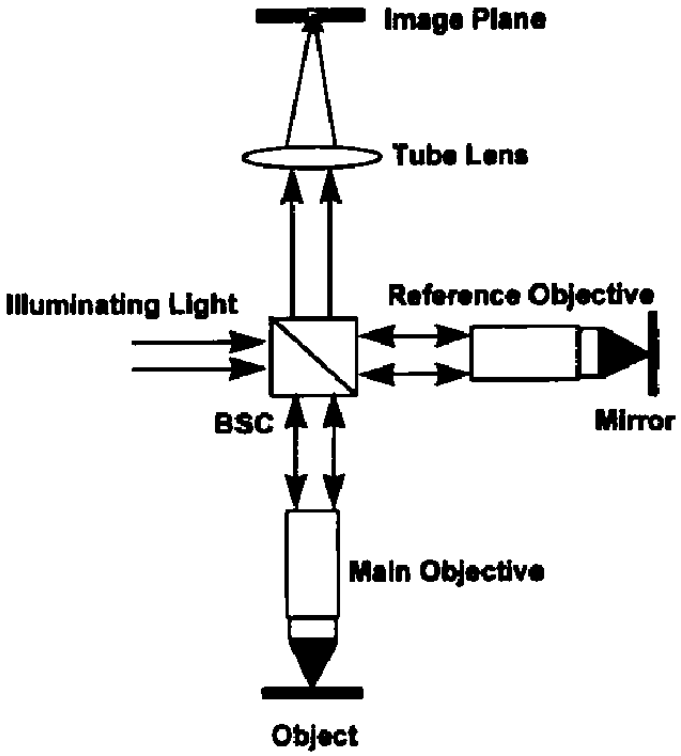

Figure 2.17: The Linnik interference microscope. Identical objectives image reflections in both arms of the interferometer to a camera array in the image plane. The recorded intensity inherits temporal interference effects in the same way as the Michelson interferometer, but with effects of imaging. BSC denotes a beam splitter cube [Reprinted from Abdulhalim [40]].

Interferograms

As the reference mirror is scanned axially, interferograms are recorded for each of the pixels in the camera array. These interferogram are sinusoidal with the phase difference $\Phi(u, v)$. The displacement corresponding to one period in the interferogram is $f\lambda_0/2$ as calculated from eq. (2.95) with $\Phi = 2\pi$ and $n = 1$[9].

The wave theory for double beam interference microscopes has been studied by Abdulhalim [40]. His derivations are based on the superposition of image amplitudes from point sources in both of the object planes, given by the point spread function of eq. (2.80). An expression for the interferogram of each pixel is ultimately derived. The derivations are very comprehensive, including effects of temporal coherence between the two fields, spatial coherence of the respective object distributions and imaging. The resulting expression is hard to interpret analytically, and require simulations to be understood. For these reasons, only a qualitative description of the theoretical results are given here. The reader is referred

[9]The change in Φ is in the interferogram related to the wavelength in air

to the reference for further details. In addition to the envelope resulting from temporal coherence described in Section 2.3.4, interferograms are modulated by two other envelopes that are due to imaging. One is caused by the axial resolution of the imaging system. As the reference mirror is scanned, it necessarily appears out of focus. This causes a difference in defocus between the interfering waves and hence attenuation of the interference signal. The width of this envelope is according to (2.91) inversely related to the NA. The other envelope is due to a lateral shift of oblique ray's as the reference mirror is scanned, but is not considered further in this text. The interference signal can therefore be modeled

$$I(z) = I_0[1 + f_{im}(z)|\gamma(z)| \cos(4\pi z/\bar{\lambda}_0)], \tag{2.96}$$

as a function of the scanning displacement z. $f_{im}(z)$ is the envelope caused by imaging defocus. The width of the overall envelope is generally determined by the smaller of the coherence length l_c and the depth of field δz.

2.5.2 Phase maps

The intensity images obtained with an interference microscope exhibit interference fringes that are contour lines of constant height. A topographic phase map of the object is thus obtained [44]. Contour lines are ambiguously determined modulo a phase of 2π. Equivalent to the description of interferograms above, the fringe contrast is axially modulated by an envelope of length given by the coherence length l_c. Therefore, fringes are restricted to a section of given depth in the sample. This depth is set by the axial position of the reference mirror. Figure 2.18 shows the sectioning of interference fringes at three different reference mirror positions when inspecting a sawed c-Si channel.

Figure 2.18: Topographic phase maps of a c-Si sawing channel for three scan positions. **Left:** Low frequent fringes are apparent in the lower left corner, corresponding to a flat surface. **Middle:** Fringes are present on the channel edges (1 and 2) only. **Right:** Fringes are present near the bottom of the channel. [Reprinted from Gastinger et al. [19]].

Phase-shifting interferometry

The contrast of interference fringes in phase maps can be enhanced by applying algorithms of phase-shifting interferometry (PSI), thus allowing for easier interpretation. The algorithm here presented is a five-frame technique presented by Hariharan et al. [45]. A short interferogram of five frames is recorded for all image pixels by scanning of the reference mirror. The frames should be uniformly distributed in the interferogram and cover one period of the signal. Hence the phase difference between subsequent frames is $\alpha = \pi/2$.

The recorded intensities are thus given by

$$\begin{array}{rl} I_1(u,v) = & I_0(u,v)[1 + |\gamma| \cos{(\Phi(u,v) - 2\alpha)}] \\ I_2(u,v) = & I_0(u,v)[1 + |\gamma| \cos{(\Phi(u,v) - \alpha)}] \\ I_3(u,v) = & I_0(u,v)[1 + |\gamma| \cos{(\Phi(u,v))}] \\ I_4(u,v) = & I_0(u,v)[1 + |\gamma| \cos{(\Phi(u,v) + \alpha)}] \\ I_5(u,v) = & I_0(u,v)[1 + |\gamma| \cos{(\Phi(u,v) + 2\alpha)}] \\ , & \end{array} \tag{2.97}$$

where $\Phi(u,v)$ is the modulo 2π phase of the third frame at image coordinates (u,v). The temporal coherence envelope $|\gamma|$ is considered constant in the small region of interest. For each pixel, the intensities in (2.97) can be combined to yield

$$\frac{I_2 - I_4}{2I_3 - I_1 - I_5} = \frac{\sin\alpha \sin\Phi}{(1 - \cos 2\alpha)\cos\Phi}. \tag{2.98}$$

With the relative phase shift $\alpha = \pi/2$, (2.98) Φ is calculated as

$$\Phi = \arctan\left[\frac{2(I_2 - I_4)}{2I_3 - I_1 - I_5}\right]. \tag{2.99}$$

When the algorithm is applied to all pixels, $\Phi(u,v)$ is a high-contrast modulo 2π topographic phase map.

The five-frame technique is quite insensitive to systematic errors in the interferometric process such as deviations from the condition $\alpha = \pi/2$, as illustrated by Hariharan et al. [45] in Figure 2.19. A drawback is that phases are calculated for all pixels, also those where fringes are not present. This may result in a chaotic pattern of ambiguously calculated phases.

2.5.3 Surface profilometry

When using a light source of low coherence, the interference microscope has application to profiling of sample surfaces. This non-contact profiling method is known as white-light

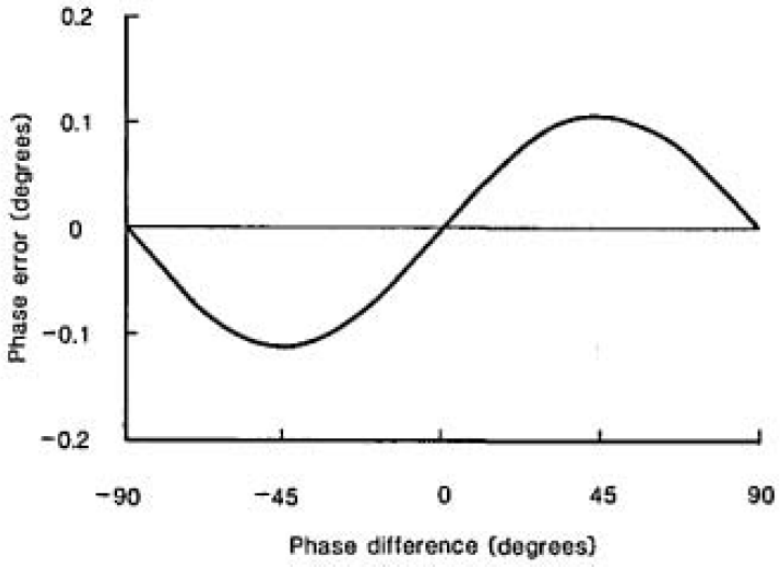

Figure 2.19: The error in calculated phase using the five-frame technique as a function of phase difference Φ. In this case, the phase shift is $\alpha = 95°$ instead of $\alpha = 90°$ (degrees). [Reprinted from Hariharan et al. [45]].

interferometry (WLI) and is based on the analysis of interferograms. The sample surface depth is estimated for all pixels in the image, and since used to replicate the surface profile. The precision of depths can be further enhanced by applying PSI algorithms.

Peak detection

Sampling interferograms for all pixels in the image leads to a three-dimensional interferogram. Each of the individual interferograms consists of a sinusoidal signal modulated by an envelope that is due to the limited by temporal coherence of the source or the limited axial focus, as shown in Figure 2.20. The envelope has a well-defined peak which corresponds to full temporal coherence between the object and reference light. Hence the peak occurs where the optical path difference is canceled out, i.e. where light is reflected from the same axial height on both the reference and sample mirrors. Determining the position of the peak on the x-axis of the interferogram gives an estimate of the sample height for that specific pixel [46].

A number of methods for determination of this position exists. Two of these, the Hilbert transform and the "Discrete Fourier Transform method" are presented in appendices A and B respectively. The former extracts the envelope from the signal and seeks to determine the position of its maximum. The latter rectifies the signal before the position is calculated from an analytic expression using the Discrete Fourier Transform.

The estimate of depth is found as a number z in units of frame numbers in the interferogram.

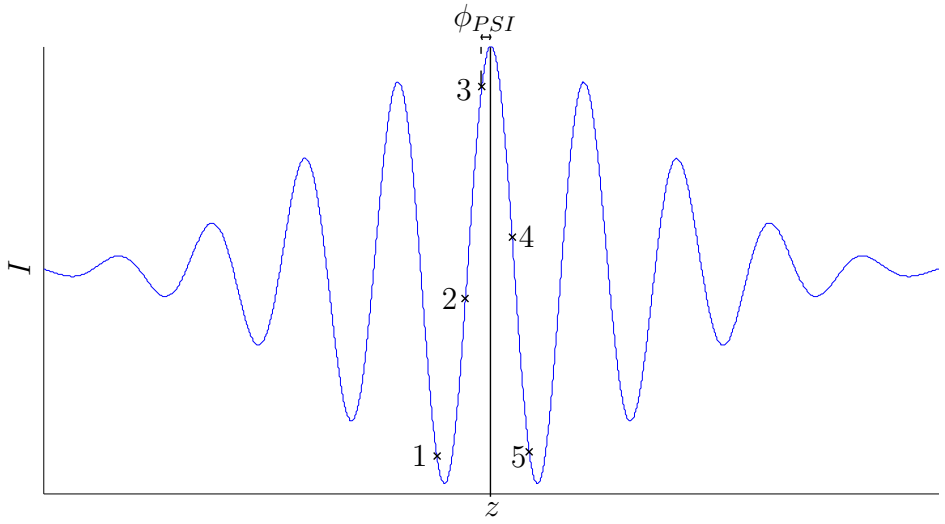

Figure 2.20: The depth of a given pixel is WLI-estimated by computing the x-axis position of the envelope peak in the corresponding interferogram. Accuracy can be later be improved by applying the five-frame PSI algorithm to compute the phase Φ of the frame (3) nearest to the WLI estimate. The true depth is represented as the x-intersection of the black vertical line.

If the phase difference $\Delta\Phi$ between frames in the interferogram is known, z can easily be related to an unambiguous phase $\Phi_{WLI}(z)$ in the interferogram through the formula

$$\Phi_{WLI}(z) = z\Delta\Phi. \tag{2.100}$$

This phase is relative to the first interferogram frame. The sample depth is then calculated from eq. (2.95). If $\Delta\Phi$ is not known, or if it is non-uniformly distributed in the interferogram, it can be calculated from a PSI algorithm. The difference in phase between two subsequent frames in the interferogram, $\Delta\Phi_n = \Phi_n - \Phi_{n-1}$, can be calculated from the formula [46]

$$\Delta\Phi_n = \arctan\frac{N_n D_{n-1} - D_n N_{n-1}}{N_n N_{n-1} + D_n D_{n-1}}, \tag{2.101}$$

where N and D are given by

$$\begin{aligned} N &= 2(I_4 - I_2) \\ D &= I_1 - 2I_3 + I_5, \end{aligned} \tag{2.102}$$

with intensities given from eqs. (2.97). When applied to all sampling intervals in the interferogram, the result is a history of phase steps [47]. The phase of the peak position is

roughly determined as

$$\Phi_{WLI}(z) = \sum_{n=4}^{z} \Delta\Phi_n. \tag{2.103}$$

This method can be used also to calibrate the sampling steps of the interferogram.

WLPSI

The accuracy in the depth determination can be further enhanced by applying PSI algorithms, given that the WLI estimate is accurate enough. The combination of these two methods is referred to as WLPSI. If the peak position is already determined within the zeroth order fringe, the phase ϕ_{PSI} of the nearest sampling point relative to the actual peak can be determined from eq. (2.99), as is shown in Figure 2.20. The final depth can thus be determined from the formula

$$h = \frac{f\tilde{\lambda}}{4\pi}(\Phi_{WLI}(z) - \phi_{PSI}). \tag{2.104}$$

If the depth is not accurately determined within the zeroth order fringe, a 2π ambiguity is introduced in the overall phase. Hence the WLI estimate must be accurate within a range of phase $[-\pi, \pi]$ for PSI corrections to be applied unambiguously.

2.6 Material Removal in Fixed-Abrasive Sawing

A theoretical study on the material removal mechanism in fixed-abrasive multi-wire sawing of monocrystalline silicon has been given by Gao et al. [48, 17]. A brief qualitatively description of the theoretical understanding is given in this section. The physical model of the process considers abrasive diamonds to be connected to the traveling wire by elastic springs. Elastic deformation of the wire is represented by deformation of the springs. As the wire travels parallel to the silicon surface, the abrasives grind the material. The material removal is mainly due to brittle fracture by grits near the bottom of the wire. The formation of the wafer surface is however due to ductile fracture from grits located at the lateral sides of the wire.

The material removal is explained from indentation fracture mechanics and is similar to that of free-abrasive sawing. A single diamond grit is considered to perform a moving indentation on the silicon surface, exerting both normal and tangential force. Figure 2.22 shows an illustration of the fracture mechanics. At atmospheric pressure, the silicon crystal is ordered in a diamond lattice. However, when subject to the stress applied by

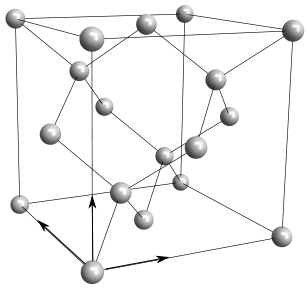

Figure 2.21: Silicon crystallized in a three-dimensional diamond lattice. The black spheres are the location of silicon atoms. Arrows represent the [100] directions in the lattice.

a sharp indenter, plastic deformations occur. These can transform the material under the indenter into denser crystal phases [49] with, possibly, different optical properties. At even larger stress, cracks are initiated in both the median and lateral directions from a depth of approximately the deformation zone. These are due to inter-atomic bonds breaking. Lateral cracks may propagate outwards and intervene with one another. When these emerge to the surface, pieces of silicon are chipped away from the surface, leaving an empty volume on the surface. As a single grit moves with the wire, the surface is formed by connection of such volumes [17].

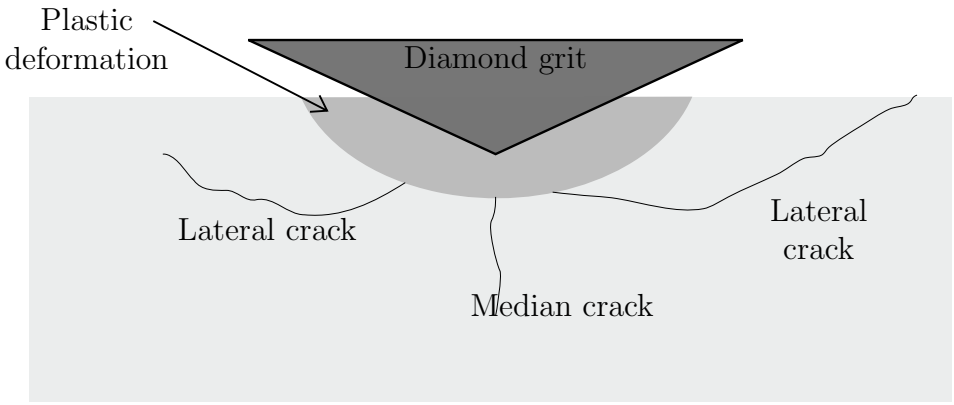

Figure 2.22: Illustration of the theoretical material removal mechanism in fixed-abrasive sawing. Material is removed when lateral cracks extend to the c-Si surface.

Chapter 3

Experimental Setup and Procedures

This section describes the experimental apparatus that has been built and used in this work, as well as the various procedures that have been followed. The optical system is based on a Linnik-configured interference microscope. For indentations and characterization of interference fringes, additional equipment has been built. Experiments are run from a computer with the assistance of a simple electric system.

3.1 Optical System

The optical apparatus is illustrated in Figure 3.1. Central components are mounted in a 30mm cage system on a vibration isolated table. A photograph of the setup is shown in Figure 3.2. This section gives a brief description of the key optical components, followed by a detailed analysis of the optical design. The latter is presented in two parts: illumination and imaging.

3.1.1 Optical components

Light source

The light source is a superluminescent diode (SLD) that combines the broadband characteristics of a conventional LED with the high power of a laser diode [50]. For transparency in silicon, a near-infrared (NIR) source with a central wavelength $\bar{\lambda} = 1290$nm is used. The spectral distribution is shown alongside the coherence function in Figure 3.3. It is recalled from Figure 2.1 that the extinction coefficient is very close to zero in this wavelength range. The width of the spectrum $\Delta\lambda \simeq 40$nm is sufficiently small for the light to be considered quasi-monochromatic, according to the condition in (2.50). The temporal

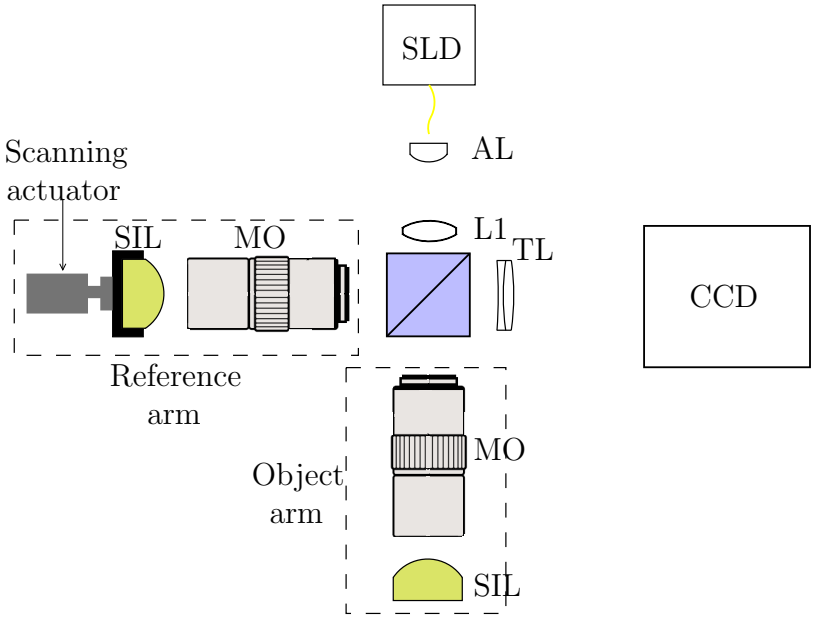

Figure 3.1: An illustration of the optical system. The beam splitter, shown in blue, is at the core of the setup. Optical components are abbreviated according to Table 3.1.

coherence length, given as FWHM[1], is roughly $l_c = 25\mu$m. Light is passed from the SLD to the interferometer in a single-mode optical fiber. Further specifications are provided in Appendix F.

Beam splitter

A cubic non-polarizing beam splitter is mounted in the core of the interferometer with a 50:50 splitting ratio. Equal amplitudes of light are thus transmitted to the two arms of the interferometer. The cube is made up of glass with refractive index $n \simeq 1.5$. Each face of the cube has an anti-reflection coating that reduces unwanted reflections to less than 0.2% over the wavelength range of the SLD.

Microscope objective

Identical microscope objectives are mounted in both the reference and object arm of the interferometer. The specific objective is infinity corrected, meaning that it is designed to image objects with the aid of a tube lens. It is designed for 20x lateral magnification and has focal length $f_{obj} = 10$mm, hence a tube length of focal length $f_{TL} = 200$mm must be used. Principal planes are located as depicted in Figure 3.4. The objective has a numerical aperture $NA = 0.4$, which allows a cone of light with half-angle 23.57° to be

[1]Full Width at Half Maximum

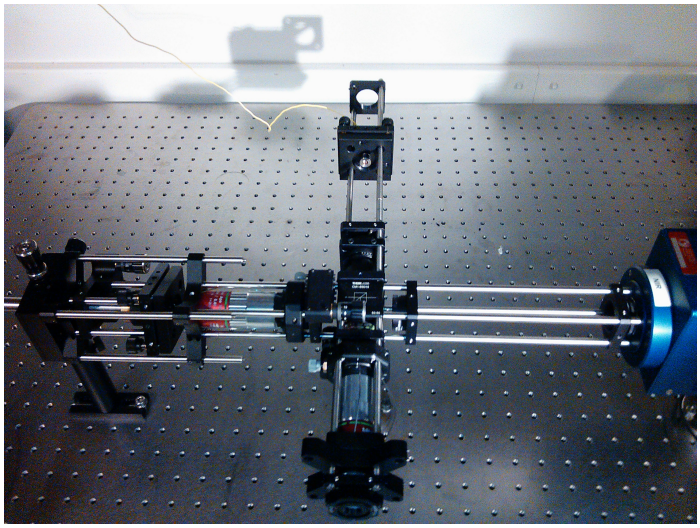

Figure 3.2: Photograph of the optical system. Reference and object arms are seen to the left and in the bottom, respectively. The camera is to the right.

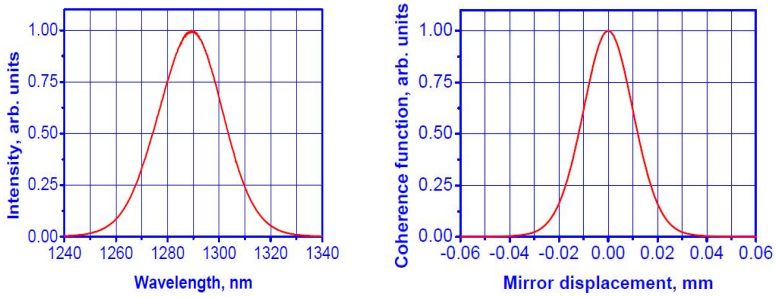

Figure 3.3: **Left:** The spectral distribution of the SLD, represented by the normalized intensity spectrum. Light is restricted to the region from 1250nm to about 1330nm. **Right:** Normalized coherence function as a function of mirror displacement. [Reprinted from [50].]

transmitted. The exit pupil of the objective is located in its back focal plane with diameter 8mm. Chromatic aberrations are compensated for in the NIR range (480-1800nm), thus covering the wavelength spectrum of the SLD. Further specifications are listed in Appendix F. Both objectives are mounted to the cage system with manual translation stages in all Cartesian directions, allowing lateral alignment (x and y) and focusing (z).

Solid immersion lens

The reflecting surfaces of both interferometer arms are constituted by SIL lenses made from monocrystalline silicon, with spherical radius $R = 8$mm as shown in Figure 3.5. Light transmitted through the spherical surface illuminates the back side surface of the

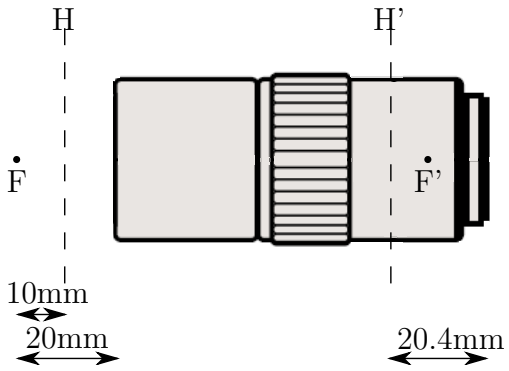

Figure 3.4: Principal planes and focal points of the microscope objective mounted in both the object and reference arm. [Reprinted from Appendix F]

lens. Light reflected from this surface constitute the object that is imaged. The spherical surface assures high lateral resolution and magnification in imaging, as discussed for solid immersion in Section 2.4.5. The same surface is anti-reflection treated in the wavelength region 1100-1600nm in order to avoid multiple internal reflections and increase the amount of light illuminating the back surface.

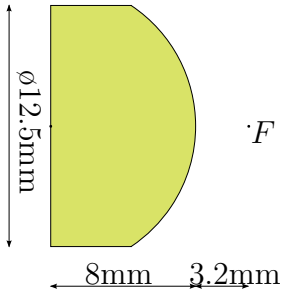

Figure 3.5: Profile and dimensions of the c-Si SIL lens used as object and reference mirrors. Reflections occur at the flat back side, where the center coincides with the spherical center. F denotes the focal point of the lens. Indents are introduced from outside the back surface on the object lens.

Refraction at the spherical surface is governed by eq. (2.59). In addition to the spherical center, a focal point[2] exists on the outisde of the SIL lens. This point is located at a distance

$$f = \frac{nR}{n-1} = \frac{3.506 \cdot 8\text{mm}}{3.506 - 1} \simeq 3.2\text{mm} \tag{3.1}$$

from the tip of the lens.

[2]In the sense of imaging light to infinity.

At normal incidence, the reflection coefficients of both polarizations are approximately 0.55. However, the large NA of the objective allow rays of angles up to 23.57° to be imaged. This corresponds to incidence angles on reflection that are larger than the critical angle of total internal reflection $\theta_c = \sin^{-1}(1/3.5) = 16.6°$. It must therefore be expected that phase-changes on reflection occur for some of the reflected light. This could possibly affect the interference of object and reference light.

The reference arm SIL lens is mounted to the tip of a piezoelectric actuator [3] which again is attached to the cage system. This enables the motorized translation stage necessary for axial scanning.

The object arm SIL lens is held in a separate cage that is magnetically mounted to the cage system. It can be rotated around the optical axis in steps of 120°. Equipment has been built that also allow it to be vertically tilted about its spherical center[3]. For indentations, the back side of this SIL lens is exposed to the indenter.

3.1.2 Optical design

The optical design of the reference and object arms of the interferometer are identical[4]. Therefore, the passage of light is described here with regards to a single arm only. The "object" will refer to the reflecting surface in either of the arms. Table 3.1 summarizes the focal lengths of the various refracting components used, with the abbreviations at which they are presented in figures.

Abbreviation	Type	Focal length [mm]
AL	Aspheric lens	4.6
L1	Bi-convex lens	25.4
MO	Microscope objective	10
TL	Tube lens	200
SIL	Solid immersion lens	3.2

Table 3.1: Summary of the various refracting components used in the optical setup and their respective focal lengths.

Illumination

Figure 3.6 illustrates how the object plane is illuminated by the light source. The output of the fiber is imaged to the object plane with a slight defocus. Ideally, the image should be perfectly defocused, by applying Köhler illumination[5]. This would be achieved by imaging

[3]Described in Section 3.2.3.

[4]The reflecting surface of the reference arm will however appear out of focus when scanned.

[5]First used by August Köhler [51].

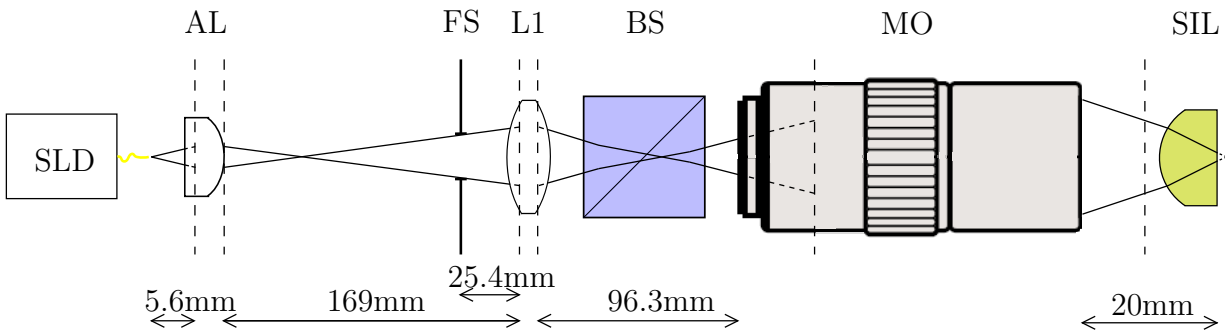

Figure 3.6: The optical design for illumination of the object. Illuminating rays are shown from an optical axis point at the output of the fiber to the object plane. Virtual rays are stapled. Vertical stapled lines are principal planes. It is stressed that this illustration is not drawn proportionally.

the fiber output to the first focal point of the SIL lens. However, as is discussed in Chapter 4, this is hard to obtain in practice due to the imaging design. The setup shown here is that corresponding to the most even illumination that was obtained. Rays have been traced by successive application of the thin lens formula (2.61). It is noted that the system is more similar to critical illumination, where a perfectly *focused* image is formed in the object plane [52].

An aspheric collimator lens (AL) projects an intermediate image of the fiber output to the front of a biconvex lens (L1). The latter lens forms another intermediate image which is located within the beam splitter (BS). Refraction at the flat faces of the BS forms a virtual image for the objective. Finally, a defocused image is formed at the back surface of the SIL lens. This image is focused at a distance 0.3675mm behind the SIL lens back surface.

An adjustable aperture is introduced in the front focal plane of L1, enabling control of the field of view. This constitutes the field stop FS of the system. The FS and final image are located in conjugate planes, hence the entrance window is located in the object plane and appear with sharp edges in the observed image.

Imaging

Figure 3.7 illustrates how reflections from the object are imaged to the image plane. The object plane O coincides with the flat surface of the SIL lens. According to eqs. (2.59) and (2.60), the spherical surface of the SIL lens forms a virtual image in this same object plane, with magnification equal to $n = 3.506$. This image serves as a virtual object for the objective, and is located in its front focal plane. The objective thus forms an image located at infinity, which is projected to a real image in the image plane I by the tube lens. A camera array is placed in this plane, which is located 200mm from the tube lens. The objective and tube lens magnifies the virtual object by a factor

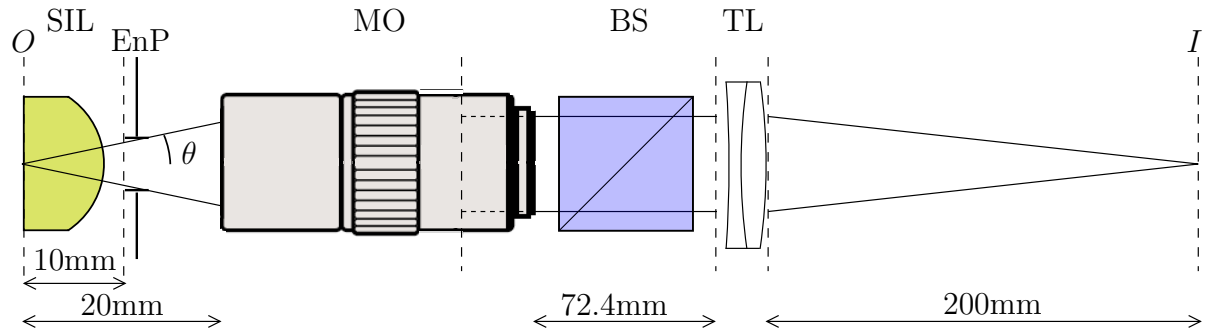

Figure 3.7: Imaging rays from an axial point in the object plane O to the image plane I. Stapled vertical lines are principal planes of the objective and the tube lens. The beam splitter alters the optical path length between objective and tube lens, but does not affect the geometrical image since the objective images at infinity. The illustration is not drawn to proportion.

$$M_{MO,TL} = \frac{f_{TL}}{f_{MO}} = \frac{200\text{mm}}{10\text{mm}} = 20. \tag{3.2}$$

Combined with the magnification of the virtual object, the total magnification should theoretically be

$$M_{tot} = 3.506 \cdot 20 = 70.12. \tag{3.3}$$

Due to the objective imaging at infinity, focus is not affected by the objective-to-tube lens distance.

As is previously described, the entrance window of the system coincides with the object plane. The aperture stop of the system is determined by the exit pupil of the microscope objective. Its object side image is located in the focal plane of the SIL lens, and serves as the entrance pupil of the system. Lateral and axial resolution are determined by the numerical aperture, given by the half-angle accepted by the objective and the object space refractive index. According to (2.88), the diffraction limit for the lateral resolution is

$$\delta x = \frac{0.61 \cdot 1.29\mu\text{m}}{3.506 \cdot 0.4} \simeq 0.56\mu m. \tag{3.4}$$

Accordingly, by (2.91) the limit for depth of field is

$$2\delta z = \frac{3.506 \cdot 1.29\mu\text{m}}{0.4^2} \simeq 28.27\mu m. \tag{3.5}$$

The frequency response of the image is determined by a low pass filter with a cut-off frequency calculated from eq. (2.90) as

$$f_0 = \frac{3.506 \cdot 0.4}{1.29\mu\text{m}} = 1.09\mu\text{m}^{-1} \tag{3.6}$$

3.2 Supporting System

Experiments are run from the computer by collecting still images from the CCD array. The same computer also controls scanning, indenter movement and object tilt. This section presents the additional equipment that is used in the various experiments. Two mechanical stages has been built, and can interchangeably be attached to the rear side of the interferometer object arm. These enable the object SIL lens to be indented and tilted.

3.2.1 CCD camera

The camera is a charge-coupled device (CCD)[53] with 640x512 photoconductive pixels situated in a two-dimensional array with a pixel pitch[6] of 20μm in both directions. Given this pitch and the magnification calculated in (3.3), the camera should output an image with an object-side field of view of 146x182.5μm. The spatial Nyquist period[7] (2x pixel pitch) corresponds to a length of 0.57μm in object space. The pixels record intensity in a spectral band ranging from 0.9 to 1.7μm, hence covering the entire spectral band of the light source. Analog intensities are converted to digital representation with a resolution of 12 bits and are transferred to the computer by a USB interface. The camera can be calibrated from software by adjusting parameters such as integration time, gain and reference voltage. The camera is further specified in Appendix F.

3.2.2 Software

Camera settings are adjusted in the X-Control software provided by the camera manufacturer [55]. This program gives live images, but is also used to capture still images. Routines for experimental control are written in visual LabVIEW [56] code, with additional text code written in MATLAB [57]. A separate software program, APT, is used to control the tilt of the object arm SIL lens [58]. Resulting data from experiments are analyzed with MATLAB code.

[6] "Pixel pitch is the center-to-center distance between adjacent picture elements (pixels)" [54]
[7] Discussed in Appendix C.

3.2.3 Electrical System

An electrical system supplies amplified voltage signals to three piezoelectric actuators: one responsible for scanning of the reference SIL lens and two responsible for indenter movement. A diagram of the signal flow in scanning is shown in Figure 3.8. The following is a brief description of the different electrical components is given in the following.

Figure 3.8: Schematic diagram of the signal flow in the electric circuit, from the computer to the piezoelectric actuators. The low-pass filter is only present for the scanning actuator.

Digital to analog converter

Analog voltages are constructed from digital data by a digital-to-analog (DA) converter. The converter is capable of outputting voltages in the range $[-10\text{V}, 10\text{V}]$ with a resolution of 16 bit. Digital signals are output from the computer by a USB interface.

Amplifier

Due to the short voltage range of the DA converter, signals are amplified in order to utilize the entire range of the piezoelectric actuators. An inverting[8] amplifier built by Lars Johnsen is used for this purpose. The amplifier is driven by two voltage sources of -30V and 70V and has a gain of $G = 18.7$ for voltages up to 60V. There are three amplifying channels; one for each of the actuators.

Piezoelectric actuators

Analog voltages are converted into spatial motion by piezoelectric actuators, thereby enabling the movement of both the indenter and the reference SIL lens. The actuators rely on the converse piezoelectric effect: An applied electric field induces mechanical stress that elongates the piezoelectric material within the actuators [59]. The result is an axial displacement of the actuator tip, on which the SIL lens or indenter is attached. Increasing voltages induce increasing displacement. This relation is however not strictly linear, as is shown in Chapter 4.

[8] In addition to amplify the signal, the sign of the signal is inversed. Negative signals are output from the computer in order to counter this effect.

The scanning actuator[9] has a travel length of 100μm in the voltage range 0-75V. It is hence, given the width of the coherence function in Figure 3.3, capable of scanning through the entire envelopes of features that are axially separated by $100 - 30 - 30 = 40\mu$m in object space. However, the achievable travel range is limited by the amplifier. The actuator has an internal capacitance of 18μF, and is coupled in series with a 180Ω resistor to produce a low pass filter with cut-off frequency $f_{co} = 49$Hz. This attenuates high-frequent components in the signal and minimizes noise in the electric circuit as desired for precise and uniform scanning. The capacitance introduces a time constant $\tau_{RC} = RC = 3.24$ms in the electric circuit, causing a delayed charging of the actuator [60]. This delay is accounted for by a pause in the control routine for scanning.

Two identical actuators[9] are responsible for the movement of the indenter. These actuators are referred to as the indent- (z-diection) and scratch (x-direction) actuators, and have travel lengths of 30μm in the range 0-75V. Again, the achievable travel is limited by the amplifier. The indenter actuators are coupled directly to the amplifier; no filter is constructed in these circuits. A feedback mechanism makes it possible to read the value of their displacement from strain gauge readers. In addition, micrometer screws enable a more rough travel.

3.2.4 Indenter stage

Indentations are performed with the Vickers indenter illustrated in Figure 3.9. This type of indenter is commonly used in hardness-testing of materials. It is a square based diamond with an angle of 136° between opposite faces, leaving 22° between the flat object surface and the four faces of the indenter. The diamond material ensures that the indenter is not deformed when used [61].

The indenter is mounted in a custom-built indenter stage that is attached to the interferometer cage system on the rear side of the object arm. A photograph of the stage is shown in Figure 3.10. The indent- and scratch actuators are attached to the indenter through this stage.

3.2.5 Tilting stage

Tilting of the object arm SIL lens is performed by a tilting stage that can be placed on the rear side of the arm. The stage, illustrated in Figure 3.11, rotates a wheel about an axis that is perpendicular to the optical axis of the object arm. It is positioned so that this axis intersects with the spherical center of the SIL lens. The spherical surface of the lens allows it to rotate around its spherical, within the lens holder. Mounted to the rotating wheel is

[9]Specified in Appendix F.

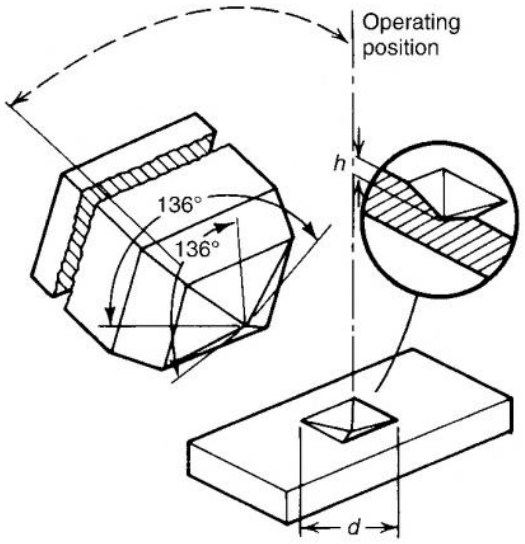

Figure 3.9: Illustration of the Vickers indenter used for moving indentations. The angle between opposite faces is 136°, and the material is diamond. The indenter enters the silicon surface normally, leaving an angle of 22° between the surface and the faces. [Reprinted from Dossett et al. [62]]

a bended arm that touches the back side of the lens. Thus, as the wheel is rotated, the lens is tilted vertically with the same angular displacement as the wheel.

The wheel is driven by a servomotor that is controlled from the computer, with a bidirectional repeatability of $\pm 0.1°$. It also provides feedback on the angular displacement. The specifications of the wheel and motor are given in Appendix F.

3.3 Procedures

This section presents the procedures that have been followed in the various experiments. Where computational routines have been written for experimental control, these are referred to in appendices. Additional code for analysis of recorded data is also referred to in appendices.

3.3.1 Alignment

Aligning the optical components is crucial in order to obtain focused images showing interference. The system is therefore flexibly designed in this aspect. The stepwise procedure of alignment has been self-developed and is presented here.

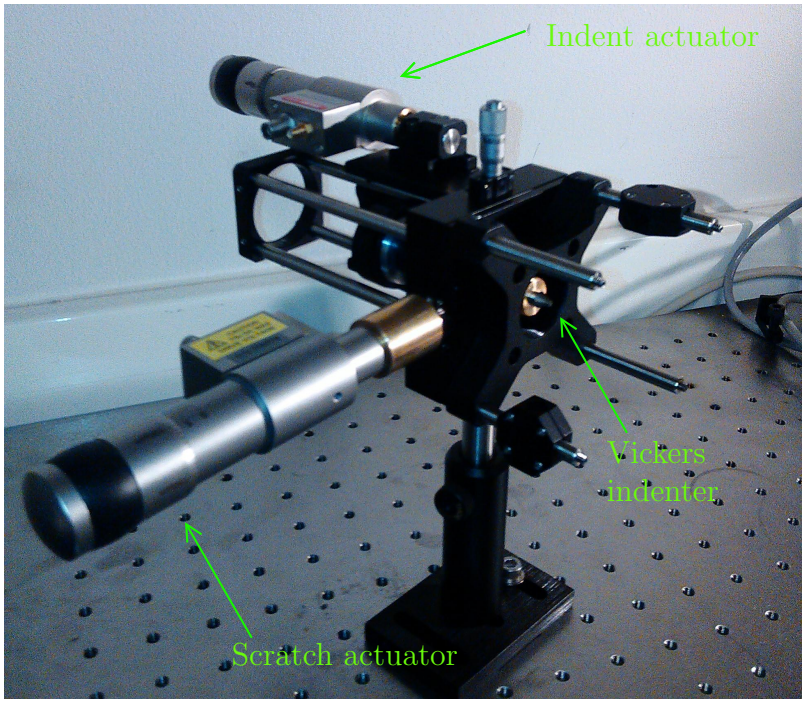

Figure 3.10: The indenter stage used to perform moving indentations on the back surface of the object arm SIL lens. The rods to the right can be attached to the rear of the object arm.

The interferometer is built with distances between components roughly according to the theoretical distances in Figures 3.6 and 3.7. These are later finely adjusted by the adjusting screws that a handful of the components are attached to the cage system with. The stepwise procedure of fine alignment is shown schematically in Figure 3.12.

It is first aimed at obtaining focused images of the objects. The object arm of the interferometer is the least flexible; the SIL lens is fixed to the cage in its magnetically mounted holder. Therefore, a centered focus is obtained in this arm first. The object surface can be brought into focus only if it inherits defected areas. If not already present on the surface, these are introduced ahead of the alignment process. Defects are brought into focus by z-translating the objective until the they appear clearly in the image. It is then assured that the object plane coincides with the first focal plane of the objective[10]. A centered image of the object is obtained by switching between the lens' three rotational positions (120° apart). The objective is laterally translated until the lateral distance from the image center to defects are equal in all three positions. It can only be assumed that the object surface is normal to the optical axis.

Moving to the reference arm, a small defect in the object surface is once again exploited

[10]Given that the distance from the tube lens to the camera array is exactly 200mm.

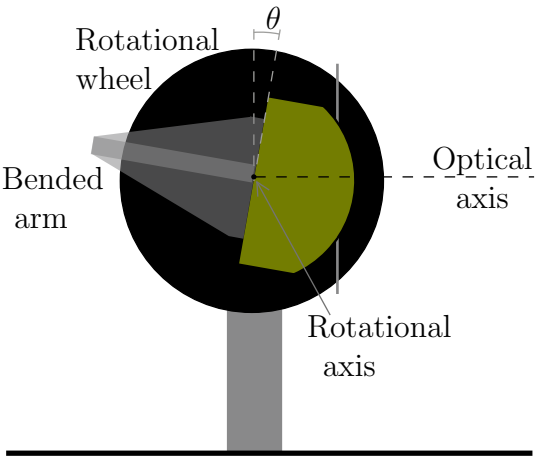

Figure 3.11: An illustration of the tilting stage used to tilt the object SIL lens.

to obtain focus[11]. The SIL lens is z-translated until the defect appears in focus.

Eliminating the path length difference between the interferometer arms is obtained by z-translating the SIL lens and objective simultaneously, keeping the defect in focus, until interference fringes appear. Fringes appear as bright and dark curved lines in the image because of misalignment.

If perfectly aligned, the fringes should appear as subsequent bright and dark frames as the reference object is axially translated. The two objects are however misaligned both laterally and angularly. In addition, the microscope objectives of both arms might be laterally misaligned. In order to counter this, the reference arm objective is now moved out of focus until the fringes converge to a common point. It is desired that this point is shifted to the center of the image, and that the fringe pattern appear circularly around this point. This step is performed rather arbitrary, by adjusting the screws altering the tilt and lateral position of the reference arm object as well as the lateral position of the reference arm objective. Once a circularly centered pattern is achieved, the objective is moved back into focus. In this last step, fringes are seen to diverge from the center and completely fill the image at focus.

For perfect alignment, this procedure must be repeated each time a new SIL lens is introduced in the object arm. However, the last step has been fully performed only when recording interferograms.

Centered illumination of the objects is assured by a set of tilting screws attached to the fiber collimator. The tilt is adjusted so that the image is symmetrically bright around its center.

[11]Since this defect is small, it is not a disturbing factor when considering limited areas in the image where it is not present.

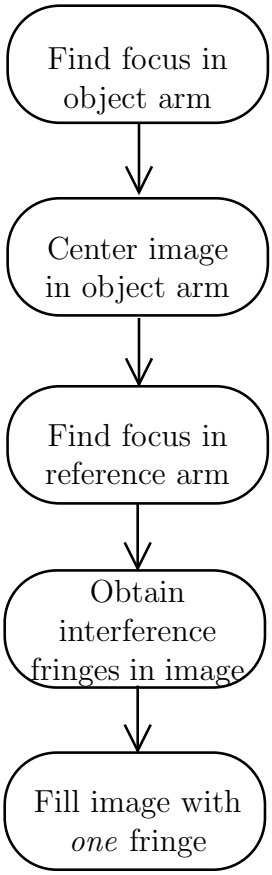

Figure 3.12: Schematic diagram of the procedure used to align the optical components for fine focus and cancellation of the path length distance between object and reference arm. The procedure has been strictly followed only ahead of interferogram scanning.

3.3.2 Imaging performance

Measurements of lateral resolution, magnification and depth of field are performed by capturing still images with the X-Control software. A SIL lens with a metallic resolution chart deposited on its object surface is used. The image is brought in and out of focus by z-translating the objective. Intensity variations along straight lines in the image are captured and manually analyzed in MATLAB.

3.3.3 Tilting

The tilting stage is utilized to observe the interference fringes' response to the object surface being tilted. A clean object surface is used for this purpose. The tilt angle is controlled by the APT software. Between subsequent tilt angles, still images are captured from X-

Control. These are later analyzed with the Discrete Fourier Transform[12] in MATLAB, where the spatial period of fringes is calculated.

3.3.4 Interferogram scanning

The systems capability of recording three-dimensional profiles of reflecting surfaces is tested by scanning of the reference arm SIL lens. The resolution chart deposited SIL lens is used in the object arm, and the alignment procedure in Figure 3.12 is fully performed. Ahead of scanning, the reference lens is manually shifted along the optical axis to assure that the entire envelope function is captured in interferograms.

The control routine used in the scanning operation is shown schematically in Figure 3.13. The corresponding LabVIEW routines are presented in Appendix D. An interferogram is obtained for each of the pixels in the image, thereby constituting a 3D-interferogram. This is saved to a three-dimensional array variable. Frames are found in the first two dimensions and the last dimension denotes the corresponding frame number. After a frame is captured, the voltage supplied to the scanning actuator is increased before capturing a new image. This process is repeated until the full range of the amplifier is reached.

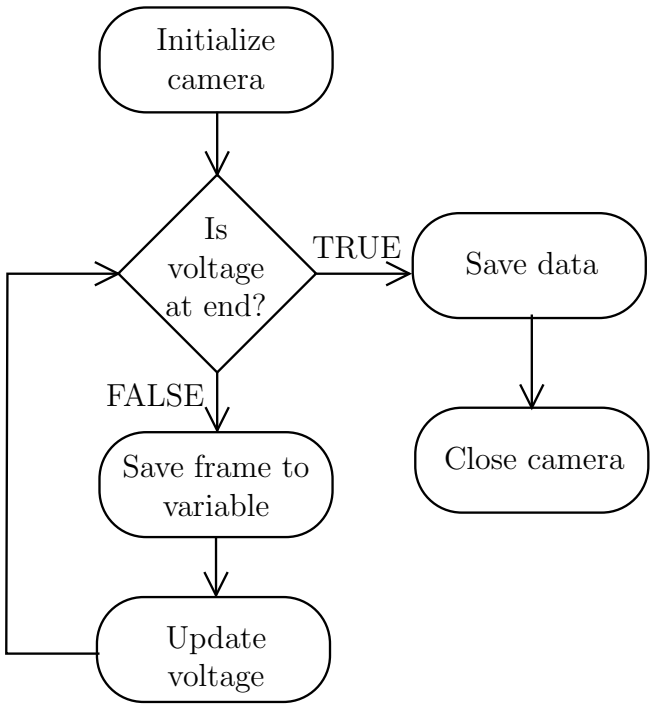

Figure 3.13: Schematic diagram of the control routine used to acquire 3D-interferograms by scanning of the reference arm SIL lens.

[12]Presented in Appendix A.

Calibration

It is desired that interferograms are sampled with uniform increments of phase. However, due to the nonlinear voltage-displacement relation of the scanning actuator, uniform displacement steps are not followed from uniform voltage steps. In order to counter this effect, the relation is calibrated. The calibration process analyzes interferograms obtained with a tilted object mirror. The tilt ensures that interference is observed in the image throughout the scanning process. Assuming a linear voltage-displacement relation, phase shifts between subsequent frames of value $\Delta\Phi = \pi/2$ should be obtained by applying uniform voltage steps of size

$$(\Delta V)_c = \frac{1.29\mu\text{m}/2}{4} \cdot \frac{75\text{V}}{100\mu\text{m}} = 0.121\text{V}. \tag{3.7}$$

The *actual* phase shifts are calculated from eq. (2.101). The result is a history of phase shifts as a function of applied voltage [47]. This data is fitted to a polynomial function $\Delta\Phi(V)$ and used as a calibrating function in later experiments. Phase shifts close to $\pi/2$ are then achieved by applying voltage steps of size

$$\Delta V(V) = (\Delta V)_c \frac{\pi/2}{\Delta\Phi(V)} \tag{3.8}$$

in the scanning operation. $(\Delta V)_c$ is here the voltage steps used in the calibration process.

Surface depths

After the scanning operation, peak detection algorithms are applied to the interferograms recorded for all pixels. Two different methods of peak detection are used. These are the "Discrete Fourier Transform method" (DFT) and the Hilbert transform method, presented in Appendices A and B, respectively. The result is an estimate of object surface depth for each of the pixels, in units of frame number in the interferogram. The MATLAB codes written for peak detection are shown in Appendix E.

3.3.5 Moving indentations

Ahead of indentation experiments, the object arm SIL lens is temporarily removed from the interferometer. The indenter tip is then brought into focus in the image by the micrometer screws on the actuators. Dust and chipped-of silicon are removed from the tip by adhesive tape while observing the image. With the SIL lens re-mounted, the indenter is approached to the surface with rough travel until Fizeau fringes appear. The last length of travel before impact on the surface is performed with piezoelectric travel. The LabVIEW code

for controlling the indent- and scratch actuators is presented in Appendix D. The indenter is stepwise penetrated to a desired depth in the silicon before the scratching process is initiated. In the same stepwise manner, the full travel length of the scratch actuator is exploited before the indenter is retracted from the sample. Indent and scratch depths are manually read from the strain gauge readers.

3.3.6 Phase maps

High-contrast phase maps are recorded during indentation by five-frame scanning of the reference SIL lens. Phase steps of $\pi/2$ between frames are assured by first noting the voltage step required to move interference fringes by a phase 2π. A perfectly aligned reference lens is not critical in these measurements. The control routine is similar to that used for interferogram scanning. A modulo 2π phase map is calculated from the five frames using eq. (2.99).

Chapter 4

Results and Discussion - System Performance

Experimental results regarding the performance of the interference microscope described in Chapter 3 are presented and discussed. The performance of the system as a conventional imaging system is first treated, followed by results regarding the interferometric performance. The obtained results are discussed in the last section.

4.1 Imaging performance

The imaging performance was surveyed in terms of lateral resolution, magnification and the depth of field. It is important to examine these concepts because they are crucial to what is achievable when the system is applied in experiments. Measurements were performed with the reference arm of the interferometer blocked from passage of light. A resolution chart deposited on the back side of the SIL lens in the object arm was used as the object in measurements. Figure 4.1 shows the chart as imaged from the back side of the SIL lens with SEM[1] by Simonsen [2]. The spatial periods of the patterns on the chart is indicated in red. This information was used in the measurements. For optimal measuring conditions, the camera settings were adjusted to exploit the entire 12-bit representation of intensities, while still avoiding saturation of pixels.

Figure 4.2 shows an image of the resolution chart in focus. The intensity of each pixel is represented by 12 bit in grayscale. Two things are worth noting from observation of this image. First, the image is not uniformly illuminated. The image brightness is greatest near the center and gradually attenuates in the radial direction. A circular pattern of illumination is seen in the corners. Secondly, the image of the chart is distorted in the

[1]Scanning Electron Microscopy.

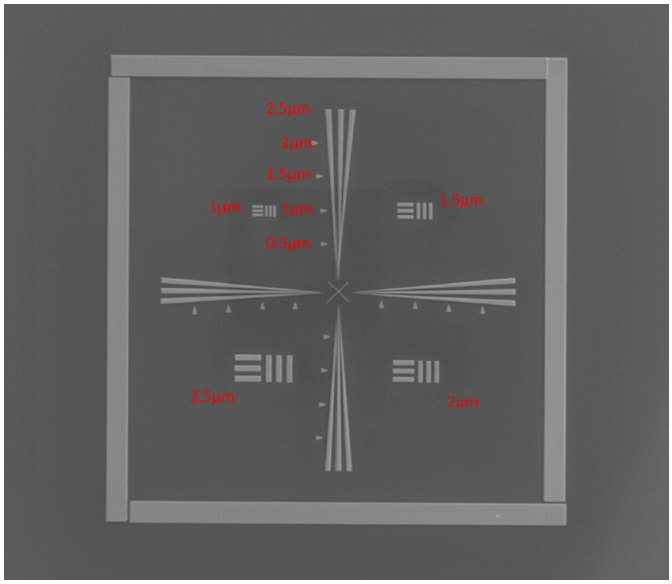

Figure 4.1: SEM image of the resolution chart used for surveying imaging properties. The lines emanating from the center are line pair gauges. The red labels indicate the spatial period of corresponding features in the object. [Reprinted from Simonsen [2].]

vicinity of the patterns. This distortion is observed as blurred replicas of the lines in the patterns.

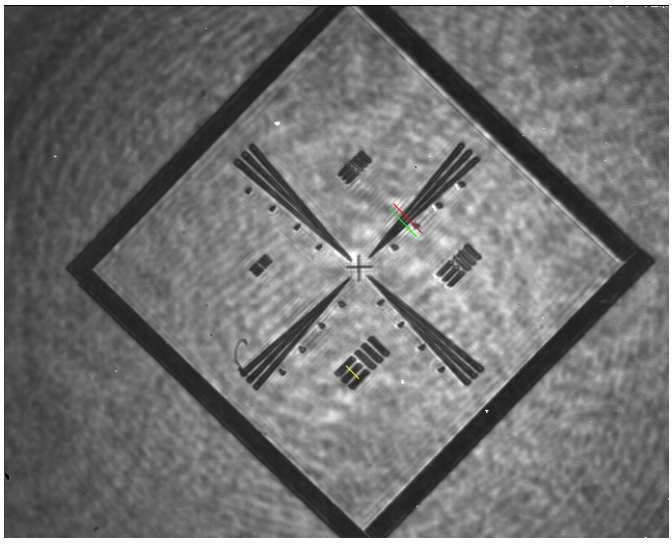

Figure 4.2: The resolution chart as imaged by the optical system through the object arm. The yellow, red and green lines traverse patterns of spatial period 2.5μm, 1μm and 0.9μm, respectively.

Lateral resolution

Experimentally, there are a number of different criterions that can be used to determine the lateral resolution of an imaging system. The one used here is described by Smith [63]: A spatial intensity signal is considered resolved if its modulation amplitude is greater than 10% of the maximum intensity in the signal.

The red line in Figure 4.2 is orthogonal to a pattern of spatial period 1μm in object space. A plot of the intensities recorded from the pixels along this line is shown in Figure 4.3. The pattern is observed between pixels 9 and 17. The modulation amplitude is measured as the intensity difference between the smallest maximum and largest minimum of the pattern, which is $\Delta I = 684$. This corresponds to $\Delta I / I_{max} = 684/3612 = 18.94\%$ of the maximal intensity in the signal. According to the given criterion, the pattern of spatial period 1μm is clearly resolved.

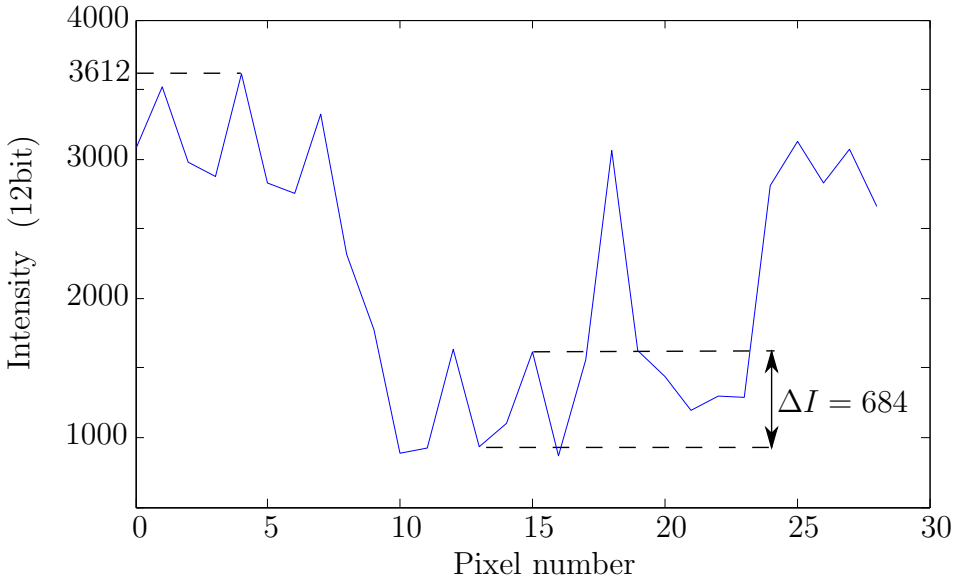

Figure 4.3: The intensity recorded from pixels on a pattern of spatial period 1μm. The pattern is clearly resolved according to the criterion. It is stressed that the pitch of these pixels does not match the pixel pitch of the camera array since the pattern is not aligned with the axes of the array.

The green line in Figure 4.2 is orthogonal to a pattern with a spatial period of roughly 0.9μm. The intensities recorded from the pixels on this line is shown in Figure 4.4. The modulation amplitude is $\Delta I = 399$, which is $399/3606 = 11.06\%$ of the maximum intensity. Hence, the 0.9μm pattern is just resolved by the imaging system. Therefore, the limit of lateral resolution can to a good approximation be determined to 0.9μm.

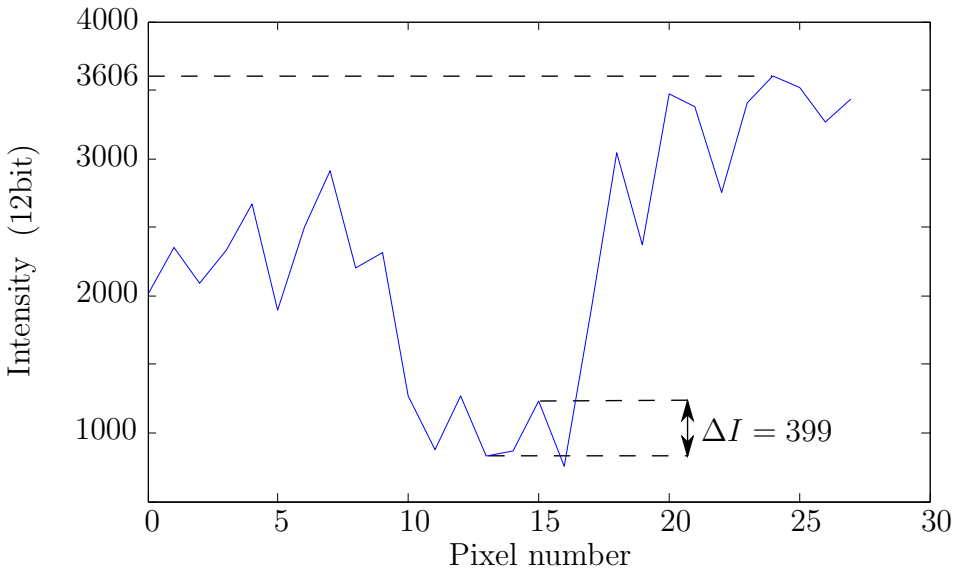

Figure 4.4: The intensity recorded from the pixels on a pattern of spatial period $0.9\mu m$. The pattern is just resolved.

Magnification

A rough measurement of the lateral magnification has been attempted. The yellow line in Figure 4.2 traverses orthogonal to two periods of a pattern with spatial period of 2.5μm in object space. The two ends of the line have pixel coordinates $(329, 348)$ and $(341, 361)$. The length of the line is therefore $L = \sqrt{(329-341)^2 + (361-348)^2} = 17.69$ pixels. The uncertainty in determining the pixel position of the two ends should be set to ± 1 pixel in both coordinate directions. Hence the uncertainty[2] of this measure is $\Delta L = 1$ pixel. Given the 20μm pixel pitch of the camera, an estimate of the lateral magnification is

$$M = \frac{(17.69 \pm 1) \cdot 20\mu\text{m}}{2 \cdot 2.5\mu\text{m}} = 70.8 \pm 4. \tag{4.1}$$

Depth of field

By moving the microscope objective along the optical axis, its front focal plane is shifted along the the same axis. This effectively causes the object to be moved in and out of focus. Since the objective is working in infinity mode, the image-side optics are not affected by this movement. It therefore has the same effect as if the SIL lens itself was moved along the optical axis. Due to refraction at the spherical surface of the SIL lens, the axial movement δz_{MO} of the objective and the axial movement δz of its focal plane are related by

[2]Using the mutual uncertainty relation: $\pm\Delta F = \sqrt{\left(\frac{\delta F}{\delta x}\right)^2 (\Delta x)^2 + \left(\frac{\delta F}{\delta y}\right)^2 (\Delta y)^2}$.

$$\delta z = n\delta z_{MO}, \tag{4.2}$$

where n is the c-Si refractive index. The above equation is derived from eq. (2.59) by successive Taylor expansions.

Depth of field was measured by considering the modulation amplitude of the intensity signal along the red line (period 1μm) in Figure 4.2 as a function of objective movement. The sampling interval $\Delta z_{MO} = 1\mu$m is the same as the resolution of the micrometer screw that moves the objective. The criterion for depth of field was chosen according to Wang et al. [64]: acceptable focus is set where the modulation is half the maximal modulation, i.e. the FWHM. Figure 4.5 shows the normalized modulation amplitude measured across the 1μm pattern as a function of the translated distance read from the screw. The FWHM is determined from the data as $\delta z_{MO} = 7.2 \pm 1\mu$m.

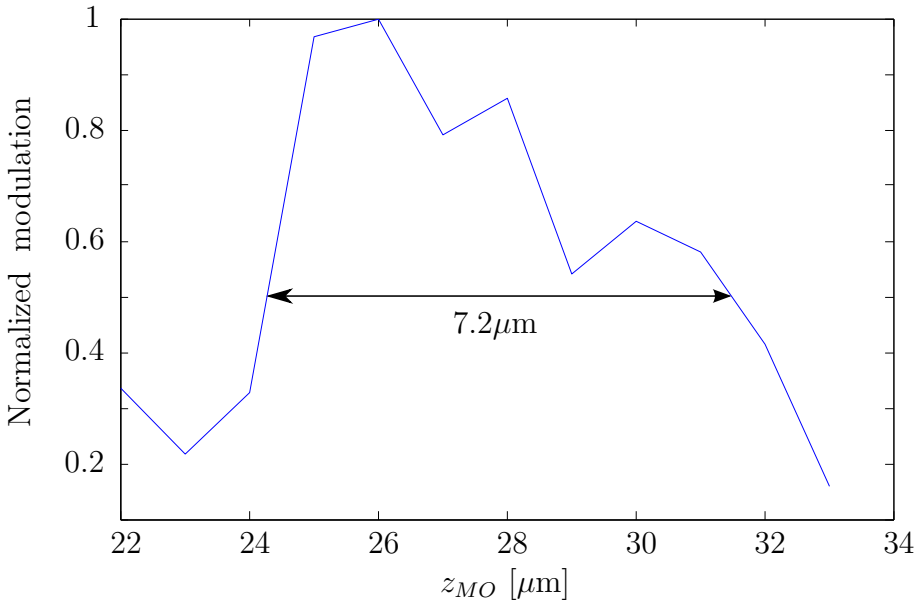

Figure 4.5: The measured modulation amplitude across the 1μm pattern as a function of axial movement of the objective z_{MO}. Values on the horizontal axis are the values read from the micrometer screw. The modulation is normalized to the largest modulation measured. The FWHM is determined as $7.2\mu m$.

Using eq. (4.2), the depth of field is determined as

$$\delta z = 3.506 \cdot 7.2 \pm 1\mu\text{m} = 25.2 \pm 3.5\mu m. \tag{4.3}$$

It is however noted that the curve in Figure 4.5 has a spiky rather than a smooth character. This should be taken into account when considering the reliability of this measurement.

4.2 Interferometric performance

The performance of the system as an interference microscope for depth profiling has been tested, and results are presented in the following. Attention is first aimed at testing the interference fringes' response to an object surface of varying tilt. Following, the depth profile of a flat test surface has been measured by interferogram scanning.

4.2.1 Interference fringes

An image showing interference fringes was obtained by introducing the reference field from the reference arm of the interferometer. A SIL lens with a clean object surface was used in the object arm as well as the reference arm. The alignment procedure of Section 3.3 was followed as closely as possible given the conditions. However, perfect focus of the two surfaces was not obtained due to a lack of features to focus on. The tilting stage was attached to the rear of the object arm, allowing the object surface to be vertically tilted. At this point, only the spacing of fringes are of interest; interferograms were not recorded. For increasing tilt angles with steps of 1°, still images were captured. Figure 4.6 presents a selection of the captured images for tilts in the range 0°-15°.

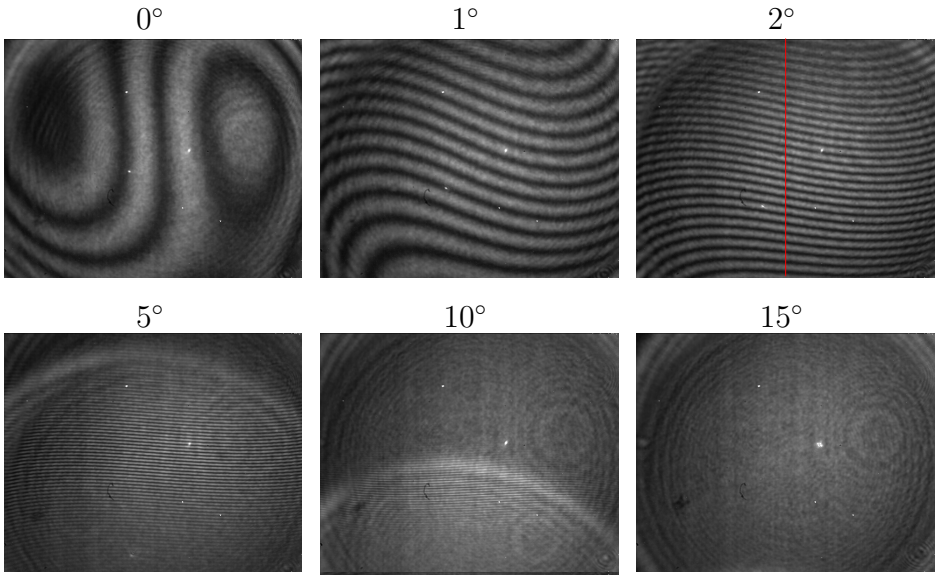

Figure 4.6: Interference fringes recorded for various object surface tilts. The red line in the 2° image is the vertical line at which fringe spacing is calculated for all images. **NB:** Fringes of short spacing may not be observable in this print. However, fringes were observed even for 15° tilt.

The curved character of the fringes, especially apparent for small tilts, is due to misalignment and defocus. Fringes are observed for all tilts up to 15°, although only in the bottom

part of the image for large tilts. This is due to lacking illumination of the object surface. For tilts larger than 15° fringes are no longer observable due to this. It is noted from Figure 4.6 that the spacing of fringes decreases with increasing tilt angle. Fringes were observed with decreasing attenuation from about 10°.

To quantify these results, an intensity signal was sampled along a vertical line centered in the image. This is the red line shown in the 2°-image of Figure 4.6. It is nearly orthogonal to the fringes for angles larger than 1°. With a Discrete Fourier Transform[3], the spatial period of the signal was calculated from the corresponding spatial frequency. The resulting periods are shown as a function of the tilt angle in Table 4.1, scaled by the pixel pitch and lateral magnification. The corresponding theoretical estimates using eq. (2.95) and the NA-factor $f = 1$ are also shown. Uncertainties are due to the accuracy at which spatial frequencies could be determined from the DFT. The width of spikes in the DFT was dramatically increasing for large tilt angles, hence the increasing uncertainty for large tilt angles. The same data is plotted in Figure 4.7.

Tilt angle [°]	Spatial period [μm]	Theoretical estimate [μm]
1	11.2338 ± 0.1770	10.4580
2	5.2153 ± 0.0381	5.2274
3	3.3963 ± 0.0162	3.4832
4	2.5627 ± 0.0092	2.6105
5	2.0286 ± 0.0058	2.0865
6	1.6593 ± 0.0039	1.7368
7	1.4319 ± 0.0029	1.4867
8	1.2483 ± 0.0022	1.2989
9	1.1064 ± 0.0017	1.1525
10	0.9935 ± 0.0014	1.0353
11	0.8958 ± 0.0011	0.9391
12	0.8203 ± 0.0009	0.8588
13	0.7528 ± 0.0012	0.7907
14	0.6953 ± 0.0017	0.7321
15	0.6730 ± 0.0022	0.6813

Table 4.1: Spatial periods in the vertical direction of images as a function of object surface tilt. Theoretical estimates are calculated using the NA-factor $f = 1$.

It is seen from Figure 4.7 that the experimental data closely follows the form of the theoretical predictions. It is however also noted that the experimental periods have slightly shorter values than their theoretical counterparts, with an exception for the value at 1°. This deviation can not be explained by the uncertainties, nor the NA-factor used in the theoretical estimates.

[3]Presented in Appendix A.

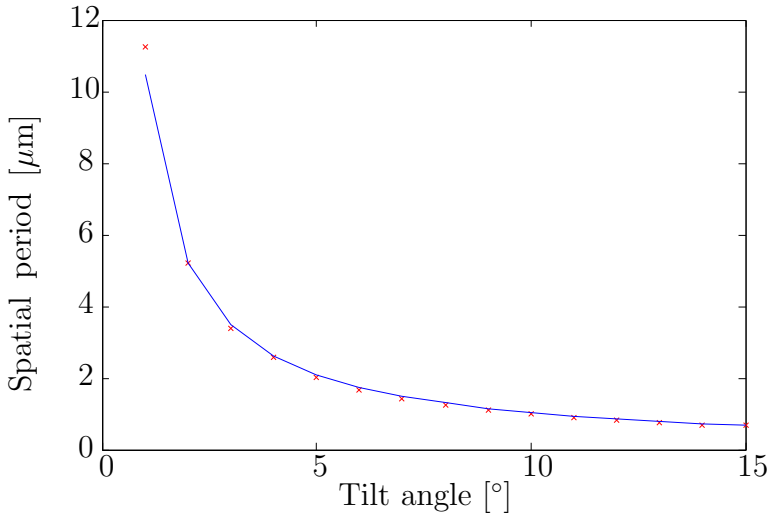

Figure 4.7: The spatial period of interference fringes vs. tilt angle, determined from experimental data (red crosses) and theory (blue line).

4.2.2 Surface profiling

The depth profile of a flat test surface has been measured by recording interferograms. It is recalled that an interferogram is recorded in every pixel of the image by scanning of the reference arm SIL lens. This section first presents results from the calibration of the scanning actuator, followed by a detailed analysis of one of the interferograms that surface depths were calculated from. Finally, calculated depth profiles are presented.

Calibration of the scanning actuator

The scanning actuator's voltage-displacement relation was uncovered from an analysis of interferograms. The same configuration as used in the analysis of fringes in Section 4.2.1 was used for this purpose. The object lens was tilted at 5°, and a 3D-interferogram was recorded by scanning of the reference arm. The tilt ensured that interference fringes were present in the image throughout scanning. Voltage steps were set to the value $(\Delta V)_c = 0.121\text{V}$, as calculated in eq. (3.7). Phase shifts between subsequent frames in the interferogram were calculated as averages over those pixels showing visibility larger than 5%. The resulting phase history is shown as the blue line of Figure 4.8a. A polynomial least-squares fit to this data is shown as the green curve in the same figure. This fit was used as the calibration function $\Delta\Phi(V)$ of eq. (3.8) when measuring depth profiles. Figure 4.8b shows the phase shifts calculated from an identical experiment where the calibration function has been employed in the scanning operation. It is seen that uniform phase shifts are not obtained despite the calibration.

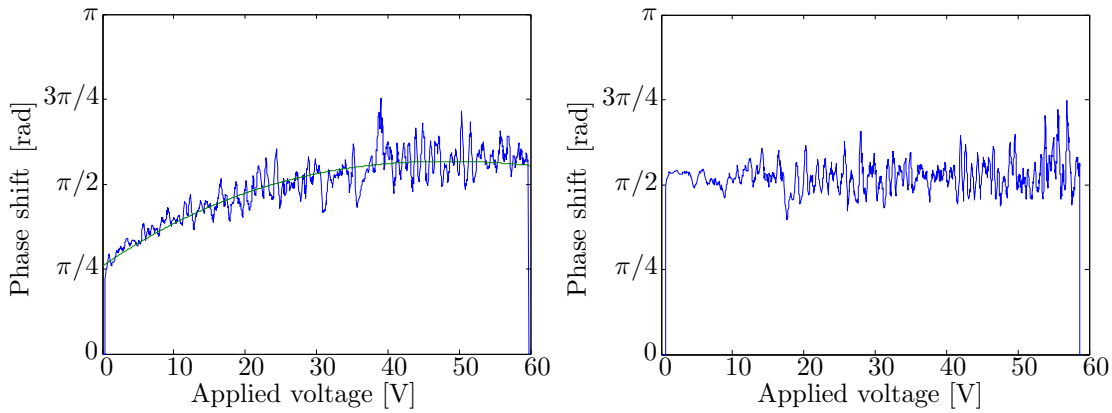

Figure 4.8: Phase shifts between subsequent frames in recorded interferograms as a function of the voltage applied to the scanning actuator. The phase shifts in a) are pre-calibration, where the green line is the least squares fit used for calibration. b) shows phase shifts from an interferogram where the calibration has been applied. The first and last three data points are zero due to a lack of sampling points for calculation.

Interferogram

The depth profiling capability of the system was tested by measuring the depth profile of a flat test surface. One of the interferograms recorded from that measurement is thoroughly analyzed here. To allow optimal alignment and focusing, the resolution chart deposited SIL lens was used in the object arm, and a defect was present on the surface of the reference arm SIL lens. A 3D-interferogram was recorded with 16 frames desired per period. The calibration function obtained in the previous section was used in the scanning operation.

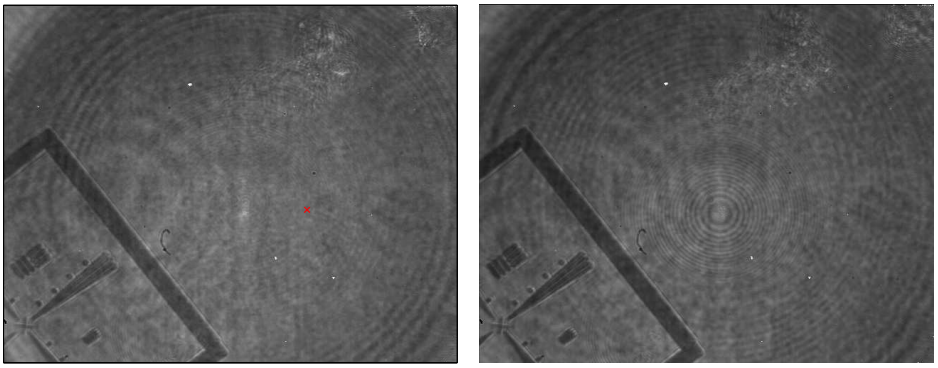

Figure 4.9: The first (left) and last (right) frame of the recorded 3D-interferogram. The red cross indicates the pixel chosen for interferogram analysis.

Figure 4.9 shows the first and last frames of the recorded 3D-interferogram. The resolution chart is seen to the bottom left, and small reference surface defects are seen in the top right corner. Both are in focus. It is noted that a circular fringe pattern is present near

the center in the last frame.

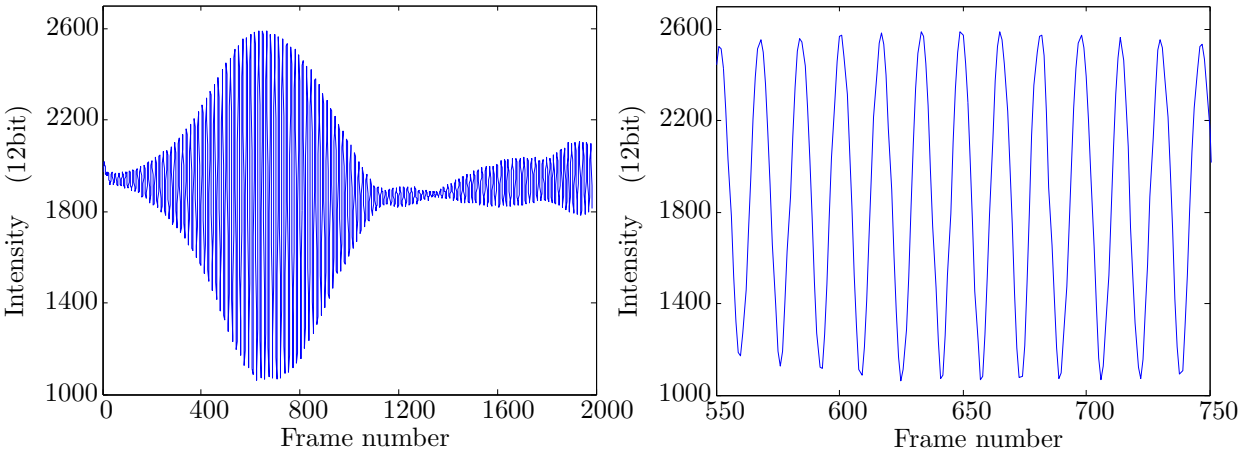

Figure 4.10: The interferogram recorded from the pixel indicated in Figure 4.9. Intensities are given by 12 bit representation. The horizontal axis denotes the interferogram frame number. a) shows the entire interferogram and b) shows a zoomed in window around the peak of the envelope.

The 1D-interferogram recorded from the pixel indicated in Figure 4.9 is shown in Figure 4.10a. The modulating envelope is seen between frame numbers 0 and 1200. The sinusoidal character of the signal is better viewed in the zoomed in window of Figure 4.10b. From manual inspection of the interferogram, the envelope peak seems located somewhere between frame numbers 600 and 700. The envelope does however seem skewed along the x-axis, as is best seen from the differing offset at either of its ends. For frame numbers larger than 1200, it is noted that the interference signal is reappearing.

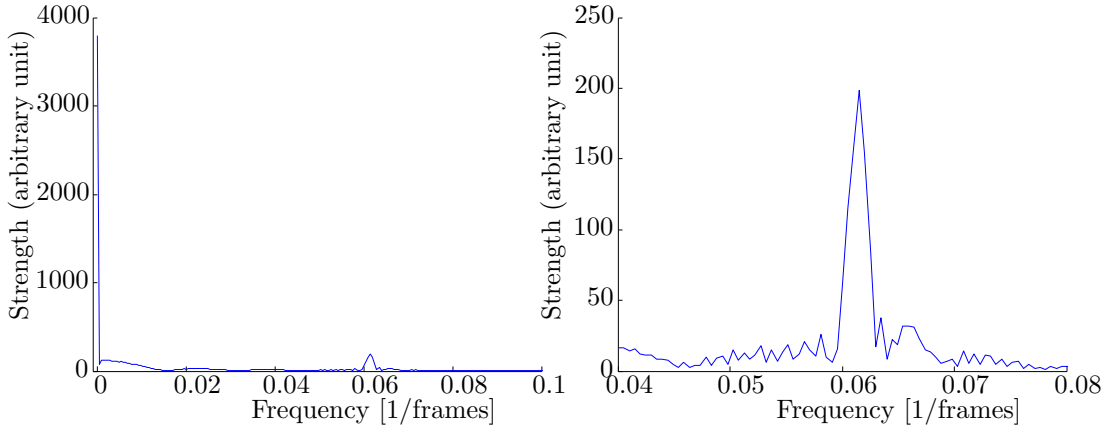

Figure 4.11: Positive-sided frequency spectrum of the interferogram in Figure 4.10, calculated by a fast fourier transform. The strength denotes the magnitude of the calculated frequency components. b) shows a zoomed in window of the spectrum in a).

A positive-sided frequency spectrum of the same interferogram was found by a DFT, and is shown in Figure 4.11. A small peak is present at the frequency 0.06152 frames^{-1}, which is the transform of the envelope function, shifted by the carrier frequency of the signal[4]. The frequency value suggests that the period of the interference signal is

$$p = \frac{1}{0.06125 \text{ frames}^{-1}} = 16.255 \text{ frames}, \tag{4.4}$$

which slightly deviates from the desired period. Two things are noted from the frequency spectrum. First, low-frequent components other than the offset frequency are present in the spectrum. These are seen for frequencies up to about 0.015 frames^{-1}. Secondly, the transform of the amplitude does not have the form expected from the transform of a smooth envelope. The transform is distorted by small spikes in its surrounding frequencies.

Depth profiles

The depth profile of the flat test surface was calculated by two different methods of envelope peak detection. In both, the offset was removed from the interferograms ahead of applying the algorithms. This was done by deleting the lowest order frequency component from the DFT, followed by an inverse DFT to reconstruct the signal.

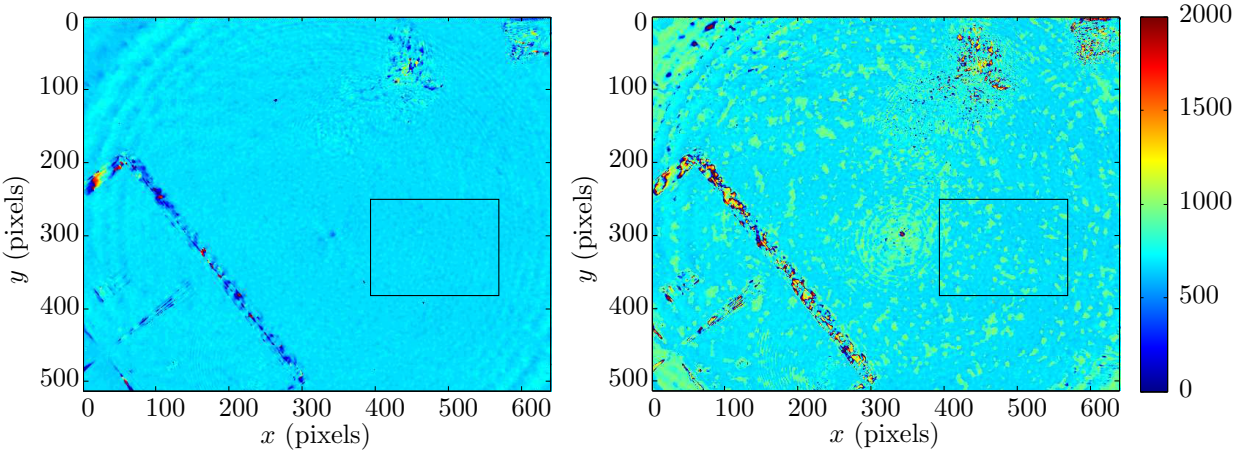

Figure 4.12: Surface depths calculated by (a) the DFT method and (b) the Hilbert transform method. Depths are represented in color as denoted by the color bar, with units of interferogram frame numbers. The black rectangles bounds the area of which the surfaces profiles are further inspected.

In Figure 4.12, depth profiles have been calculated by the two methods and are plotted in a colored image. The depth of each pixel is represented by its color, in units of interferogram

[4]The frequency spectrum of an amplitude modulated signal is presented in Appendix A.

frame number as shown by the color bar. It is noted that some of the features observed in the images of Figure 4.9 are visible also in the calculated surface profiles. These include the resolution chart, the defect and the illumination pattern. The depth calculated at pixels coinciding with the chart and the defect appear randomly and often out of limits.

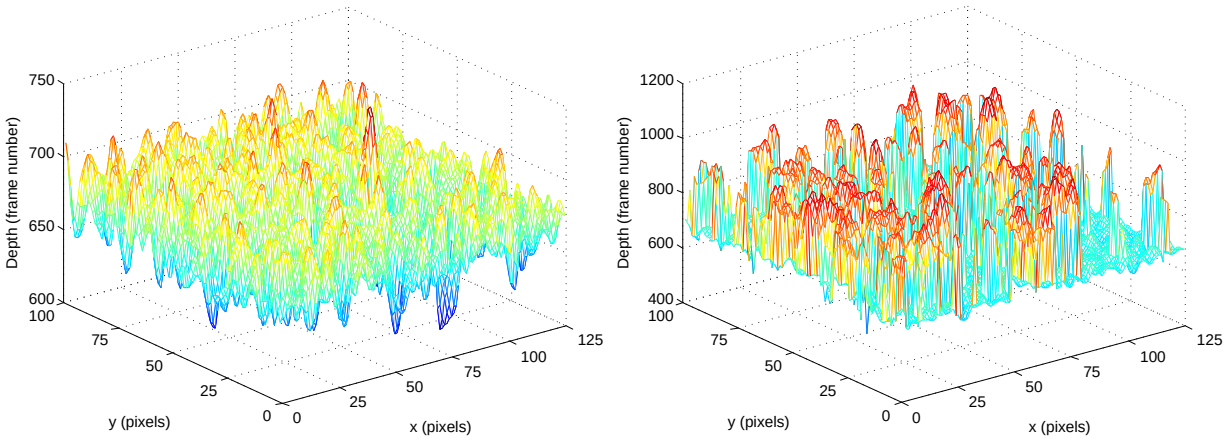

(a) DFT method (b) Hilbert transform method

Figure 4.13: Three-dimensional surface profiles corresponding to the area bounded by the black rectangles in Figure 4.12. Depths are represented, in units of frame numbers, by the vertical axis.

Figure 4.13 shows the corresponding three-dimensional surfaces to the area of inspection indicated by the black rectangles in Figure 4.9. The area represents a clean and flat test surface, free from disrupting features like the resolution chart and defects. Statistical data of the calculated depth distributions, including range, mean value μ and standard deviation[5] σ, are summarized in Table 4.2 for the two methods.

Method	Range (frames)	μ (frames)	σ (frames))
Hilbert transform	$[446, 1029]$	719.34	92.59
DFT	$[608, 738]$	670.47	14.80

Table 4.2: Statistical data for the depth distributions in Figure 4.13.

It is clear from these data that the DFT method gives the better replication of the flat test surface. This is seen from both the range and standard deviation of the depths, but also

[5]Calculated from the formula $\sigma = \sqrt{\frac{1}{N-1}\sum_{i=1}^{N}(z_i - \mu)^2}$.

from comparison of the mean value with the manual prediction of envelope peak position from the interferogram in Figure 4.10 (between frames 600 and 700). Therefore, only the depth distribution calculated from the DFT method is analyzed in the following.

Using the interferogram period calculated in eq. (4.4), the calculated depths range between $130/16.255 = 8$ interferogram periods, and the standard deviation is equal to $14.80/16.255 = 0.91$ periods. A 95% confidence interval[6], for the depths is $[-1.79, 1.79]$, in units of periods about the mean. In order to apply PSI algorithms for increased accuracy without introducing 2π-ambiguities, the half-width of this interval should be less than 0.5 periods. It can therefore not be expected to enhance accuracy by PSI.

Converting to units of physical depth[7] using eq. (2.95), the calculated depths range in an interval of width

$$\frac{8 \cdot 1.29\mu\text{m}}{2 \cdot 3.506} = 1.47\mu\text{m}. \tag{4.5}$$

The corresponding standard deviation is

$$\frac{0.91 \cdot 1.29\mu\text{m}}{2 \cdot 3.506} = 0.17\mu\text{m}. \tag{4.6}$$

4.3 Discussion

Results regarding the performance of the system are in the following discussed.

4.3.1 Imaging performance

A great deal of information on the imaging performance of the system was obtained from simply studying the image of the resolution chart in Figure 4.2. The observations made from this image are discussed before the measurements of lateral resolution, magnification and depth of field are treated.

Aberrations

The distortion of the image of the resolution chart in Figure 4.2 must be understood as image aberrations. The large NA of the system leaves it very susceptible to spherical aberrations at refracting surfaces. It is therefore very likely that the blurred replicas of the

[6] Assuming fluctuations to be randomly distributed about a mean value, with a well-defined standard deviation (standard distribution).

[7] Assuming the NA-factor $f = 1$.

chart patterns are caused by imaging rays with large angular departure from the optical axis. Spherical aberration causes the image formed by such rays to be offset laterally with defocus. This agrees with what was observed in the image; the blurred replicas are offset laterally from the patterns. The source of spherical aberration is most probably the flat faces of the cubic beam splitter. This assertion is supported by the fact that both the microscope objective and tube lens are corrected for such aberrations.

Illumination

It was observed that the image of the chart was unevenly illuminated and brightest near its center. The latter is most likely and effect of vignetting. Vignetting can be a result of the illumination optics or the imaging optics, but is suspected to be a result of the illumination optics [23]. What is seen is a partly defocused image of the light output from the fiber end. As the diameter of the single-mode field is small, this might be approximated as a point source. The illuminating system should therefore produce a defocused Airy disk in the object plane, which again is imaged to the image plane. Defocus causes the Airy disk to be both enlarged and blurred with rotational symmetry. Spherical aberration is also observed with rotational symmetry [29]. Therefore, the circular pattern in Figure 4.2 might be explained as a defocused image of the fiber output with spherical aberrations introduced by the beam splitter.

A more uniform illumination of the object would be achieved by applying Köhler illumination. In such a configuration, the light source is perfectly defocused in the object plane by projecting an image of the source to the front focal plane of the condenser lens [52]. In this system the condenser lens is a compound system constituted by the biconvex lens, the objective and the SIL lens. A great deal of effort has been put in trying to set up the system for Köhler illumination. By back-tracing a perfectly defocused beam from the object plane, distances between the optical components in the entrance arm of the interferometer have been calculated. However, a uniform illumination was not obtained in the current set-up, and may be a future improvement.

It is in the following argued, from a theoretical perspective, that Köhler illumination is practically hard to obtain with the design of this interference microscope. The argument is supported by Figure 4.14. The imaging design dictates the location of the SIL lenses relative to the infinity-corrected objective. Therefore, the distance between these cannot be altered without moving the object plane out of focus. In order to obtain Köhler illumination, an image of the light source must be formed in the front focal plane of the SIL lens. This plane is located roughly 1.2mm in front of the second principal plane of the objective. By applying the lens formula (2.61) with $z_i = -1.2$mm, an intermediate image must correspondingly be formed roughly 1.1mm in front of the objectives first principal plane. The proximity to this principal plane causes the illumination to be very sensitive to deviations from the theoretically calculated distance. Consequently, it is practically very hard to obtain uniform illumination

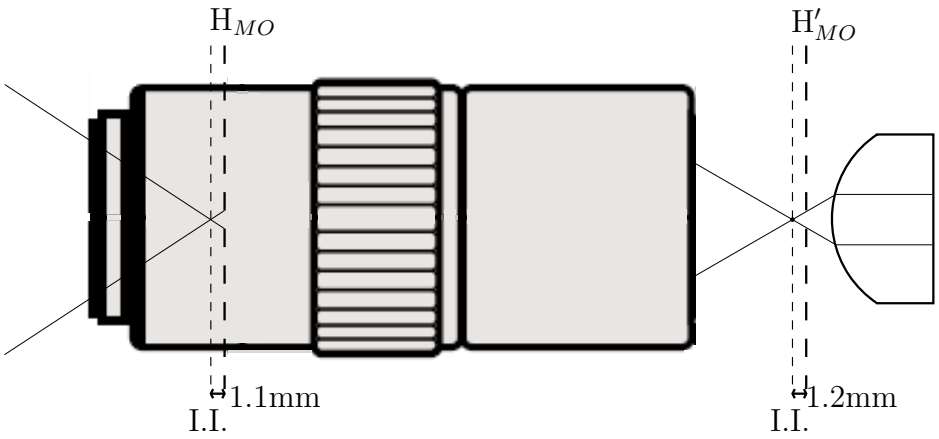

Figure 4.14: Theoretical sketch of illuminating rays through the objective and SIL lens with the system set up for Köhler illumination. The close proximity ($1.1mm$) of the first intermediate image to the first principal plane H_{MO} of the objective makes the illumination very sensible to axial misplacements.

Lateral resolution

The lateral resolution determined from the measurement (0.9μm) is poorer than the diffraction-limit calculated in Chapter 3 (0.56μm). This can in part be explained by the spherical aberrations previously discussed. It is seen from the spatial intensity signal in Figure 4.4 that aberrations cause a large variation of intensity outside the line pair gauge. It is likely that aberrations affect the intensity also within the pattern. The measured resolution still gives a good indicator of the lateral distance at which features can be resolved with this system. It is stressed that the measurement is subject to a very strict criterion, and that an even better resolution could be measured using a less strict criterion [63]. The resolution has only been measured in the object arm of the interferometer. It is only assumed that a similar resolution is obtainable in the reference arm.

Still, the measured resolution is superior to that of the previous prototype used by Simonsen, which was 1.6μm [2]. This is explained by moving to the Linnik configuration, in which imaging rays through the beam splitter are focused at infinity. It is believed that this significantly reduces aberrations. As a result of the improved resolution, interference fringes of shorter spacing should be observable with this prototype, allowing the topography of even steeper surfaces to be determined. This is a great advantage when characterizing the structure of surface damage induced by moving indentations.

Magnification

The measured lateral magnification (70.77x) is close to the theoretical estimate (70.12x). It is noted that the theoretical value is well covered within the range of the uncertainty ($\pm$4x),

and therefore the theoretical estimate should be trustworthy. The large magnification is essential to inspection of microscopic details in the surface damage induced by indentations.

Depth of field

The measured depth of field ($\delta z = 25.2\mu$m) is only slightly shorter than the calculated diffraction limit ($28.27\mu m$). The measured value should be seen in context with the spatial period (1μm) over which the modulation amplitudes were measured, since it is uncertain whether this has an effect on the measurement. For example, a different depth of field might have been measured if the 2μm pattern was chosen as the basis for the measurement. In any case, the measurement was performed over a spatial period very close to the lateral resolution. The spiky character of the modulation curve in Figure 4.5 does however raise questions on the credibility of the measurement. Seemingly, the lateral resolution's response to axial displacements of the object is not a smooth curve. This is most likely caused by the spherical aberrations previously discussed.

The measured depth of field propose a promising prospect for imaging of three-dimensional objects such as surface damage. With the c-Si surface in perfect focus, reflecting surfaces of depths down to 12μm should be imaged with acceptable focus.

The measured value is comparable to the coherence length of the light source, which has been determined in terms of FWHM to $l_c = 25\mu$m. It should therefore be expected that the modulating envelopes of recorded interferograms are formed by a combination of the temporal coherence and the limited axial resolution.

4.3.2 Interferometric performance

Results regarding the system's performance as an interference microscope are discussed in the following.

Interference fringes

The interference fringes' response to an object surface of varying tilt was tested in Section 4.2.1. It is observed from Figure 4.6 that fringes are not straight horizontal lines, but has a curved character. This is clearly a consequence of misalignment, since the alignment procedure had not been fully performed for this experiment. A more satisfactory alignment could be achieved by using SIL lenses with inherit surface defects, but this would also complicate the interpretation and quantification of the results. The curvature's effect on the vertical fringe spacing is apparent for small tilts, but decreasingly dominant for increasing tilts.

At tilts of 5° and larger, only parts of the object arm surface was illuminated by the light source. This is seen as a downwards shift of the illumination pattern. As a consequence, fringes are only present in the lower parts of the image. It is likely that the illuminating pattern takes a different shape when illuminating a tilted surface, but the center of the pattern should maintain its position if good alignment is met. It is therefore believed that the object SIL lens was laterally misaligned with the illuminating optics in this experiment. As a consequence, fringes could not be detected for tilts larger than 15°.

It was clearly seen from Figure 4.6 that the vertical fringe spacing decreased with increasing tilt angle, as is expected from theory. This is supported by the spatial periods calculated from the experiment as shown in Table 4.1. It is seen from Figure 4.7 that the spatial period's dependency on the tilt angle closely follows that predicted by theory with the NA-factor f=1. The measured periods are however slightly shorter than the theoretical values, except for the value at 1°. If anything, the experiment suggest an NA-factor less than unity. This is not in accordance with theory, as the NA-factor is always greater than or equal to unity. The shorter values might be explained as a systematic error caused by a slight tilt of the object surface at the start of the experiment, which was assumed to be 0°. If the vertical tilt was misaligned in the order of tenth of a degree, the experimental data in Figure 4.7 has been shifted by an equal amount to the left. This would possibly suggest an NA-factor larger than unity. The large deviation at 1° can however only be explained from other misalignments causing the curved fringe pattern. In any case, an NA-factor of f=1 should be a good approximation when relating fringes to axial depths.

It is seen from Figure 4.6 that the visibility of the fringe pattern is attenuated for large tilt angles. The attenuation was observed as most dramatic for tilts larger than 10°. This should be seen in context with the frequency response of the imaging system. Theoretically, the transfer of spatial frequencies from object to image is represented by a low-pass filter with a cut-off frequency as calculated in (3.6), corresponding to a spatial period of 0.92μm, which is roughly equal to the measured lateral resolution. It is likely that the same frequency response causes attenuation of interference fringes for short fringe spacings. Nevertheless, fringes are still observed even at 15°.

There is no evidence of camera array aliasing in the measured fringe spacings. Nor is this expected for such small tilt angles. The spatial Nyquist period of 0.5705μm set by the pixel pitch of the camera array suggests that aliases start occurring for tilt angles larger than

$$\tan^{-1}\left(\frac{1.29\mu\text{m}}{2 \cdot 3.506 \cdot 0.5705\mu\text{m}}\right) = 17.87°. \tag{4.7}$$

The Nyquist period sets the ultimate limit at which topographic slopes can be unambiguously determined. It is noted that fringes are detected close to this limit, although severely attenuated.

In summary, the results regarding interference fringes suggest that the interference microscope is capable of showing interference fringes for object surfaces inclined up to 15°.

Scanning calibration

It is seen from Figure 4.8a that applying uniform voltage steps to the scanning actuator does not result in uniform phase shifts in recorded interferograms. Since the phase shifts are directly related to the displacement of the actuator, it is established that the voltage-displacement relation is non-linear. From a large scale perspective, the displacement is an increasing function of voltage. This large-scale effect has been countered by incorporating the calibration function in the control routine of scanning. From a small scale perspective however, the displacement steps are disrupted by what seems like random fluctuations. These fluctuations cannot be countered by the calibration, as is seen for the phase shifts obtained by calibrated scanning in Figure 4.8b. Fluctuations constitute a disruptive factor when recording interferograms, since they cause non-uniform sampling intervals.

The origin of the fluctuations are in the following briefly discussed. Since the electrical signal supplied to the actuator is low-pass filtered, it is unlikely that high-frequent noise created in the electrical circuit is the source of this undesired behavior. It may however be caused by mechanical vibrations in the laboratory equipment. This argument is supported by the large size of the apparatus, leaving it very susceptible to vibrations from the surroundings. It is also likely that thermal expansion of the piezoelectric material causes the disturbance, or that the actuator is simply defected.

Interferogram analysis

The modulating envelope was clearly seen in the recorded interferogram of Figure 4.10a. From manual inspection, it was determined that the peak was located between frame numbers 600 and 700. A more accurate location was however not achieved from simple inspection. A number of disturbing factors were seen in the interferogram, including a surprising reappearance of interference signal and a slight skew of the modulating envelope.

The interference signal that was seen to reappear outside the envelope is most likely related to the circular fringe pattern observed in the last frame of the interferogram shown in Figure 4.9. Since the visibility of the interference signal should be severely attenuated in this region of the interferogram due to the limited coherence length, these fringes must be caused by reflections at surfaces other than the flat object surfaces. The circular symmetry of the fringe pattern suggests that the pattern is caused by reflections at one or more spherical surfaces. It is therefore lead to believe that reflections from the SIL lenses' spherical surfaces are the source of this interference signal. Although these surfaces are anti-reflection coated, a small amount of light is still reflected upon illumination. This explanation does however

imply that the two SIL lenses are of slightly unequal thickness. If they were in fact of equal thickness, this interference signal would coincide with the envelope.

Another disturbing factor is the skewed character of the envelope, best identified by the differing values of offset intensity on the two ends. This observation is discussed further in the next section regarding the surface profiles.

The frequency spectrum of the same interferogram was shown in Figure 4.11. From Fourier transform theory[8], it is expected that the spectrum of an amplitude modulated sinusoidal signal, such as this interferogram, is the transform of the modulating function shifted by the frequency of the signal. A larger offset component should also be expected. A prominent peak was in fact observed very near to the predicted frequency of the signal. The narrowness of this peak justifies the use of Bedrosian's product theorem in the Hilbert transform method of envelope detection[9]. The peak does however not resemble the smooth Fourier transform of a symmetric function. If this peak was in fact the transform of the temporal coherence function $|\Gamma(\tau)|$, it should have the form of the light source's spectral distribution $S(\nu)$ since these are related by transform pairs. This does not seem to be the case. The curve of the peak is distorted by a large dent on its right side. It is probable that this dent is caused by the interference signal from the SIL lenses' spherical surfaces. The peak is also surrounded by a series of small spikes on either side. This might be due to the non-uniform sampling intervals. Since the Discrete Fourier Transform assumes uniform sampling intervals, deviations from this concept may cause leakage into the frequency components neighboring the carrier frequency. In addition, low-frequent components other than the offset frequency are also prominent in the spectrum. These are believed to be a disrupting factor when measuring the location of the peak, especially by the DFT method since it uses the first non-trivial frequency component of the rectified signal for calculations.

Depth profiles

It was obvious from the calculated surface profiles in Figure 4.13 that the DFT method of peak detection gave the best replication of the flat test surface. However, the statistical analysis showed that even this method was far from accurate enough for PSI algorithms to be applied for enhanced accuracy without introducing ambiguities. The range of calculated depths (1.47μm) is very large compared to the microscopic chipping depths expected from moving indentations. This suggests that surface profiles of indentations would provide very little reliable information. It is therefore concluded that the present system is not capable of providing meaningful surface profiles during indentations.

Possible explanations for the inaccurate surface profiles are now discussed. The surface profiles in Figure 4.13 provide very little information about the origin of the inaccuracy. It is however seen in Figure 4.9 that the circular pattern, previously explained as a defocused

[8]Presented in Appendix A.

[9]Bedrosian's product theorem is presented in Appendix B.

and aberrated image of the light source, is apparent also in the calculated surface profiles. In other words, the non-uniform illumination seems to have an effect on the calculation of depths. If this is the case, an effect of the illumination should be observable in interferograms as well. It is therefore reasonable to believe that the skew of the envelope is caused by illumination effects. As the reference SIL lens is scanned in the axial direction, the defocus of the light source image is slightly altered in the object plane. The result is a dynamic illumination pattern during scanning. This argument is supported by the differing illumination patterns of the first and last frames of the interferogram, as seen in Figure 4.9. For any pixel, this causes the magnitude of the reference amplitude to be a slowly varying function of the scan position z in addition to the time delay τ, i.e. $U_r = U_r(z, \tau)$. It then follows that the interference signal is disturbed in both the offset intensity and the envelope:

$$I(z, \tau) = I_o + I_r(z) + 2\Re\left\{\langle U_o^* U_r(z, \tau)\rangle\right\} \tag{4.8}$$

Due to the small displacement of the reference mirror, the z-dependencies are most likely slowly varying. The term $I_r(z)$ might explain the skewed character of the envelope. It might also explain the low-frequent components observed in the frequency spectrum of the interferogram. As for the disturbance of the envelope, it is possibly manifested as the lack of smoothness in the Fourier transform of the envelope. Both of these effects are disturbing factors in the calculation of depths, and can possibly explain some of the inaccuracy. It is nevertheless hard to explain exactly why the illumination pattern is present in the surface profiles. The disturbed offset could possibly be eliminated by a digital low-pass filtering of the interferogram. The disturbance of the envelope is however hard to eliminate digitally. It seems that this problem can only be solved by reevaluating the optical design for a more uniform illumination.

It is also believed that the interference pattern outside the envelope affects the depth calculations. Though this pattern is most likely due to reflections from the spherical SIL lens surfaces, it significantly disturbs the spectrum of the signal. It is therefore apparent that it is a disturbing factor in the frequency spectrum of the coherence envelope. This effect could possibly be reduced by disregarding the interference signal outside the envelope when determining peak positions. Additional algorithms would need to be developed for such a windowing to be applied. One idea would be to select a suitable window based on the contrast of the interference signal. This suggestion is however not applicable if the two interference signals overlap. It seems that a general solution to the problem would be to reduce reflections at the spherical SIL lens surfaces.

A third possible explanation is that the non-uniform sampling intervals previously discussed impedes an accurate calculation of depths. The sampling rate of approximately 16 samples per period is by far sufficient to avoid alias frequencies. However, if the non-uniform sampling intervals in fact has an effect on the frequency spectrum of the interferogram, this will affect the calculated depths.

It must also be questioned whether the coherence envelope is narrow enough for its peak to be accurately determined. The neighborhood of the peak is rather flat as seen in Figure 4.10b, meaning that the visibility is not much larger for the zeroth order fringe than it is for the first few orders. This can affect the accuracy at which depths are calculated. A future enhancement of the system can therefore be to replace the current SLD source with a light source of an even broader spectrum.

4.3.3 Concluding remarks

Although spherical aberrations are present, the system shows good performance in conventional imaging, with a lateral resolution superior to that of the previous prototype. The measured axial resolution predicts that interferograms are modulated by a combination of temporal coherence and imaging effects, although the reliability of this measurement is questionable. The response of interference fringes to a tilted object surface predicts that reflecting surfaces inclined up to 15° can be reproduced by interference microscopy. The system is however not yet capable of reproducing accurate depth profiles by scanning interferograms. For this reason, it has not been attempted to monitor moving indentations by calculation of depth profiles.

In order to enhance the accuracy of depth profiles, the optical design needs reevaluation. It is believed that a more uniform illumination will reduce the amount of low-frequent spectral components in interferograms, thereby enhancing the accuracy at which depths are calculated by the methods used in this this text. This should be achieved by setting up the system for Köhler illumination. However, this does most likely also involve a reevaluation of the imaging optics. Reflections at the spherical SIL lens surfaces must also be reduced to a minimum in order to be able to record clean interferograms.

Future enhancement should also involve better control of the scanning actuator's displacement, in order to sample interferograms at uniform intervals. This involves a thorough analysis of the error sources causing the fluctuating behavior, or a sophisticated control system for the scanning operation.

Chapter 5

Results and Discussion - Moving Indentation Experiments

Results from moving indentation experiments are in the following presented and discussed.

Moving indentations have been performed on two different experiments, by two different inspection techniques. In the first experiment, on sample 1, the process was monitored by imaging mode only. In the second experiment, on sample 2, the process was monitored by calculating interferometric phase maps. The orientation of the diamond lattice of the silicon crystal with respect to its flat surface was the same for both samples; the [100]-directions of the crystal was aligned with the sample surface. With respect to the corners of the indenter however, the crystal orientation was different for the two samples. Perfect focus was obtained ahead of both experiments by focusing on defects. The results from the two experiments are presented and discussed separately.

5.1 Imaging mode

The first indentation experiment was performed with the indenter corners misaligned by approximately 30° with the [100] crystal direction, as shown in Figure 5.1.

At the moment the picture in Figure 5.1 was taken, there was no physical contact between the indenter and the silicon surface. The quadratic pattern of bright and dark gray levels was identified as Fizeau fringes resulting from waves reflected at the indenter surface interfering with waves reflected at the silicon surface. As the indenter tip was moved even closer to the surface, it was observed that the fringes converged to the center. The center of the fringe pattern was therefore identified as the projected position of the indenter tip. The moment of first impact was noted by observing an abrupt change in the gray level of the center fringe. At this point, the indent actuator length read from the gauge reader was noted and used for reference.

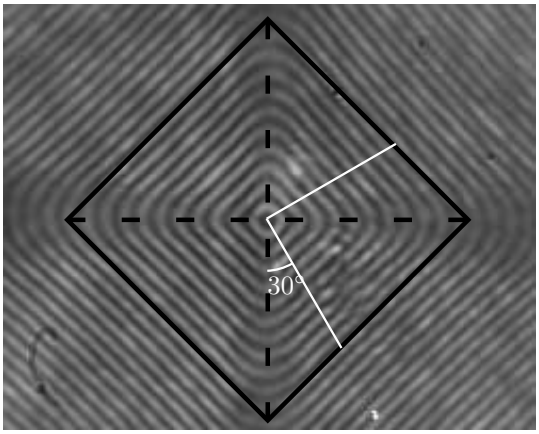

Figure 5.1: The orientation of the crystal axes with respect to the corners of the indenter. White lines are [100]-directions in the crystal, stapled lines are the indenter corners projected onto the surface.

After impact, the indenter was stepwise penetrated into the silicon by applying voltage steps of size $\Delta V = 0.935$V to the indent actuator. The speed of each step was set to 0.374V/s. Between every voltage step, a picture was taken and the penetration depth noted. After reaching a depth of 1.78μm, the scratching process was initiated by applying the same procedure and settings to the scratch actuator. After actuating to a scratch length of 27.52μm, the indenter was retracted from the sample.

Figure 5.2 shows a selection of the images captured during the experiment. The field of view is the same in all images. The indicated actuation lengths are the values read when the associated picture was taken. As there are significant delays and fluctuations in the readers, these values are merely indicators of the actual depth and scratch lengths. In addition, the actuation length at the moment of first impact is necessarily an uncertain quantity dependent on the size of the voltage step before impact. This causes a positive shift of the actual indent lengths. Right before impact was observed, the indenter was actuated a length 0.95μm from the last reading.

Some observations from the images in Figure 5.2 are in the following presented. Lateral directions in the images are denoted by cardinal directions. It is seen from Figure 5.2b that the indentation has caused a dark region to laterally spread out from the center of the fringe pattern. This region is however not uniformly distributed about the center; it extends longer in the south and east directions. Within the region, the visibility of the Fizeau fringes are increasingly attenuated towards the center. In the scratching process represented by Figures 5.2c-f, the dark region is increasingly spread. This spread was observed during the experiment as sudden transitions. Especially apparent is the hemispheric-shaped region that appears to the east in Figure 5.2d. Sudden transitions to darkness occur most prominently to the west, but also to the north and south. Dark regions are bounded by sharp edges to the Fizeau fringes at some boundaries. At other

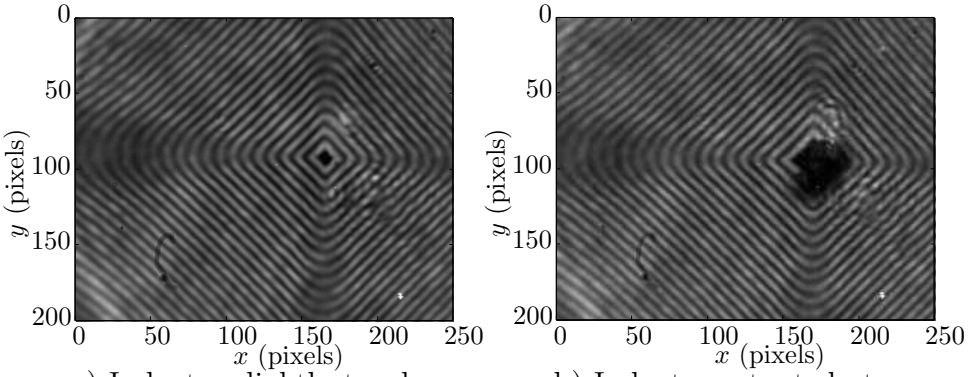

a) Indenter slightly touches the surface.

b) Indenter actuated at 1.78μm depth.

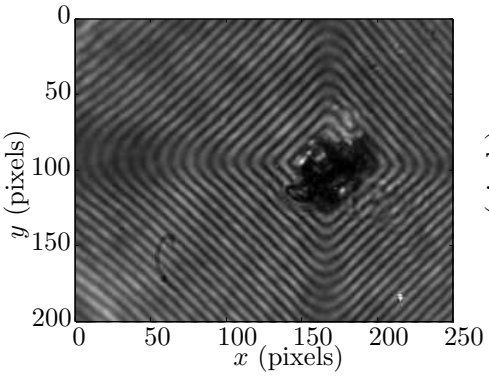

c) Scratch actuated at 2.05μm.

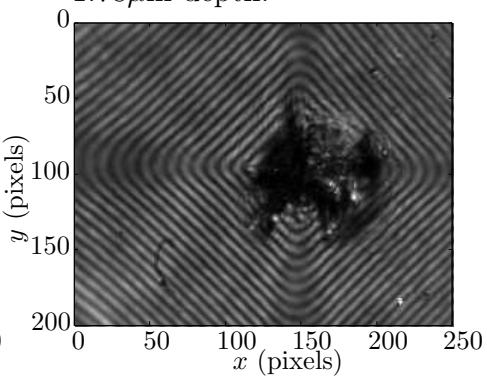

d) Scratch actuated at 7.48μm.

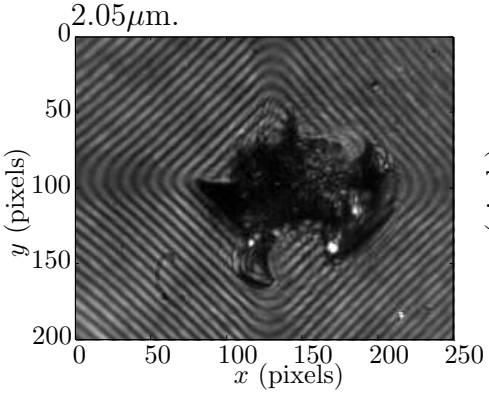

e) Scratch actuated at 12.60μm.

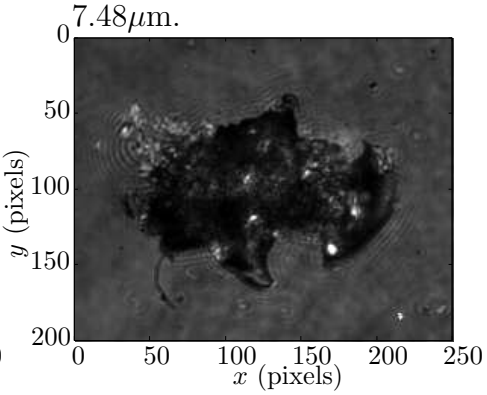

f) Scratch actuated at 27.52μm and indenter retracted from sample.

Figure 5.2: A selection of images of the silicon surface during indentation and scratching. No reference light is present, interference fringes are due to reflections from the indenter surface.

boundaries, the edges are less sharp and attenuated Fizeau fringes are seen. Strongly reflecting spots are observed at some points within the dark region, especially within the hemisphere previously mentioned. In Figure 5.2f, where the indenter has been retracted

from the sample, the edges of the absorbing region are distorted by spherical aberrations.

5.2 Interferometric phase maps

In the second experiment, on sample 2, the [100]-axes of the crystal were approximately aligned with the indenter corners[1]. With the reference field and hence interference fringes present, five frames of mutual phase difference approximately $\pi/2$ were recorded at a selection of stages in the process. These were later used to calculate phase maps of high contrast. The same settings and procedure as in the previous experiment was followed. When first impact was observed, the indent actuator had been moved 0.72μm since the last reading. The indenter was buried to a penetration depth of 2.88μm before the scratching process was initiated.

It should be noted, that the camera driver temporarily stopped responding at an early stage in the scratching process. This caused a very long delay in the experiment. When the driver finally responded, the read values of penetration depth and scratch length were significantly different from the previous readings. The read values were increased by 1.20μm and 0.37μm, respectively. It is unknown whether this deviation is caused by gauge reader delay or actual expansion of the piezoelectric materials. In the presented results, the indicated values are those read from the gauge readers.

The phase maps calculated from the indentation and scratching process are presented separately in the following sections.

Indentation

Figure 5.3 shows a selection of six phase maps recorded and calculated during indentation. The corresponding penetration depths are indicated for each map. The interferometric phase is given in grayscale as indicated by the color bars. This is the phase of frame number three out of the five frames captured, according to eq. (2.99). It is stressed that the maps are modulo 2π. Therefore, transitions from black to white does in general not represent an abrupt change in phase.

The vertical variation in phase present in all maps are interference fringes due to misalignment of the sample and reference surfaces. These were useful when calibrating the scanning actuator, and affects the interpretation of the maps only to a very limited degree. It is evident that the Fizeau fringes that was observed in the previous experiment are present also in the calculated phase maps. The visibility of this pattern is however low.

Some observations from Figure 5.3 are noted. The impact of the indenter tip on the surface is seen as the white spot in image Figure 5.3a. At later stages, this spot has spread out

[1] With the angle in Figure 5.1 equal to zero.

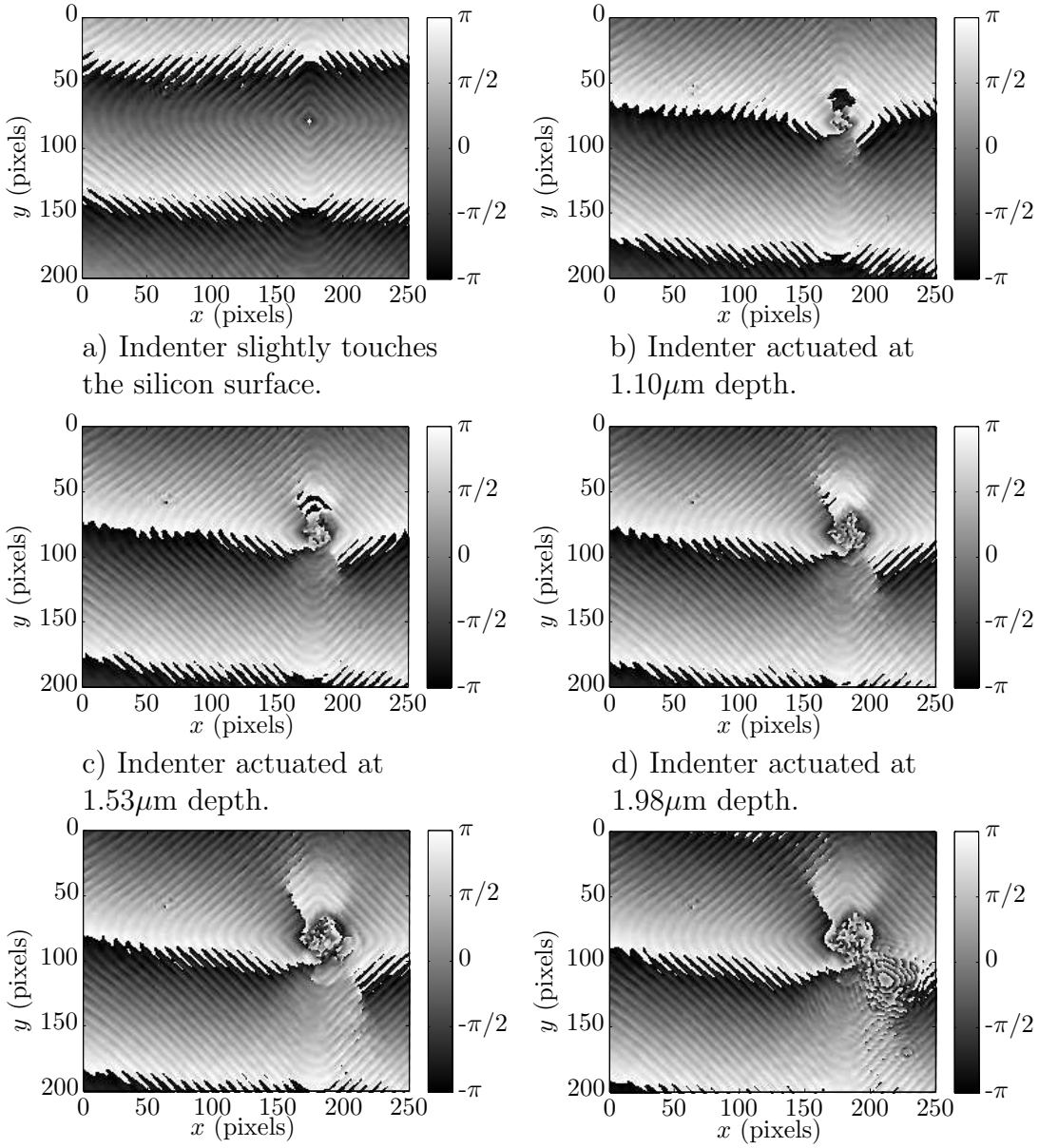

a) Indenter slightly touches the silicon surface.

b) Indenter actuated at 1.10μm depth.

c) Indenter actuated at 1.53μm depth.

d) Indenter actuated at 1.98μm depth.

e) Indenter actuated at 2.41μm depth.

f) Indenter actuated at 2.88μm depth.

Figure 5.3: A selection of phase maps obtained during the process of indenting the sample. Interferometric phase is given modulo 2π as represented by the grayscale bars.

to form a region of high-frequent variation in phase. Abrupt phase changes are seen for areas both to the north and south of the indenter tip in Figures 5.3b-e. Both areas have sharp edges on one side and less sharp edges on the other sides. The two areas seem to extend with increased penetration. In Figure 5.3f, a large region of interesting character has suddenly appeared to the south-east of the tip, covering the area of the abrupt phase

change present in Figure 5.3e. This region connects with the other regions of high-frequent variation in phase.

Scratching

A selection of eight phase maps calculated from the scratching process is shown in Figure 5.4. All the shown maps where recorded after the inconvenient response delay of the camera driver. At this stage, the value of the penetration depth was determined to 4.08μm from the reading. This value stayed approximately constant throughout scratching.

The features observed in Figure 5.3f are still present in Figure 5.4a, including the high-frequent patterns and the abrupt phase transition along the line to the north-west of the indenter tip. In addition, a phase change seems apparent along a line extending to the south-west, although not very sharp. In Figure 5.4b, the high-frequent region surrounding the tip has been further spread in all directions, but the lines of sharp phase changes are still intact. In Figure 5.4c however, these lines have been partly covered by high-frequent patterns. The same patterns also extend in the direction opposite of the indenter movement. In Figure 5.4d, a very large region of high-frequent patterns suddenly extends here, with a smaller area of less frequent phase in its interior. This area is significantly distorted in Figures 5.4f-h. High-frequent regions are increasingly more present through Figure 5.4e-h, particularly in the direction of indenter movement but also to the north and south.

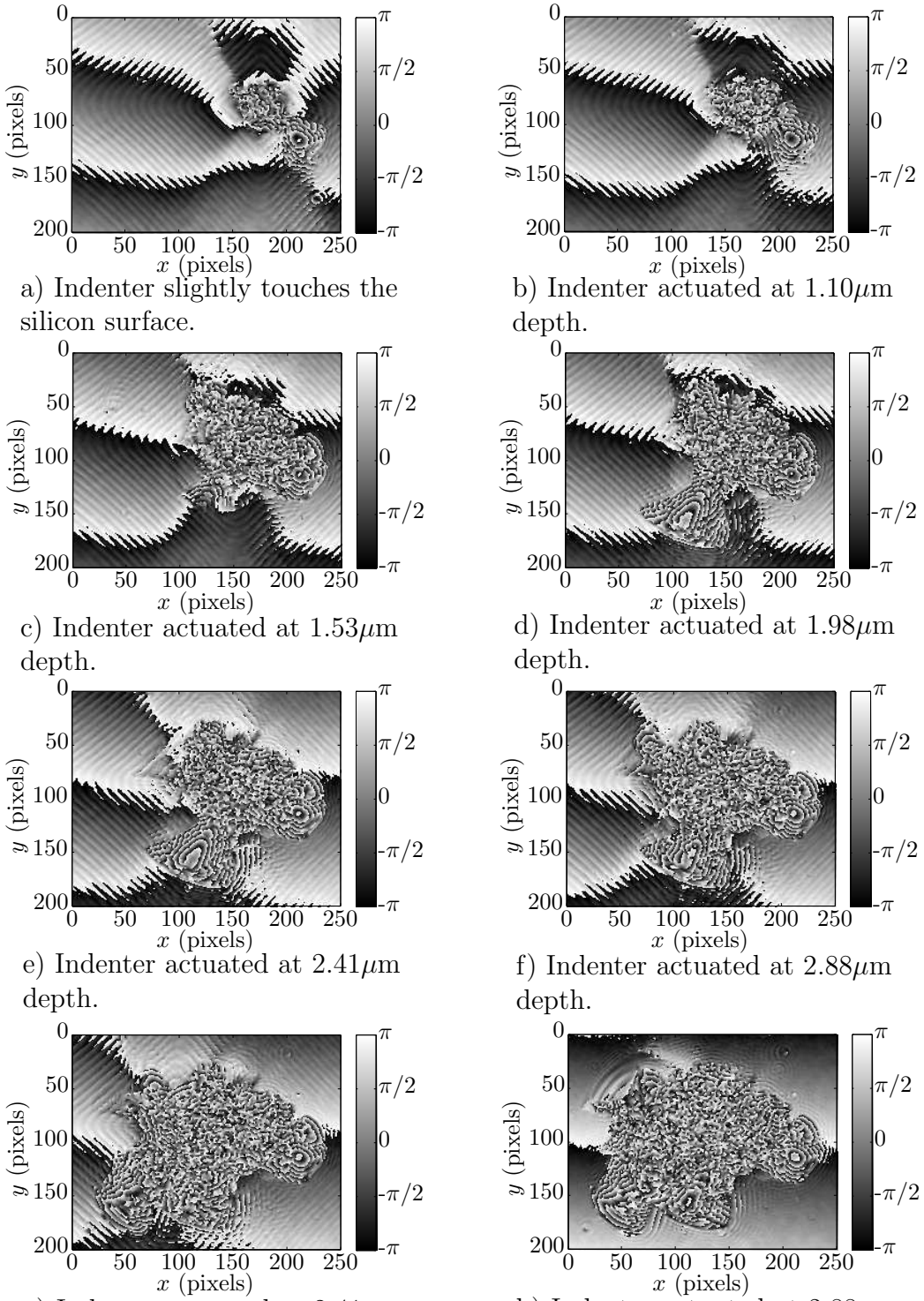

a) Indenter slightly touches the silicon surface.

b) Indenter actuated at 1.10μm depth.

c) Indenter actuated at 1.53μm depth.

d) Indenter actuated at 1.98μm depth.

e) Indenter actuated at 2.41μm depth.

f) Indenter actuated at 2.88μm depth.

g) Indenter actuated at 2.41μm depth.

h) Indenter actuated at 2.88μm depth.

Figure 5.4: Phase maps obtained during the scratching process.

5.3 Discussion

In this section, the results from the moving indentation experiments are tried put in context with the material removal mechanisms presented in Section 2.6. The discussion is separate for the results obtained on sample 1 by pure imaging, and the phase maps obtained with sample 2.

5.3.1 Imaging mode

Plastic deformations

It was observed from Figure 5.2b that a dark region spread out from the indenter tip as a result of submerging the indenter in the c-Si material. This region is not bounded by sharp edges, but by attenuated Fizeau fringes. It may therefore indicate that a large amount of absorption occurs in this region. Absorption of light is not expected in the diamond structure of c-Si because of its small extinction coefficient for the wavelengths used. It may therefore be that light is absorbed by a region of plastic deformation causing transition to a different crystal structure. In such a transition, it is very plausible that optical properties are severely altered. The absorption might therefore be explained as a transition to a crystal phase with large extinction coefficient κ. According to theory, the thickness of the deformation region is largest under the indenter tip and decreases radially. This could explain why Fizeau fringes are decreasingly attenuated radially from the center.

It is however strange that as a result of indenter penetration, the absorbing area has a larger extent in some radial directions than others. According to theory, the deformation region should spread out with radial symmetry from the indenter tip. A possible explanation to this is that the indenter movement is slightly misaligned with the normal of the c-Si surface.

Chippings

The spread of the dark region with sharp edges must be understood as material being chipped away from the c-Si surface. The sharp edges mark a boundary between areas of surface damage and areas of the clean unaffected surface. Such an edge is especially apparent to the west in Figure 5.2e. It is likely that these edges are formed by lateral cracks extending to the surface and chipping away pieces of material. This is supported by the observation that the transitions occurred suddenly. The less sharp edges where the Fizeau fringes are observed with attenuated visibility cannot be explained in the same way. It can perhaps be an effect of plastic deformations.

The evolution of chippings is clearly seen throughout Figures 5.2c-f. It is evident that the surface damage occurs mainly in the direction of indenter movement, but also to the

lateral sides of the movement. An exception is the large hemisphere that was observed to the east in Figure 5.2d, in the direction opposite of the indenter movement. The final extent of the surface damage, seen in Figure 5.2f, can be interpreted as a channel extending in the direction of indenter movement. The width of this channel is roughly 120 pixels at maximum, corresponding to an object-space width of roughly 34μm given the lateral magnification. It is likely that the width of this channel is largely dependent on the submersion of the indenter.

The strongly reflecting spots observed within the chippings are most probably due to surface roughness. With a very rough surface it must be expected that some light experiences multiple reflections before being imaged. If in addition total internal reflection is experienced at these reflections, the reflected light will be imaged with very large intensity. This may be a rare scenario, causing such spots to be observed occasionally only. Other areas on the chipped surface may have slopes so steep that large parts of the reflected light is not accepted by the imaging system, causing the imaged area to appear dark. It is recalled that the object-side NA only accepts a cone of rays of half-angle $\theta = 23.57°$.

5.3.2 Phase maps

Moving now to the phase maps obtained from sample 2. The presence of Fizeau fringes also in the phase maps is expected since they represent the distribution of phase in the optical field reflected from the sample.

The vertical stripes seen in Figure 5.3a are due to interference fringes caused by a slight misalignment between the object and reference surfaces. Between each phase map of the indentation process, these are seen to be shifted vertically. This may be due to a lack of repeatability in the scanning actuator. The starting displacement of the scanning actuator may not be the same for all phase maps, causing the phase calculated for any given pixel to be different in between measurements. It is however seen, especially in the phase maps of Figure 5.4 recorded during the scratching process, that these stripes appear with a large curvature at later stages. The stripes seem, to some extent, to be converging towards the center of the Fizeau fringe pattern. This could possibly be a consequence of the silicon surface being compressed by the pressure applied by the indenter, causing the undamaged surface not to be perfectly flat anymore.

The pattern of high-frequent variation of phase spreading out from the indenter tip in Figures 5.3 is believed to be a manifestation of a plastic deformation region. It is recalled from the discussion of sample 1, by imaging only, that this region was observed as a dark region, perhaps caused by a transition to an absorbing crystal phase. This could explain the irregularity of these phase patterns, as there is very little amplitude from the object for the reference field interfere with, causing a very limited visibility. The large regions of high-frequent phase variation that occur suddenly must be areas of chipped-away material. Throughout the scratching process presented in Figure 5.4 it is increasingly hard

to distinguish these two regions from one another.

Lateral cracks

The abrupt changes in phase observed during indentation are believed to represent the edges of lateral cracks in the sub-surface of the silicon crystal. When a sub-surface crack is present in the material, it introduces an additional interface at which light is partly transmitted and reflected. In order to argue that such a crack can introduce a phase change in the interference signal, a simplified example is in the following considered. The interference signal is a result of three waves interfering: U_o, U_c and $U_r(z)$. z denotes the reference amplitude's dependency on the scanning operation. These are the waves reflected from the object surface, crack interface and reference surface, respectively. It is for simplicity assumed that these waves are completely coherent and that their amplitudes are of equal magnitude. For a given pixel, the interference signal is thus found from the intensity

$$\begin{aligned} I(z) &= \langle (U_o + U_c + U_r(z))(U_o + U_c + U_r(z))^* \rangle \\ &= I_0(1 + \cos(\Phi_c - \Phi_o) + \cos(\Phi_c - \Phi_r(z)) + \cos(\Phi_o - \Phi_r(z)), \end{aligned} \tag{5.1}$$

where the Φ's denote the phase of the respective waves. Applying a trigonometric identity[2] to the last two cosines yields

$$\begin{aligned} I(z) &= I_0(1 + \cos(\Phi_c - \Phi_o) + \cos(\tfrac{\Phi_c - \Phi_o}{2}) \cos(\tfrac{\Phi_c + \Phi_o}{2} - \Phi_r(z)) \\ &= I_0' + I_1 \cos(\tfrac{\Phi_c + \Phi_o}{2} - \Phi_r(z)), \end{aligned} \tag{5.2}$$

where $I_0' = I_0(1 + \cos(\Phi_c - \Phi_o))$ is a constant offset term and $I_1 = I_0 \cos(\frac{\Phi_c - \Phi_o}{2})$. The last line of eq. (5.1) shows that the phase recorded at this pixel is $\frac{\Phi_c + \Phi_o}{2}$ rather than just Φ_o as would be expected without the crack. In spite of the assumptions used in this argument, it seems plausible that a sub-surface crack introduce a change of phase in the calculated maps.

Figure 5.5 shows the edges of the lateral cracks observed in Figures 5.4e-f highlighted in red. It should be expected that cracks are entirely bounded by sharp changes in phase, indicating their edges. This is however not the case, as some transitions are rather continuous. This makes it hard to precisely determine the lateral extent of the cracks. It is seen, from left to right in Figure 5.5, that a large piece of material is removed in the vicinity of where there previously was a crack. The same is seen between Figures 5.4b-c, where a piece of material is removed near the lateral crack to the north of the indenter tip. This supports the theory that material is removed when lateral cracks extend to the surface. The material removal can thus, to some extent, be foreseen by observing lateral cracks in the phase maps.

[2] $\cos\theta + \cos\phi = 2\cos\frac{\theta+\phi}{2}\cos\frac{\theta\phi}{2}$

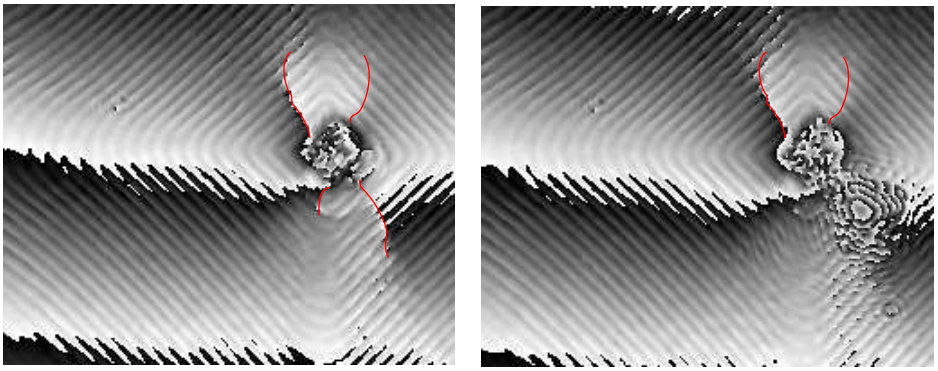

Figure 5.5: Phase maps of the silicon surface right before (left) and after (right) a large piece of material has been chipped away during the indentation process. The edges of lateral cracks are highlighted in red. Phase maps are taken from Figures 5.3e-f.

Surface topography

The topography of the surface damage is determinable from the phase maps only to a limited extent. In most cases, the phase pattern within chippings is highly irregular, and does not resemble contour lines. This makes the patterns hard to interpret. It is therefore difficult to determine whether the phase calculated for a given pixel actually represents the depth at which reflection occurs. By pure imaging, it was observed that surface-damaged areas reflected very little light. The visibility of interference fringes must therefore be expected to be small. In addition, it was established in Chapter 4 that fringes are severely attenuated for inclination angles exceeding approximately 15°. Chances are therefore that irregular patterns are results of wrongly calculated phases, caused by little or non-existing visibility in the interference signal. These patterns should therefore be interpreted as noise rather than topographic contours.

In some cases however, phase variations calculated from within the damaged area are more regular, and can be interpreted as contour lines. It is possible that such patterns actually represent relative depths on the material-removed surface. An example is shown in Figure 5.6, where contour lines have been attempted drawn in red for the large chipping observed in Figure 5.4e. Consequent lines are separated by a depth of 184nm, according to eq. (2.95). The contour lines surround an area on the surface that is nearly flat. It can only be assumed, because of the 2π-ambiguity, whether this is a "valley" or a "hill" on the surface. Most probably it is the former, with the contours on either side almost extending up to the undamaged surface.

5.3.3 Concluding remarks

When operating in imaging mode only, the system is capable of monitoring the lateral extent of surface damage in c-Si during moving indentations. Chippings are observed as

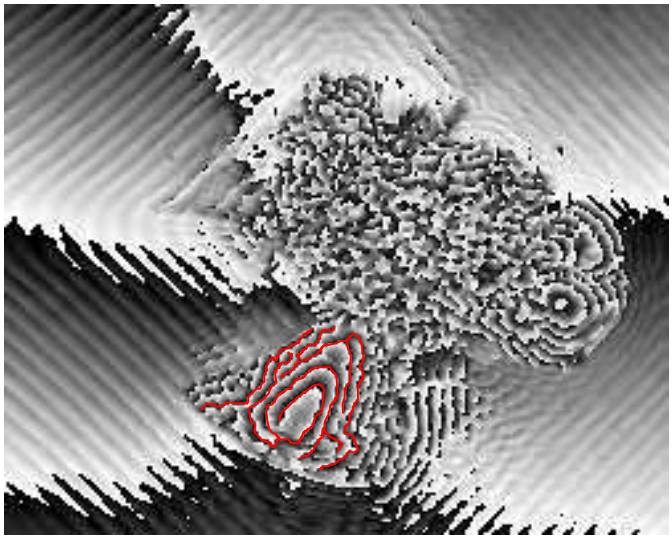

Figure 5.6: Phase map of the surface damage during scratching. Contour lines relating phases to relative depths are attempted highlighted in red.

sudden transitions to reduced irradiance, observed as dark areas in the image. Sharp edges separating the dark areas from Fizeau fringes are most likely a result of lateral cracks that has extended to the surface. It is also believed that plastic deformations can be seen as visibility attenuation of Fizeau fringes. This attenuation is also seen at the less sharp edges of chippings. The final surface damage is seen to be formed by connection of chippings. The imaging mode does however not provide any depth information about the removal mechanisms.

By calculating interferometric phase maps during the process, lateral cracks in the sub-surface are identified by abrupt phase changes in the Fizeau fringe pattern. Chippings are observed with this method of monitoring also, and can to some degree be foreseen by the lateral sub-surface cracks. The phase pattern within chippings is in general hard to interpret. Only in special cases can the spatial variation in phase be regarded as contour lines representing depth. The calculated phase is however 2π-ambiguous, meaning that contours must extend to the undamaged surface in order to give an absolute measure of the chipping depth.

The results obtained from moving indentation experiments have been almost entirely qualitative in terms of topography. In order to achieve a better understanding of removal mechanisms, the topography of surface damage must be obtained accurately and quantitatively. This requires the ability to measure surface profiles by recording low coherent interferograms, which has proven unsuccessful earlier in this report. It is also desirable to be able to measure the depth of sub-surface cracks, which is an interesting topic for further work.

The results obtained in this chapter do however rise questions regarding the ultimate lim-

itations of the attempted profiling technique for this specific application. It has already been established that fringes are severely attenuated for clean surfaces inclined above 10°. However, the lack of irradiance observed from reflections within the surface damage, as seen in the imaging mode, also contributes to attenuate fringes. It is likely that this further complicates profiling, since fringes may not be properly resolved in the interferogram frames.

Chapter 6

Conclusion

An interference microscope for sub-surface inspection of c-Si has been developed, with specific application to monitoring of moving indentation experiments. The system has been tested in terms of both imaging performance and its interferometric capabilities. Measurements regarding imaging performance indicate that microscopic features of the c-Si surface can be imaged with very good detail over a sufficiently large range of depths. The optical resolution of the system is superior to that of the previous prototype. In addition, an analysis of the interference fringes' response to a tilted object surface show that fringes are detectable for surfaces inclined up to approximately 15°. This is very close to the ultimate limit set by the Nyquist period of the camera array. Together, these results indicate that the new prototype should be capable of identifying topographic structures of even steeper slopes than previously achieved.

Results from the measurement of a flat test surface's depth profile do however show that surface depths are calculated with very large inaccuracy. The range of calculated depths is too large for accuracy to be enhanced by applying algorithms of phase-shifting interferometry. Since the profile of even a simple flat surface is inaccurately measured, it cannot be expected that measurements of complex surfaces provide meaningful information. It has therefore been concluded that the system is not yet capable of accurately replicating the depth profiles of chippings during moving indentations. Based on analysis of the results, it has been argued that the large inaccuracy is due to a combination of non-uniform illumination, undesired reflections and non-uniform sampling intervals in the scanning of interferograms.

Moving indentation experiments have been performed with inspection by both conventional imaging and calculation of interferometric phase maps. Results show that the system is capable of monitoring the evolution of surface damage throughout the process. In addition, lateral cracks in the sub-surface have been identified from phase maps. Chippings are to some degree foreseen by these lateral cracks. It has also been verified that the final surface damage is formed by connection of chippings. The phase maps of surface damage are

however hard to interpret, and can only to a limited extent be identified as topographic maps showing contour lines. Even in special cases where this is possible, the depth of chippings cannot be determined if not the contour lines extends to the undamaged surface.

At the present stage of development, the interference microscope is capable of identifying some of the mechanisms in material removal by fixed-abrasive sawing. Findings are however predominantly qualitative and still rely on the interpretation of 2π-ambiguous phase maps for measures of depth. For an increased knowledge of removal mechanisms, firmer results based on quantitative and accurate measures are needed. Such information can be obtained from calculation of depth profiles, as has been attempted in this report. Future enhancement of the system therefore relies on improving the accuracy at which depths can be determined from interferograms. The discussions given in this report suggest that reevaluation of the optical design is a necessary action for future improvements.

Bibliography

[1] T. R. C. of Norway, "Next generation production equipment for the production of ultra-thin silicon solar cell wafers." http://www.forskningsradet.no/servlet/Satellite?c=Prosjekt&cid=1244733932712&pagename=ForskningsradetNorsk/Hovedsidemal&p=1181730334233, 2009.

[2] O. Simonsen, "Characterization of solar cell wafers with low coherence interferometry," Master's thesis, Norwegian University of Science and Technology.

[3] W. Van Sark, L. Korte, and F. Roca, *Physics and Technology of Amorphous-Crystalline Heterostructure Silicon Solar Cells*. Engineering Materials, Springer, 2011.

[4] T. Markvart and L. Castañer, *Solar Cells: Materials, Manufacture And Operation*. Elsevier Advanced Technology, 2005.

[5] A. Einstein *et al.*, "On the electrodynamics of moving bodies," *Annalen der Physik*, vol. 17, no. 891, p. 50, 1905.

[6] Nobelprize.org, "The nobel prize in physics 1921." http://www.nobelprize.org/nobel_prizes/physics/laureates/1921/, 2012.

[7] C. Chen, *Physics of Solar Energy*. John Wiley & Sons, 2011.

[8] R. Castellano, *Solar Panel Processing*. Éd. des Archives contemporaines, 2010.

[9] M. Green, K. Emery, Y. Hishikawa, W. Warta, and E. Dunlop, "Solar cell efficiency tables (version 39)," *Progress in Photovoltaics: Research and Applications*, vol. 20, no. 1, pp. 12–20, 2012.

[10] A. Luque and S. Hegedus, *Handbook of Photovoltaic Science and Engineering*. John Wiley & Sons, 2011.

[11] V. Lindroos, M. Tilli, A. Lehto, and T. Motooka, *Handbook of Silicon Based MEMs Materials and Technologies*. Micro & Nano Technologies, William Andrew/Elsevier, 2009.

[12] H. Möller, C. Funke, M. Rinio, and S. Scholz, "Multicrystalline silicon for solar cells," *Thin Solid Films*, vol. 487, no. 1, pp. 179–187, 2005.

[13] H. Lee, *Thermal Design: Heat Sinks, Thermoelectrics, Heat Pipes, Compact Heat Exchangers, and Solar Cells*. John Wiley & Sons, 2010.

[14] H. Möller, "Basic mechanisms and models of multi-wire sawing," *Advanced Engineering Materials*, vol. 6, no. 7, pp. 501–513, 2004.

[15] H. Du and Y. Yu, "Present situation and development trend of precise wire cutting technology of silicon wafers," *Advanced Materials Research*, vol. 102, pp. 762–766, 2010.

[16] N. Watanabe, Y. Kondo, D. Ide, T. Matsuki, H. Takato, and I. Sakata, "Characterization of polycrystalline silicon wafers for solar cells sliced with novel fixed-abrasive wire," *Progress in Photovoltaics: Research and Applications*, vol. 18, no. 7, pp. 485–490, 2010.

[17] Y. Gao and P. Ge, "Analysis of grit cut depth in fixed-abrasive diamond wire saw slicing single crystal silicon," *Solid State Phenomena*, vol. 175, pp. 72–76, 2011.

[18] K. Gastinger and L. Johnsen, "Near-infrared low-coherence speckle interferometry (nir-lcsi) as a tool for the investigation of silicon in solar cell production," in *Proceedings of SPIE*, vol. 7387, p. 738713, 2010.

[19] K. Gastinger, L. Johnsen, O. Simonsen, and A. Aksnes, "Inspection of processes during silicon wafer sawing using low coherence interferometry in the near infrared wavelength region," in *Proceedings of SPIE*, vol. 8082, p. 80820U, 2011.

[20] L. Kittang, "Resolving optical sub-sampling ambiguity in near-infrared low coherence interferometry by envelope detection.".

[21] M. Born, E. Wolf, and A. Bhatia, *Principles of optics: electromagnetic theory of propagation, interference and diffraction of light*. Cambridge Univ Pr, 1999.

[22] B. Saleh and M. Teich, *Fundamentals of photonics*, vol. 22. Wiley Online Library, 1991.

[23] F. Pedrotti and L. Pedrotti, *Introduction to optics*, vol. 28. Prentice Hall, 1993.

[24] D. Meschede, *Optics, Light and Lasers: The Practical Approach to Modern Aspects of Photonics and Laser Physics*. Physics textbook, John Wiley & Sons, 2008.

[25] C. Kittel, *Introduction To Solid State Physics*. Wiley, 2005.

[26] E. Hecht, *Optics*. Pearson education, Addison-Wesley, 2002.

[27] M. Green and M. Keevers, "Optical properties of intrinsic silicon at 300 k," *Progress in Photovoltaics: Research and Applications*, vol. 3, no. 3, pp. 189–192, 1995.

[28] W. Lauterborn and T. Kurz, *Coherent optics: fundamentals and applications*. Springer Verlag, 2003.

[29] H. Gross, W. Singer, M. Totzeck, F. Blechinger, and B. Achtner, *Handbook of Optical systems*, vol. 2. Wiley Online Library, 2005.

[30] P. Hariharan, *Basics of Interferometry*. Electronics & Electrical, Elsevier Academic Press, 2007.

[31] J. Goodman, *Introduction to Fourier Optics, Roberts & Company Publishers*. Greenwood Village, CO, USA, 2005.

[32] K. Sharma, *Optics: Principles And Applications*. Academic Press, 2006.

[33] R. Ditteon, *Modern geometrical optics*, vol. 37. Wiley, 1998.

[34] M. Gu, *Principles of three dimensional imaging in confocal microscopes*. World Scientific Pub Co Inc, 1996.

[35] L. Novotny and B. Hecht, *Principles of Nano-Optics*. Cambridge University Press, 2006.

[36] L. Rayleigh, "Xxxi. investigations in optics with special reference to the spectroscope," *The London, Edinburgh, and Dublin Philosophical Magazine and Journal of Science*, vol. 8, no. 49, pp. 261–274, 1879.

[37] M. Pluta, *Advanced Light Microscopy: Principles and basic properties*. No. v. 1, Elsevier, 1988.

[38] S. Mansfield and G. Kino, "Solid immersion microscope," *Applied physics letters*, vol. 57, p. 2615, 1990.

[39] H. Huff, W. Bergholz, and K. Sumino, *Semiconductor Silicon 1994: Proceedings of the Seventh International Symposium on Silicon Materials Science and Technology*. Proceedings (Electrochemical Society), Electrochemical Society, 1994.

[40] I. Abdulhalim, "Theory for double beam interference microscopes with coherence effects and verification using the linnik microscope," *Journal of Modern Optics*, vol. 48, no. 2, pp. 279–302, 2001.

[41] A. Harasaki, J. Schmit, and J. Wyant, "Improved vertical-scanning interferometry," *Applied optics*, vol. 39, no. 13, pp. 2107–2115, 2000.

[42] K. Creath, "Calibration of numerical aperture effects in interferometric microscope objectives," *Applied optics*, vol. 28, no. 16, pp. 3333–3338, 1989.

[43] E. Ingelstam and L. Johansson, "Correction due to aperture in transmission interference microscopes," *Journal of Scientific Instruments*, vol. 35, p. 15, 1958.

[44] W. Kuhn, "Wavelength multiplexed quantitative differential interference contrast microscopy," June 11 2002. US Patent 6,404,544.

[45] P. Hariharan, B. Oreb, and T. Eiju, "Digital phase-shifting interferometry: a simple error-compensating phase calculation algorithm," *Applied optics*, vol. 26, no. 13, pp. 2504–2506, 1987.

[46] J. Schmit and A. Olszak, "High-precision shape measurement by white-light interferometry with real-time scanner error correction," *Applied optics*, vol. 41, no. 28, pp. 5943–5950, 2002.

[47] L. Deck, "Interferometric methods and systems using low coherence illumination," Feb. 22 2000. US Patent 6,028,670.

[48] Y. Gao, P. Ge, and Z. Hou, "Study on removal mechanism of fixed-abrasive diamond wire saw slicing monocrystalline silicon," *Key Engineering Materials*, vol. 359, pp. 450–454, 2008.

[49] T. Kiriyama, H. Harada, and J. Yan, "Finite element modeling of high-pressure deformation and phase transformation of silicon beneath a sharp indenter," *Semiconductor Science and Technology*, vol. 24, p. 025014, 2009.

[50] Superlum, "Superlum — faq." `http://www.superlumdiodes.com/faq.htm`, 2011.

[51] A. Köhler, "Ein neues beleuchtungsverfahren für mikrophotographische zwecke," *Zeitschrift für wissenschaftliche Mikroskopie und für mikroskopische Technik*, vol. 10, no. 4, pp. 433–440, 1893.

[52] M. Spencer, *Fundamentals of Light Microscopy*. Iupab Biophysics Series, Cambridge University Press, 1982.

[53] J. Fraden, *Handbook of Modern Sensors: Physics, Designs, and Applications*. Springer, 2010.

[54] J. Leachtenauer and R. Driggers, *Surveillance and Reconnaissance Imaging Systems: Modeling and Performance Prediction*. Artech House Optoelectronics Library, Artech House, 2001.

[55] Xenics, "Xcontrol infrared camera software - graphical user interface." `http://www.xenics.com/en/infrared_camera/infrared_camera_software_and_sdk/xcontrol_infrared_camera_software_-_graphical_user_interface.asp`, 2012.

[56] N. I. Corporation, "Ni labview - improving the productivity of engineers and scientists - national instruments." `http://www.ni.com/labview/`, 2012.

[57] I. The MathWorks, "Matlab - the language of technical computing." `http://www.mathworks.se/products/matlab/`, 2012.

[58] Thorlabs, "Apt software." `http://www.thorlabs.com/software_pages/APTSoftware.cfm`, 2012.

[59] G. Gautschi, *Piezoelectric Sensorics: Force, Strain, Pressure, Acceleration and Acoustic Emission Sensors, Materials and Amplifiers*. Engineering Online Library, Springer, 2002.

[60] J. Cox, *Fundamentals of Linear Electronics: Integrated and Discrete*. Delmar Thomson Learning, 2002.

[61] A. Alavudeen, A. N. Venkateshwaran, and J. Jappes, *A Textbook of Engineering Materials and Metallurgy*. Laxmi Publications Pvt Limited, 2006.

[62] J. Dossett and H. Boyer, *Practical Heat Treating*. Asm International, 2006.

[63] S. Smith, *The Scientist and Engineer's Guide to Digital Signal Processing*. California Technical Pub., 1997.

[64] R. El-Maksoud, L. Wang, J. Sasian, and V. Valencia, "Depth of field estimation: theory, experiment, and application," in *Proceedings of SPIE*, vol. 7429, p. 74290W, 2009.

[65] R. Bracewell, *The Fourier transform and its applications*. McGraw-Hill series in electrical and computer engineering, McGraw Hill, 2000.

[66] E. Brigham, *The fast Fourier transform and its applications*. Prentice-Hall signal processing series, Prentice Hall, 1988.

[67] A. Poularikas, *Transforms and Applications Handbook*. Electrical Engineering Handbook Series, CRC Press, 2009.

[68] R. Lyons, *Understanding Digital Signal Processing*. Prentice Hall, 2010.

[69] Y. Silvan, "gaussian curve fit - file exchange - matlab central." `http://www.mathworks.com/matlabcentral/fileexchange/11733-gaussian-curve-fit`, 2006.

[70] Xenics, "xenics infrared and thermal imaging solutions." `http://www.xenics.com`, 2012.

[71] M. A. Corporation, "Mitutoyo america corporation." `http://www.mitutoyo.com`, 2012.

[72] ThorLabs, "Thorlabs, inc. - your source for fiber optics, laser diodes, optical instrumentation and polarization measurement and control." `http://www.thorlabs.com`, 2012.

Appendix A

Fourier transform methods

This appendix discusses the Fourier transform and presents how it is used to determine both the carrier frequency and peak of an amplitude modulated signal

Continuous Fourier Transform

The Fourier transform $F(\nu)$ of a signal $f(x)$ is defined as [65]

$$F(\nu) = \mathfrak{F}\{f(x)\} = \int_{-\infty}^{\infty} f(x)e^{-i2\pi x\nu}\mathrm{d}x, \tag{A.1}$$

and represents the signal in the domain of frequencies s. The original signal $f(x)$ is found from its transform by an inverse Fourier transform defined by

$$f(x) = \mathfrak{F}^{-1}\{F(\nu)\} = \int_{-\infty}^{\infty} F(\nu)e^{i2\pi x\nu}\mathrm{d}x. \tag{A.2}$$

Convolution

The convolution $h(x)$ of two functions $f(x)$ and $g(x)$ is given by the integral

$$h(x) = f(x) * g(x) = \int_{-\infty}^{\infty} a(u)b(x-u)\mathrm{d}u. \tag{A.3}$$

The convolution theorem of Fourier analysis states that the Fourier transform of a convoluted function is the transform product of the respective functions joining in the convolution:

$$H(\nu) = F(\nu)G(\nu). \tag{A.4}$$

Conversely, the transform of a product is a convolution of the respective transforms. That is, if

$$h(x) = f(x)g(x), \tag{A.5}$$

then its transform is

$$H(\nu) = F(\nu) * G(\nu). \tag{A.6}$$

Symmetry

An important property of Fourier transforms is symmetry. Bracewell [65] shows that, for an even function, its associated transformed is also even. An example is the Gaussian function centered at $x = 0$,

$$f(x) = e^{-\pi x^2}, \tag{A.7}$$

whose Fourier transform is also a Gaussian function centered at $x = 0$:

$$F(s) = e^{-\pi s^2}. \tag{A.8}$$

Discrete Fourier Transform

The continuous Fourier Transform described above has a discrete version, namely the Discrete Fourier Transform which is defined as [66]

$$F(n) = \sum_{k=0}^{N-1} f(k)e^{-i2\pi nk/N}, \tag{A.9}$$

where N is the number of samples in the discrete signal. k and n represent length[1] and frequency, respectively, in discrete values of the range $[0, N-1]$. The physical values are

[1] Or some other physical quantity like time.

computed from these as $\nu = n/(N\Delta x)$ and $x = k\Delta x$, where Δx is the sampling length. The discrete transforms $F(n)$ are known as Fourier coefficients.

Accordingly, the discrete inverse transform is

$$f(k) = \frac{1}{N}\sum_{n=0}^{N-1} F(n)e^{i2\pi nk/N}. \tag{A.10}$$

A.1 AM Carrier frequency

The Fourier transform of the cosine function $\cos(2\pi\nu_c x)$ is [65]

$$\mathfrak{F}^{-1}\{\cos(2\pi\nu_c x)\} = \frac{1}{2}[\delta(\nu-\nu_c)+\delta(\nu+\nu_c)], \tag{A.11}$$

where ν_c denotes the carrier frequency of the cosine. An amplitude modulated (AM) signal is a product of a such a cosine and a modulating function $a(x)$. The modulated signal reads

$$f(x) = a(x)\cos 2\pi\nu_c x. \tag{A.12}$$

If the transform of $a(x)$ is $A(\nu)$, the Fourier transform of the modulated signal is, using eq. (A.6),

$$F(\nu) = A(\nu) * \frac{1}{2}[\delta(\nu-\nu_c)+\delta(\nu+\nu_c)] = \frac{1}{2}[A(\nu-\nu_c)+A(\nu+\nu_c)]. \tag{A.13}$$

Hence the transform of the modulated signal is a superposition of two versions of $A(\nu)$, shifted by the carrier frequency in the positive and negative frequency domains. If the modulating function is an even function with a global maximum at zero, such as the Gaussian discussed above, the carrier frequency can be found from a discrete Fourier transform. Considering only the one-sided spectrum, ν_c is found as the frequency associated with the largest Fourier coefficient[2].

A.2 Peak detection

The following method of peak detection is presented in a patent by Deck [47].

An amplitude modulated signal such as that of an interferogram recorded with low coherent light may be modeled as

[2]Ignoring a possible DC-offset which may be present.

$$f(x) = a_0 + a(x)\cos(2\pi\nu_c x), \tag{A.14}$$

where a_0 is a constant offset and $a(x)$ is a modulating function. $a(x)$ is an envelope function of low frequency components and has a maximum for some value of x. The aim of this method is to find that specific value. The offset in (A.14) may be removed by subtracting the root mean square[3] of the signal. Squaring the resulting signal yields a rectified signal

$$\begin{aligned} f_{rect}(x) &= (f(x) - a_0)^2 \\ &= a^2(x)\cos^2(2\pi\nu_c x) \\ &= \tfrac{1}{2}a^2(x) + \tfrac{1}{2}a^2(x)\cos(2\pi(2\nu)_c x), \end{aligned} \tag{A.15}$$

where a trigonometric identity has been used in the last line. It is seen from eq. (A.15) that the rectification demodulates the signal into two terms: one constituting the square of the modulating function only and one where the carrier is modulated by the same function. In addition, the frequency of the carrier is doubled. The Fourier transform of the squared modulation $a^2(x)$ is according to eq. (A.6) a convolution of the transformed modulation $A(\nu)$ with itself. That is,

$$\mathfrak{F}\{a^2(x)\} = A(\nu) * A(\nu). \tag{A.16}$$

The transform of the rectified signal $f_{rect}(x)$ has according to eq. (A.13) three terms proportional to $A(\nu) * A(\nu)$. Two are shifted, positively and negatively, by twice the carrier frequency $2\nu_c$. The third is not. Provided that the frequency spectrum $A(\nu)$ is sufficiently narrow, the two terms are completely separated in the frequency domain. Hence, $a^2(k)$ can be reconstructed from a Discrete Fourier Transform $F_{rect}(n)$ of the rectified signal by considering low frequent components only. In doing so, a low pass transfer function $G(n)$ is applied to the discrete transform, and $a^2(x)$ is given by an inverse discrete transform [WHY REAL PART????]

$$a^2(k) = \Re\left\{\sum_{n=0}^{N-1} G(n)F_{rect}(n)e^{-i2\pi nk/N}\right\}. \tag{A.17}$$

Finding the maximum of $a(x)$ is now equivalent to finding the maximum of $a^2(k)$. Calculating the derivative of (A.17) with respect to k and setting the result to zero yields

$$\frac{\mathrm{d}a^2(k)}{\mathrm{d}k} = \Re\left\{\sum_{n=0}^{N-1} G(n)F_{rect}(n)ime^{-i2\pi nk/N}\right\} = 0, \tag{A.18}$$

[3] ???

where constants have been dropped. By acknowledging that the global maximum is due to the low frequent character of the envelope, $a^2(k)$ can be strictly low pass filtered by setting $G(n)$ to zero for all n except that of the first non-trivial frequency component, i.e. $n = 1$. Eq. (A.18) is then rewritten as

$$\frac{\mathrm{d}a^2(k)}{\mathrm{d}k} = \Re\left\{F_{rect}(1)ie^{-i2\pi k/N}\right\} = 0. \tag{A.19}$$

An analytic expression for the position of the envelope peak can now be found. Solving for k yields

$$k = \frac{N}{2\pi} arg(F_{rect}(1)). \tag{A.20}$$

Appendix B

Hilbert transform method

This appendix is a revised version of a section written for my project work, presenting the Hilbert transform method of envelope detection. The derivations follow concepts from Poularikas [67] and Bracewell [65].

The Hilbert transform H of a signal $u(x)$ is defined by [67] as

$$H[u(x)] = v(x) = \frac{1}{\pi}\int_{-\infty}^{\infty}\frac{u(\eta)}{x-\eta},\mathrm{d}\eta \tag{B.1}$$

This transform is closely related to the Fourier transform through the convolution theorem. Since (B.1) is actually the convolution of the initial signal with the function $h(x) = \frac{1}{\pi x}$, the Fourier transform of the Hilbert transformed signal is

$$\mathcal{F}[v(x)] = F(\nu) = U(\nu)H(\nu) = U(\nu)\cdot(-i\cdot sgn(\nu)), \tag{B.2}$$

where $U(\nu)$ and $H(\nu)$ are the Fourier transforms of $u(x)$ and $h(x)$, respectively, and $sgn(\nu)$ is the sign-function that returns the sign of its argument (ν denotes a spatial frequency). Thus the Hilbert transform alters the phase of the Fourier components of the signal by $\frac{\pi}{2}$, positively or negatively according to the sign of the frequency. The amplitude of the components is unchanged. From this perspective, the Hilbert transform acts as a quadrature filter.

Two Hilbert transforms of particular interest in the detection of envelope are those of the sine and cosine functions. From the argument above, these transforms are given by

$$H[\sin(\nu x+\phi)] = \cos(\nu x+\phi) \tag{B.3}$$

$$H[\cos(\nu x+\phi)] = -\sin(\nu x+\phi). \tag{B.4}$$

An important property of the Hilbert transform is given by Bedrosian's product theorem. If a signal $u(x) = f(x)g(x)$ is a product of a low pass signal $f(x)$ and a high-pass signal $g(x)$ and the Fourier spectra of these signals do not overlap - then the Hilbert transform of this signal is

$$H[u(x)] = H[f(x)g(x)] = f(x)H[g(x)]. \tag{B.5}$$

In words, only the high pass filter is transformed.

Analytic signal

Constructing a complex function of which the real part is the signal and the imaginary part is its Hilbert transform, gives the *analytic signal*

$$\Psi(x) = u(x) + i \cdot v(x). \tag{B.6}$$

Assuming a signal is a product of an envelope $A(x)$ and a harmonic function,

$$u(x) = A(x)\cos(\nu x + \phi), \tag{B.7}$$

the envelope can be found explicitly from the magnitude of the analytic signal.

$$|\Psi(x)| = \sqrt{u^2(x) + v^2(x)} = \sqrt{A^2(x)[\cos^2(\nu x + \phi) + \sin^2(\nu x + \phi)]} = A(x). \tag{B.8}$$

In fact, the envelope *is* the magnitude of the analytic signal. The x corresponding to the peak of the envelope may be found directly from $A(x)$ by locating its maximum. If however the peak is not well-defined due to noise, the peak may be estimated by first fitting $A(x)$ to an assumed functional form, e.g. the general Gaussian function:

$$f(x) = ae-\frac{(x-b)^2}{2c^2} \tag{B.9}$$

This can be done by a polynomial least-squares fit, and the estimated peak position is resultantly the offset parameter b.

Appendix C

Analog to Digital Conversion

Analog to digital conversion (AD conversion) is a process that transforms a continuous signal to a discrete signal. A discrete signal necessarily contains less information than the equivalent analog signal, since a digital signal contains a finite number of data points whereas this number is infinite for an analog signal. The succeeding derivation on aliasing and the sampling theorem follows Lyons [68].

Aliasing

AD conversion involves sampling of an analog signal at uniform sampling intervals given by the sampling period t_s[1]. The corresponding sampling frequency is given by $f_s = \frac{1}{t_s}$. From Fourier analysis, an arbitrary analog signal can be represented as a sum of harmonic functions of the signals inherent frequencies. It is therefore sufficient to consider a sine wave of a single frequency in the following argument. If a signal $u(t) = sin(2\pi f_o t)$ is sampled at the sample frequency f_s, the obtained data points are given as

$$u(n) = sin(2\pi f_o n t_s), \quad n = 0, 1, 2, ... \tag{C.1}$$

where n is the sample number. Because of the periodicity of the sine function, (C.1) is equal to itself with the addition of an integer multiple m of 2π in the phase. Letting m be an integer multiple of the sample number, $m = kn$, (C.1) can be expanded to

$$u(n) = sin(2\pi f_o n t_s + kn2\pi) = sin(2\pi(f_o + \frac{k}{t_s})nt_s), \quad k = 0, \pm1, \pm2, ..., \tag{C.2}$$

which can be rewritten

[1]The formalism of spatial signals is entirely similar that of time-varying signals.

$$u(n) = sin(2\pi f_o n t_s) = sin(2\pi(f_o + k f_s) n t_s). \tag{C.3}$$

From (C.3), there is an ambiguity kf_s in the frequency of the digital signal when sampling at f_s. This ambiguity is unavoidable in AD conversion if the sampling frequency is not adequately large. Thus, attempting to reproduce the analog signal from the samples taken in the AD conversion process is not guaranteed complete accuracy. For any given signal and sample frequency, there exists a k such that a "least frequency" interpretation of the digital signal will have frequency in the range $[-\frac{f_s}{2}, \frac{f_s}{2}]$. This frequency is called the *alias* of the corresponding frequency of the analog signal. Any frequency outside of $[-\frac{f_s}{2}, \frac{f_s}{2}]$ is manifested by its alias frequency when the signal is reconstructed.

However, if the frequency to be converted is less than half the sampling frequency, i.e. if $|f_o| \leq \frac{f_s}{2}$ or equivalently $f_s \geq 2f_o$, only one harmonic interpretation of the sampled signal exists. The conversion is therefore unambiguous and the signal can be correctly reconstructed. If on the other hand $|f_o| \geq \frac{f_s}{2}$, aliasing will occur due to AD conversion. The frequency $f_s/2$ is known as the Nyquist frequency.

Considering the general case of a signal consisting of multiple frequencies, all of the frequencies must be in the range $[-\frac{f_s}{2}, \frac{f_s}{2}]$ for the signal to be reconstructed correctly after AD conversion [68]. This is the sampling theorem of AD conversion.

Appendix D

LabVIEW routines

This appendix presents a selection of LabVIEW routines that has been written for this work. The block diagrams of five visual instrument (vi) programs are shown, where the first four are used for recording interferograms and the last is used for controlling indenter movement. Table D.1 summarizes the various vi's functionality and hierarchical position. The routines used for recording phase maps are very similar to those used for interferograms, and are thus not shown.

Name	Functionality	Hierarchy
CaptureInterferogram.vi	Initiates and ends scanning.	Main vi.
PerformScan.vi	Records interferogram by scanning.	Sub-vi to CaptureInterferogram.vi.
Calibrate.vi	Calibrates voltage steps in scanning.	Sub-vi to PerformScan.vi.
VoltageRamp.vi	Outputs each voltage step on a linear ramp.	Sub-vi to both PerformScan.vi and ControlIndentAndScratch.vi.
ControlIndentAndScratch.vi	Controls the voltage supplied to the indent and scratch actuators.	Main vi.

Table D.1

CaptureInterferogram.vi (Block diagram)

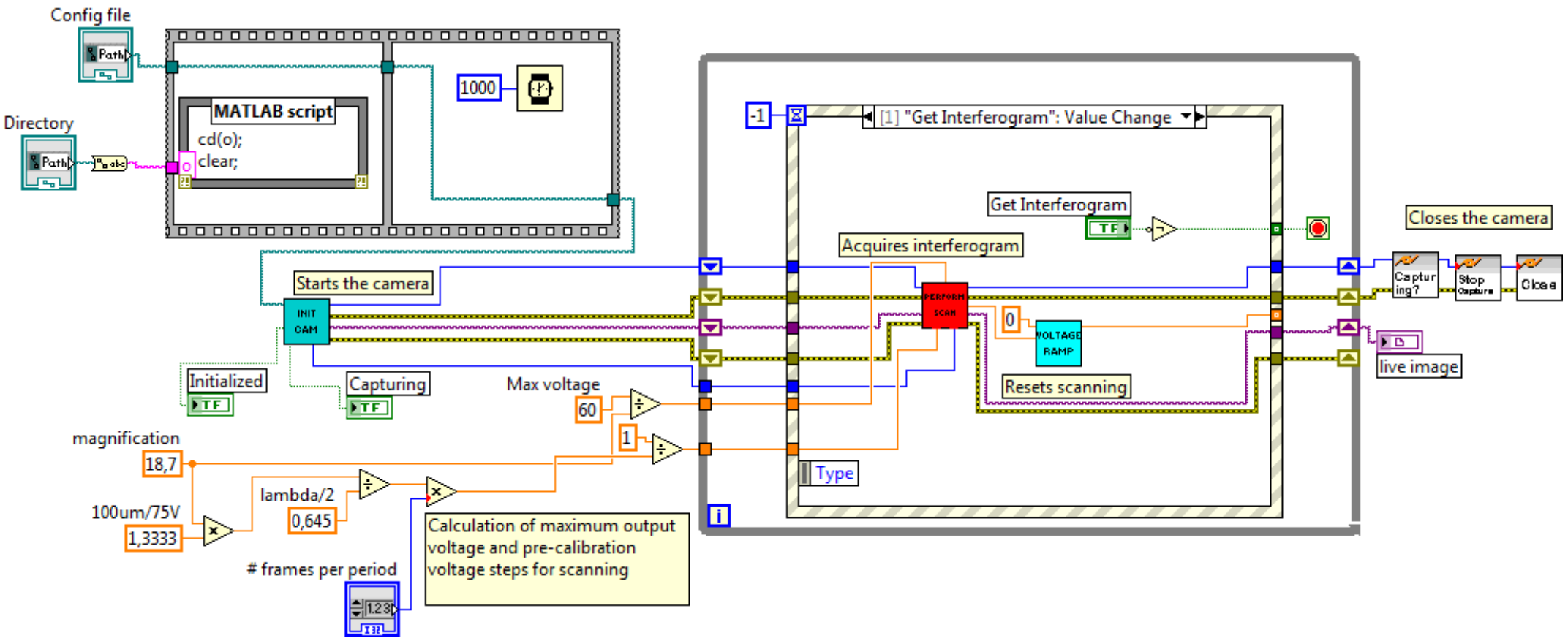

PerformScan.vi (Block diagram)

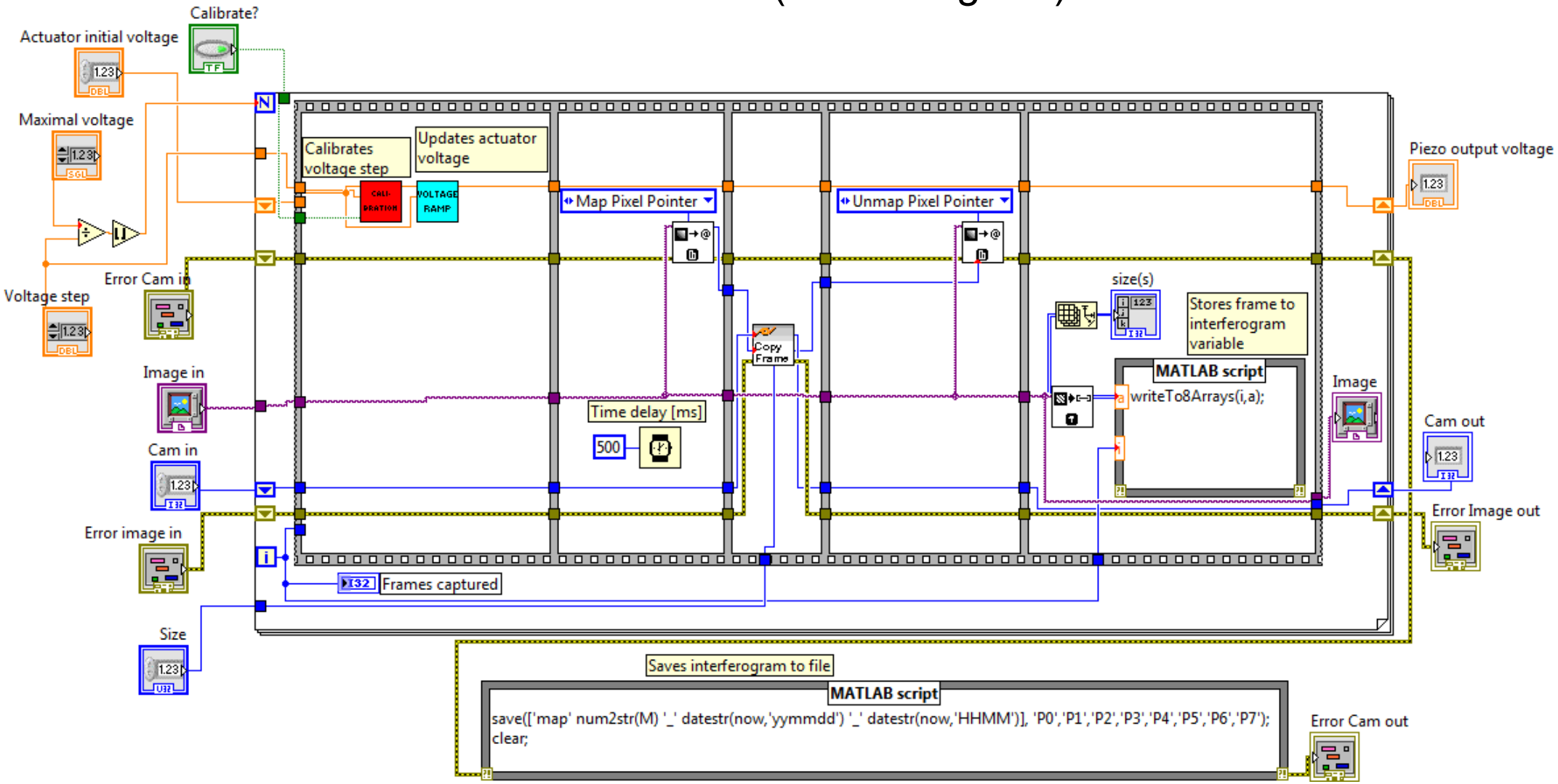

VoltageRamp.vi (Block diagram)

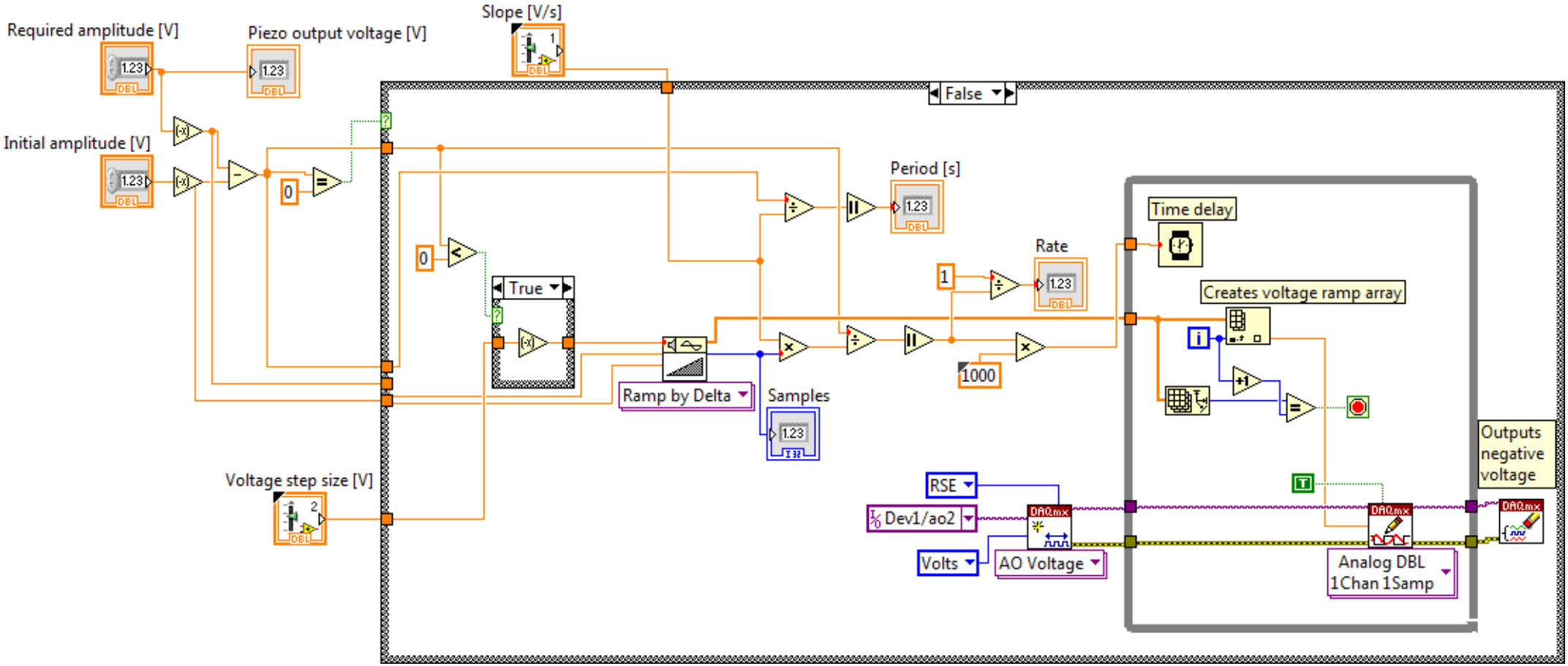

Calibrate.vi (Block diagram)

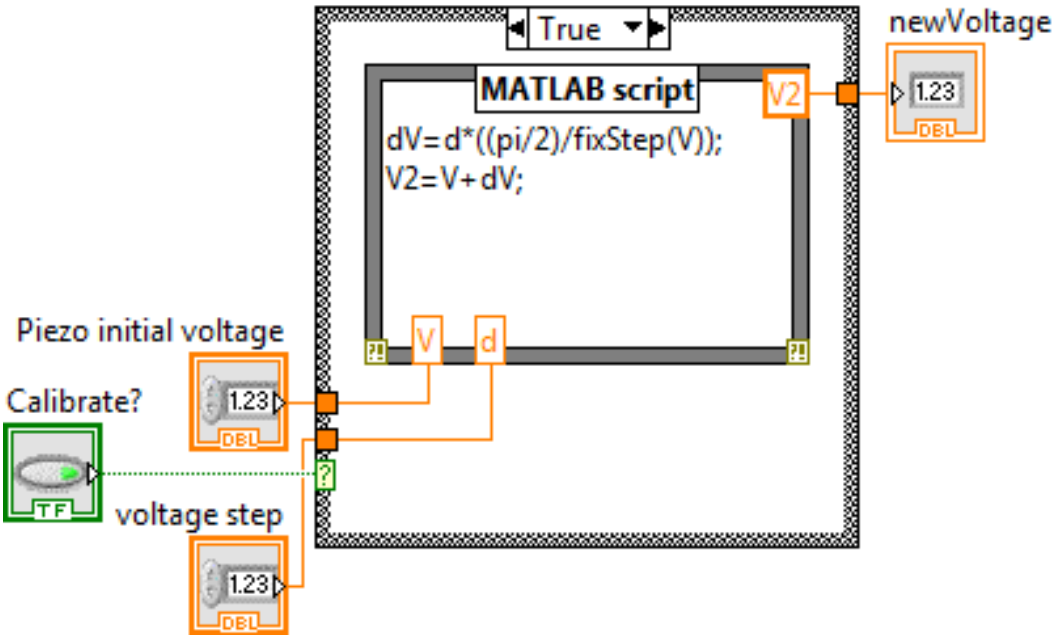

ControlIndentAndScratch.vi (Block diagram)

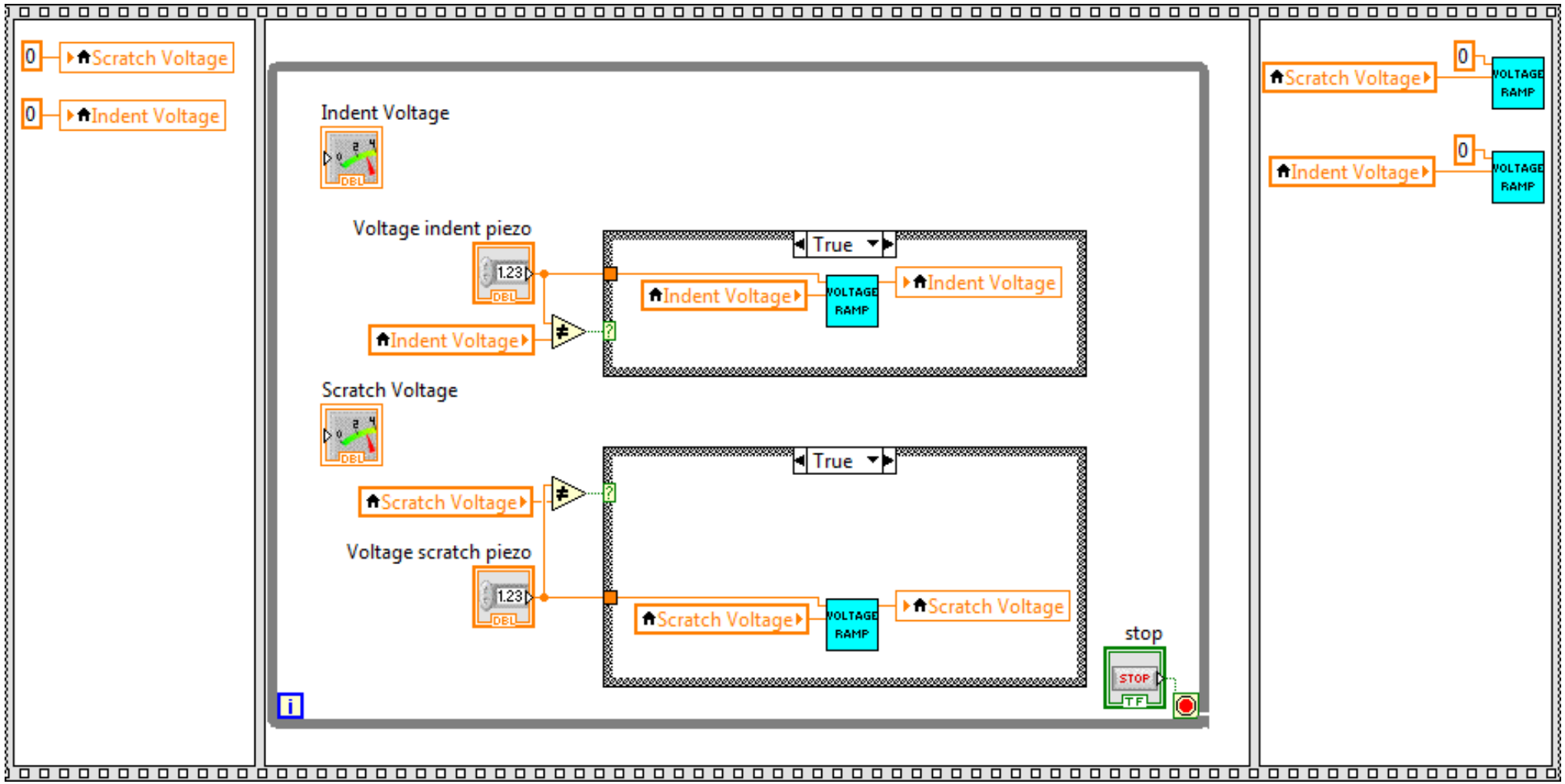

Appendix E

MATLAB code

This appendix presents the various MATLAB functions that have been written.

fixStep

```
function [y] =fixStep(x)
%Uses the calibration function (given by the coefficients a–d) to calibrate
%voltage steps given by the input voltage x.

a=0.8104;
b=0.8526;
c=-0.2233;
d=0.015;

y=d.*x.^3-c.*x.^2+b.*x+a;

end
```

writeTo8Arrays

```
function [] = writeTo8Arrays(i,a)
%Writes the input image array "a" to the correct subarray
%("P0"-"P7") according to the frame number "i".
%This function is used in the LabVIEW routine PerformScan.vi

    j=floor(i/8)+1;          % Calculates the correct sub-array index j.
    if mod(i,8)==0           % Finds the correct subarray and saves.
        P0(j,:,:)=a;
    elseif mod(i,8)==1
```

```
        P1(j,:,:)=a;
    elseif mod(i,8)==2
        P2(j,:,:)=a;
    elseif mod(i,8)==3
        P3(j,:,:)=a;
    elseif mod(i,8)==4
        P4(j,:,:)=a;
    elseif mod(i,8)==5
        P5(j,:,:)=a;
    elseif mod(i,8)==6
        P6(j,:,:)=a;
    else
        P7(j,:,:)=a;
    end
end
```

coherencePeakArray

```
function [DepthArrayDFT,DepthArrayHilbert] =coherencePeakArrayDFT(P0,P1,
                                                    P2,P3,P4,P5,P6,P7)
%Returns a 2D array with the index of coherence peak in each cell
    for i=1:512
        for j=1:640
        I=makePointInterferogram8(i,j,P0,P1,P2,P3,P4,P5,P6,P7);
        DFT=fft(I);
                %Computes the fast fourier transf.
        DFT(1)=0;
                %Deletes offset.
        IFT=real(ifft(DFT));
                %Inverse transformation
        DepthArrayDFT(i,j)=length(I)-findPeakCoherenceIndexDFT(IFT);
                %Computes peak position by the DFT method.
        DepthArrayHilbert(i,j)=findPeakCoherenceIndexHilbert(IFT);
                %Computes peak poisition by the Hilbert transform method.
        end
    end
end
```

makePointInterferogram8

```
function [P] = makePointInterferogram8(x,y,P0,P1,P2,P3,P4,P5,P6,P7)
%Reconstructs a 1D interferogram for the array location (x,y)
P=makeInterferogram8(P0(:,x,y),P1(:,x,y),P2(:,x,y),P3(:,x,y),P4(:,x,y),
```

```
                                                    P5(:,x,y),P6(:,x,y),P7(:,x,y));
end
```

makeInterferogram8

```
function [P] = makeInterferogram8(P0,P1,P2,P3,P4,P5,P6,P7)
% Reconstructs a 1D-interferogram from the 1D-subarrays "P0"-"P7"

for i=0:(length(P0)+length(P1)+length(P2)+length(P3)+length(P4)
        +length(P5)+length(P6)+length(P7)-1)
    j=floor(i/8)+1;
    if mod(i,8)==0
        P(i+1)=P0(j);
    elseif mod(i,8)==1
        P(i+1)=P1(j);
    elseif mod(i,8)==2
        P(i+1)=P2(j);
    elseif mod(i,8)==3
        P(i+1)=P3(j);
    elseif mod(i,8)==4
        P(i+1)=P4(j);
    elseif mod(i,8)==5
        P(i+1)=P5(j);
    elseif mod(i,8)==6
        P(i+1)=P6(j);
    else mod(i,8)==7
        P(i+1)=P7(j);
end
end
```

findPeakCoherenceIndexDFT

```
function [index] =findPeakCoherenceIndexFFT(I)
%Finds the index of the peak frame by the DFT method.

        N=length(I);
                %Determines the length of I
        FFT=fft(abs(I).^2);
                %Calculates the fft of the rectified signal |I|^2
        arg=angle(FFT(2));
                %Calculates the angular argument of FFT(2)
        if arg<0
                 arg=arg+2*pi;
```

```
            %Moves the angle to the range [0,2pi]
        end
        index=N*arg/(2*pi);
            %Calculates the index of the peak position
end
```

findPeakCoherenceIndexHilbert

```
function [index] = findPeakCoherenceIndexHilbert(I)
%Finds the index of the peak frame by the Hilbert transform method

    Envelope=abs(hilbert(I));
        %Calculates the envelope
    Envelope=moving(Envelope,50);
        %Applies a moving average filter
    index=findMaxPosFromGauss(Envelope);
        %Finds the peak position from a Gauss fit
end
```

findMaxPosFromGauss

```
function [b] = findMaxPosFromGauss(A)
%Returns the offset parameter b from a Gauss fit.

    [c,b,a]=mygaussfit(1:length(A),A);
end
```

mygaussfit

This code was written by Yohanan Sivan [69].

```
function [sigma,mu,A]=mygaussfit(x,y,h)

%
% [sigma,mu,A]=mygaussfit(x,y)
% [sigma,mu,A]=mygaussfit(x,y,h)
%
% this function is doing fit to the function
% y=A * exp( -(x-mu)^2 / (2*sigma^2) )
%
% the fitting is been done by a polyfit
% the lan of the data.
%
% h is the threshold which is the fraction
```

```
% from the maximum y height that the data
% is been taken from.
% h should be a number between 0-1.
% if h have not been taken it is set to be 0.2
% as default.
%


%% threshold
if nargin==2, h=0.2; end

%% cutting
ymax=max(y);
xnew=[];
ynew=[];
for n=1:length(x)
    if y(n)>ymax*h;
        xnew=[xnew,x(n)];
        ynew=[ynew,y(n)];
    end
end

%% fitting
ylog=log(ynew);
xlog=xnew;
p=polyfit(xlog,ylog,2);
A2=p(1);
A1=p(2);
A0=p(3);
sigma=sqrt(-1/(2*A2));
mu=A1*sigma^2;
A=exp(A0+mu^2/(2*sigma^2));
```

findPhaseMap

```
function [Phi] = findPhaseMap(P)
% Calculates a phase map from five frames stored in "P" using the
% five-frame algorithm.

for i=1:512
    for j=1:640
    Phi(i,j)=atan2(2*(P(2,i,j)-P(4,i,j)),2*P(3,i,j)-P(1,i,j)-P(5,i,j));
```

```
    end
end

end
```

Appendix F

Component Specifications

In this appendix, the specifications of a number of the experimental components of the system are listed.

Light source: Superlum BroadLighter S1300 [50]

Superlum BroadLighters | **S1300-G-I-20: 20 mW Benchtop Lightsource at 1300 nm**

High Output Power, Gaussian-like Optical Spectrum, Optically Isolated, Low-noise

Parameter	Device	Min	Typ.	Max
SM fiber output power – full power mode, mW	S1300-HP-I-G-B-20	15	20	-
SM fiber output power – low power mode, mW		1*	-	-
Mean wavelength, nm		1280	1290	1300
3 dB (FWHM) spectrum width, nm (full power)		45	-	-
Residual spectral modulation index (0.05 nm res), %		-	2.0	5.0
Output isolation		Built-in optical isolator (-30 dB)		
Fiber		SM, Corning SMF-28		
Output connector		FC/APC		
Long-term stability, %**		±0.5%		
Short-term stability, %***		±0.1%		

* other upon request. ** 8 hours, measurements taken every minute, 100 ms integration. *** 15 minutes, measurements taken every second, 100 ms integration. All measurements were taken after a one-hour warm-up period at ambient temperature 22±0.5 °C.

Optical Spectrum and Coherence Function

Full Power Mode

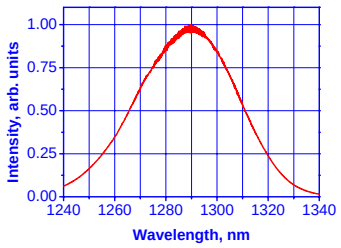

Low Power mode

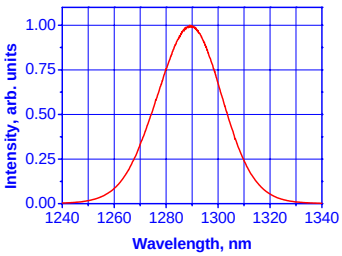

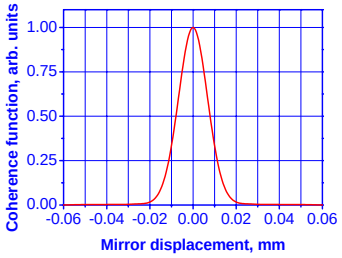

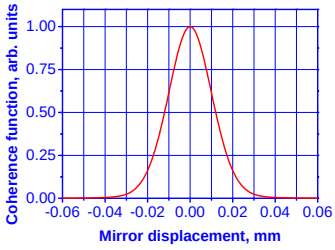

Typical RIN

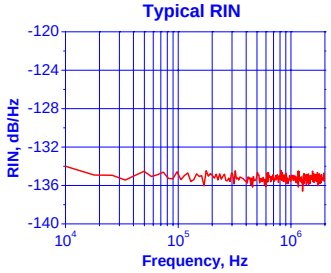

All specifications are subject to change without notice.
For more details check
http://www.superlumdiodes.com/s_broadlighters.htm.

Camera: Xenics Xeva-1.7-640 [70]

Specifications

Array specifications	Xeva-1.7-640
Array Type	InGaAs
Spectral band	Standard: 0.9 to 1.7 µm
# Pixels	640 x 512
Pixel Pitch	20 µm
Array Cooling	TE1-cooled down to 263K
Pixel operability	> 99%

Camera specifications	25 Hz	90 Hz
Lens (included)		
Focal length	25mm f/0.95	
Optical interface	C-Mount, spectrograph fixation holes (Broad selection of lenses are available)	
Imaging performance		
Frame rate	25 Hz	90 Hz
Integration type	Snapshot	
Exposure time range	1 µs up to 100 seconds	
Noise level: Low gain	7 AD counts	
High gain	14 AD counts	
S/N ratio: Low gain	67 dB	
High gain	61 dB	
A to D conversion resolution	14 bit	
Interfaces		
Camera control	USB 2.0	
Image acquisition	USB 2.0 / CameraLink	
Trigger	TTL levels	
Graphical User Interface (GUI)	Xeneth Advanced	
Power requirements		
Power consumption	< 4 Watt, cooler: 30 Watt max	
Input voltage	12 V	
Physical characteristics		
Camera cooling	Forced convection cooling	
Ambient operating temperature	0 to 50 °C	
Dimensions	90 W x 110 H x 110 L mm^3	
Weight camera head	App. 1.8 kg	
Weight power supply	300 g	

Microscope objective: M Plan Apo NIR 378-824-5 [71]

Near-infrared Radiation Corrected
M Plan Apo NIR for Bright Field Observation

Order No.	Mag.	N.A.	W.D.	f	R	D.F.	View field 1	View field 2	Mass
378-822-5	5X	0.14	37.5mm	40mm	2.0μm	14.0μm	ø4.8mm	0.96x1.28mm	220g
378-823-5	10X	0.26	30.5mm	20mm	1.1μm	4.1μm	ø2.4mm	0.48x0.64mm	250g
378-824-5	20X	0.40	20.0mm	10mm	0.7μm	1.7μm	ø1.2mm	0.24x0.32mm	300g
378-825-5	50X	0.42	17.0mm	4mm	0.7μm	1.6μm	ø0.48mm	0.10x0.13mm	315g
378-826-5	100X	0.50	12.0mm	2mm	0.6μm	1.1μm	ø0.24mm	0.05x0.06mm	335g
378-863-5	50X	0.65	10mm	4mm	0.42μm	0.65μm	ø0.48mm	0.10x0.13mm	450g
378-864-5	100X	0.70	10mm	2mm	0.39μm	0.56μm	ø0.24mm	0.05x0.06mm	450g

DIMENSIONS

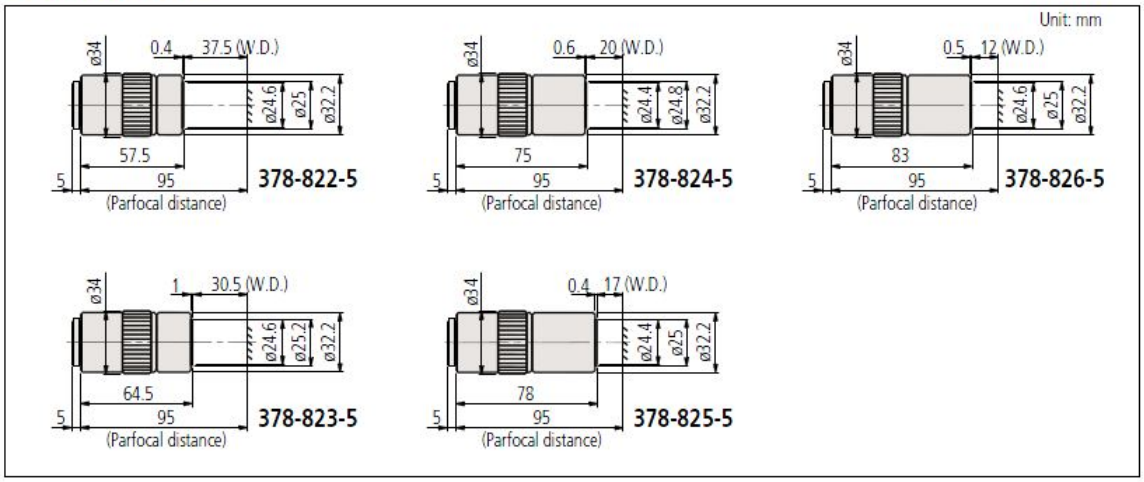

Scanning actuator: ThorLabs PAS015 [72]

Travel	100μm
Length	201mm
Resolution	100nm
Capacitance	18μF
Piezo Blocking Force	1000N @ 60V, 1150N @ 75V
Operating Temperature	-20 to 80°C

Indent actuators: ThorLabs DRV517 [72]

Micrometer Travel Range	12.7mm
Micrometer resolution	1μm
Piezo Travel Range	30μm
Piezo Resolution	10nm
Piezo Driving Voltage	75V
Piezo Capacitance	7.2μF

Rotation stage: ThorLabs PRM1Z8E [72]

Bidirectional Repeatability	$\pm 0.1^\circ$
Backlash	$\pm 0.3^\circ$
Max Rotation Velocity	25°/sec
Achievable Incremental Motion (Min)	25 arcsec
Repeatable Incremental Motion (Max)	0.03°
Absolute On-Axis Accuracy	0.01%
Max Percentage Accuracy	0.08%
Home Location Accuracy	$\pm 0.2^\circ$
Range	Continuous